Experimental study and modeling of metamaterials for water surface waves

Adam Anglart

To cite this version:

Adam Anglart. Experimental study and modeling of metamaterials for water surface waves. Mechanics [physics.med-ph]. Université Paris sciences et lettres, 2021. English. NNT : 2021UPSLS068 . tel-03516863

HAL Id: tel-03516863
https://pastel.hal.science/tel-03516863

Submitted on 7 Jan 2022

PSL
UNIVERSITÉ PARIS

THÈSE DE DOCTORAT
DE L'UNIVERSITÉ PSL

Préparée à l'**ESPCI PMMH**
Laboratoire de Physique et Mécanique des Milieux Hétérogènes

Experimental study and modeling of metamaterials for water surface waves

Étude expérimentale et modélisation de métamatériaux pour les ondes à la surface de l'eau

Soutenue par
Adam ANGLART
Le 14 décembre 2021

École doctorale n°391
Sciences mécanique, acoustique, électronique et robotique

Spécialité
Mécanique

Composition du jury :

Christophe JOSSERAND Directeur de recherche École Polytechnique	*Président du jury*
Sébastien GUENNEAU Directeur de recherche Imperial College London	*Rapporteur*
Pablo COBELLI Professeur des universités Universidad de Buenos Aires	*Rapporteur*
Stéphan FAUVE Professeur des universités École Normale Supérieure	*Examinateur*
Richard PORTER Professeur des universités University of Bristol	*Examinateur*
Vincent PAGNEUX Directeur de recherche Le Mans Université	*Directeur de thèse*
Agnès MAUREL Directrice de recherche Institut Langevin, ESPCI Paris	*Directrice de thèse*
Philippe PETITJEANS Directeur de recherche ESPCI Paris	*Directeur de thèse*

ESPCI PARIS | PSL

ESPCI PARIS | PSL

Adam Anglart

Experimental study and modeling of metamaterials for water surface waves

The presented research has been carried out
at the Laboratoire de Physique et Mécanique des Milieux Hétérogènes
(*CNRS PMMH, Sorbonne Université, 7 quai Saint-Bernard, 75005 Paris, France*)
of the École Supérieure de Physique et de Chimie Industrielles de la Ville de Paris
(*10 rue Vauquelin, 75005 Paris, France*)
on the premises of the Institut Langevin
(1 rue Jussieu, 75005 Paris, France)

Acknowledgements

When I came to Paris for the first time, I would have never thought that my adventure here would bring me so many new opportunities. The most important one so far was to prepare my PhD thesis with so many incredible people who supported me throughout this project.

First of all, I would like to express my deepest gratitude to my supervisors. Philippe Petitjeans, with his extensive knowledge in experimental research, guided me through the twists and turns of becoming a scientist. His outstanding organizational skills allowed me to focus on my studies and accelerated my progress, which would not have been possible if it had not been for the extraordinary pedagogical experience of Agnès Maurel in unraveling complex theoretical problems. In particular, I would like to express my genuine appreciation of her invaluable kindness. With equal recognition, I want to thank Vincent Pagneux, who continuously provided me with the newest theoretical advances in the field of wave physics. The sharpness and clarity of his mind were a source of inspiration not only on an academic but also on a personal ground.

My sincere gratitude also goes to the reviewers of my thesis, Sébastien Guenneau, and Pablo Cobelli, for a deep insight into this work. I would also thank Stéphan Fauve, Christophe Josserand, and Richard Porter for accepting to be a part of my thesis' jury.

Throughout these years, I was very lucky to have Samantha Kucher and Léo-Paul Euvé as my team members. Our day-to-day, both scientific and personal discussions, were always inspiring and stimulating. Many thanks also go to the interns Paweł Obrępalski and Natalia Pieśniewska for the unforgettable experience of discovering the perfect combination of coffee accompanied with *une tarte au citron.*

A friendly and sincere atmosphere at the office would not have been possible without Kamil Szafrański, Ludovic Bellebon, and Nathan Jeger-Madiot, who were always there to have a refreshing chat.

This challenging journey in the world of fluid dynamics started a few years ago with the inspiring lecture given by Sophie Goujon-Durand. Thanks to her, I was given an opportunity to join the PMMH laboratory as an intern, for which I will always be grateful.

Behind the scenes of the scientific work, there is a lot of administrational effort that makes the research possible. The masters of making the French bureaucracy accessible to a simple human being are Frédérique Auger and Claudette Barez, who were always there to offer their help.

For the arduous favor of proofreading this manuscript, I would like to express my gratitude to Harold Kasten, whose watchful eye was able to notice even the most inconspicuous typos and mistakes. I would also like to thank Bartłomiej Dobosz for the unique design of this thesis' cover.

I am enormously grateful to my closest friends Kasia Czajkowska, Tymoteusz Zdunek, Kasia Krzywik, and Thomas Palfray-Schneider, whose constant encouragement kept me motivated and confident in my abilities. Their strong belief in me allowed me to overcome many obstacles and moments of doubt. The time shared with Alexia Quintin and Giovanni Mezzano always kept me grounded and reminded me of what is important in life.

Last but not least, this thesis would never have been created if it had not been for the unconditional love and support of my parents Violetta and Marek, as well as my brothers Marcin and Maciej Anglart.

Titre : Étude expérimentale et modélisation de métamatériaux pour les ondes à la surface de l'eau

Résumé

La thèse concerne l'étude des métamatériaux dans le contexte des ondes à la surface de l'eau. Cette étude s'appuie sur une expérience en laboratoire qui permet de mesurer précisément le champ des ondes.

Dans la première partie, nous démontrons expérimentalement et numériquement que les métamatériaux peuvent être utilisés pour contrôler la propagation des ondes et les propriétés de résonance d'une cavité fermée, y compris le « cloaking » de ses modes propres. Le milieu anisotrope est conçu à partir de la théorie de la transformation des coordonnées et de l'homogénéisation d'un problème d'onde tridimensionnel. Ce milieu est constitué par un ensemble de plaques verticales dont l'espacement est très inférieur à la longueur d'onde. Cette structure impose une bathymétrie anisotrope qui influe sur la propagation des ondes différemment selon leur direction de propagation par rapport à ce milieu structuré. Trois cavités différentes, fabriquées par une imprimante 3D, sont testées et comparées au cas de référence avec bathymétrie sans structuration. La profilométrie par transformée de Fourier, ainsi que des capteurs de déplacement confocaux, sont utilisés pour les mesures de la déformation de la surface de l'eau résolues en temps et en espace. Les données expérimentales montrent une capacité remarquable du métamatériau à influer sur la propagation anisotrope des ondes à la surface de l'eau.

La deuxième partie concerne les métamatériaux immergés entre deux eaux pour lesquels un modèle homogénéisé est proposé et la solution numérique par méthode modale est fournie. Les propriétés anisotropes d'une telle structure sont étudiées expérimentalement en utilisant la même technique. Une analyse basée sur le formalisme de Bloch-Floquet est effectuée pour vérifier la relation de dispersion de ce milieu prédite par la méthode d'homogénéisation.

L'objectif principal de la troisième partie de cette thèse est d'étudier expérimentalement les états de bord topologiquement protégés dans un guide d'ondes à géométrie périodique en régime linéaire et non-linéaire. Une des représentations des états topologiques, fournie par le modèle Su-Schrieffer-Heeger (SSH), est appliquée pour décrire les phénomènes observés. Un guide d'ondes avec une largeur périodique est comparé au cas régulier d’un réservoir rectangulaire avec une largeur constante. Des capteurs de déplacement confocaux sont utilisés pour mesurer le champ d'onde très précisément. Les données expérimentales sont comparées aux résultats des simulations numériques 2D et à la prédiction du modèle SSH. Les résultats obtenus montrent que cette configuration très simple présente toutes les propriétés du modèle SSH avec un excellent accord.

Mots clés : métamatériaux, mécanique des fluides, ondes, homogénéisation, modèle SSH, étude expérimentale

Title: Experimental study and modeling of metamaterials for water surface waves

Abstract

This thesis concerns the study of metamaterials for water surface waves. The study is based on a laboratory experiment which makes it possible to measure the wave field precisely.

In the first part, we demonstrate experimentally and numerically that metamaterials can be used to control the wave propagation and resonance properties of a closed cavity, including the cloaking of its eigenmodes. The anisotropic medium is designed using coordinate transformation theory and the homogenization of a three-dimensional linear water wave problem. This medium consists of a set of vertical plates whose spacing is much lower than the wavelength. This structure imposes an anisotropic bathymetry which influences the propagation of the waves differently according to their direction of propagation. Three different cavities manufactured by a 3D printer are tested and compared to the reference case with bathymetry without structuring. Fourier transform profilometry, as well as confocal displacement sensors, are used for measurements of water surface deformation resolved in time and space. Experimental data shows a remarkable ability of the metamaterial to influence the anisotropic propagation of waves on the water surface.

The second part concerns the metamaterials submerged between two water layers for which a homogenized model is proposed, and the numerical solution by the modal method is provided. The anisotropic properties of such a structure are investigated experimentally using the same technique. An analysis based on the Bloch-Floquet formalism is performed to verify the dispersion relation of this medium predicted by the homogenization method.

The main objective of the third part of this thesis is to experimentally study topologically protected edge states in a waveguide with periodic geometry in both linear and nonlinear regimes. One of the representations of topological states, provided by the Su-Schrieffer-Heeger (SSH) model, is applied to describe the observed phenomena. A waveguide with periodic width is compared to the regular case of a rectangular reservoir with constant width. Confocal displacement sensors are used to measure the wave field very precisely. The experimental data is compared with the results of the 2D numerical simulations and the prediction of the SSH model. The results obtained show that this very simple configuration presents all the properties of the SSH model with excellent agreement.

Keywords: metamaterials, fluid mechanics, waves, homogenization, SSH model, experimental study

Table of contents

Introduction

> *"If you want to find the secrets of the Universe, think in terms of energy, frequency and vibration."*
>
> Nikola Tesla

Everything appears to be in a constant state of motion, whether it is a particle, a wave, or both at the same time. The idea of a **wave** *per se* is a universal, and thus quintessential concept for every field of physics – starting from the scale of subatomic particles that exhibit wave-like properties, through the propagation of light, sound, water (Fig. 1a), or earthquakes to scales as big as that of the gravitational waves that travel through spacetime. The advances in the field of wave physics from the last century contribute to the constant development of humankind, whether it comes to communication over a great distance, harvesting renewable energies, or inspecting environments previously beyond the reach of a naked eye with examples as diverse as visualizing our internal organs using ultrasound or capturing the image of the black hole (Fig. 1b) by an international network of radio telescopes [2]. These analogies

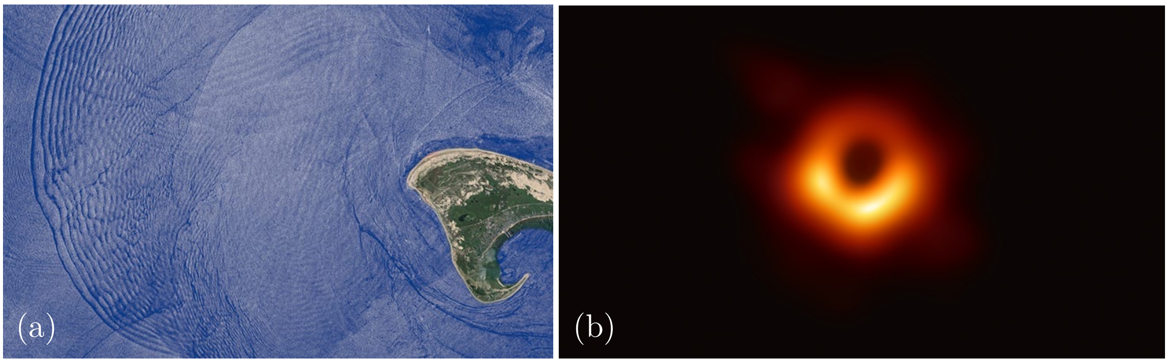

Fig. 1 (a) Satellite imagery of water waves formed at the ocean surface by an internal wave propagating deeper in the depths [1]. (b) An image of the black hole at the center of galaxy M87 [2].

allow to observe the same phenomena throughout different types of waves, but how far can we push them, and what is the degree of universality between them?

A wave is a disturbance that propagates from the spot where it was created (*source*) and carries energy at a certain distance but does not necessarily transfer any mass. Sound and water waves are mechanical waves. They necessitate a medium to travel through – a gas, a solid, or a liquid. The speed with which it travels depends on the material characteristics of the medium. By changing the properties of the medium, one can control the propagation of the wave. Since water waves are common and readily visible due to their macroscopic scale, they are often studied to understand the properties and phenomena of their other counterparts. On the other hand, many challenges arise due to the inherent water waves complexities, such as nonlinear effects revealed for large enough surface elevation gradient or its dispersive behavior varying with depth. In this thesis, we focus on an experimental study of water surface waves.

A medium, through which the wave propagates, with specially designed unique patterns or structures, is called a **metamaterial** – from the Greek *μετά*-, meaning *beyond*, *higher* or *changed*, *altered*. These specially engineered material properties cause the wave to interact with the metamaterial in ways not commonly found in nature. However, some links can be found, through which fascinating phenomena emerge when it comes to the naturally periodic media. One of the examples illustrates the occurrence of flow control through an array of unique structures on a shark's skin [3]. It consists of millions of microscopic scales (Fig. 2a). Where control of the water flow adjacent to the predator's body is essential, i.e., around the gills and at the trailing edge of the dorsal fin, the scales can move. The size of the scales corresponds to the size of the

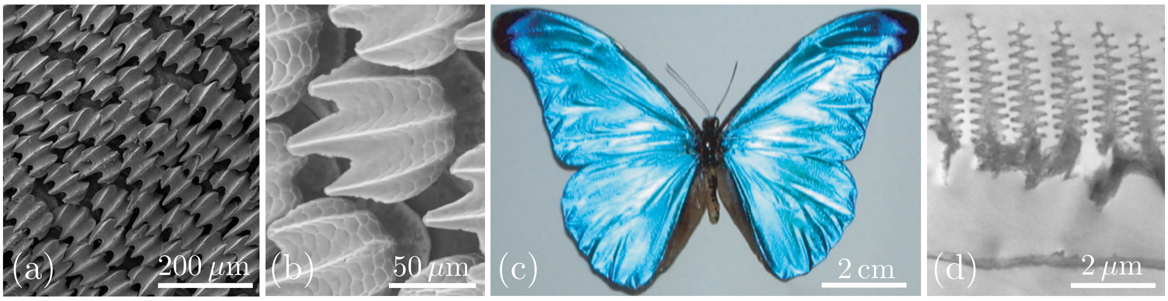

Fig. 2 (a) Close-view image of denticles from the surface of the mid-body region in a bonnethead shark *Sphyrna tiburo* [3]. (b) Details of typical denticle structure with the three surface ridges and three posteriorly pointing prongs. Such denticle structure appears on the body, fins, and tail [3]. (c) Whole specimen of *Morpho rhetenor* butterfly [4]. (d) Transmission electron microscope image showing cross-section of a scale of *Morpho rhetenor* [5].

boundary layer. It has been shown that the scales indeed do delay the flow separation, and the usefulness of similar structures is being investigated in aviation [6].

Another example could involve the phenomenon of iridescence which consists in the fact that certain surfaces progressively change their color as the angle of the incident light wave changes. This extraordinary quality is attributable to the microstructure that interferes with light and can be found, i.e., in bird feathers, certain minerals, or butterfly wings (Fig. 2d). It is therefore evident that by modifying the medium at the wavelength scale, new material properties are found that allow intricate control of the wave propagation.

The concept of designing metamaterials exhibiting peculiar behavior has always been attracting the attention of the scientific and engineering community. Metamaterials, originally used in electromagnetism [7, 8] gained their worldwide interest especially when it was shown that they can be used to make objects **invisible** [9, 10]. The principle of cloaking using the metamaterial, being one of the most fascinating applications, is based on the fact that the Helmholtz and Maxwell equations preserve their form when undergoing coordinate transform. It has been shown that not only the perfect transmission of the wave through the scatterer can be achieved, but also the scattered field around the object can be canceled, thus making the object fully undetectable.

During the last two decades, attempts to translate these peculiar properties have been made for other fields of physics [11, 12]. A substantial interest has been developed in controlling acoustic [13–17], elastic [18–21], and seismic waves [22–26] using metamaterials. They have been also employed to control water wave propagation, for which some of the applications include cloaking [27–30], focusing [31], or guiding the energy flow [32, 33]. As a result, metamaterials for water waves can be beneficial for coastal engineering when it comes to wave-free zones, shore protection, energy harvesting, or designing wakeless watercrafts.

Water wave metamaterials usually consist of the periodic structure at a subwavelength scale allowing to obtain new global properties. It can be summarized that to obtain the aforementioned special properties, one can use submerged or surface piercing pillars, holes in the seabed, or varying depth. Designing such structures would not have been possible if it had not been for special mathematical tools that allow to reduce complicated hydrodynamical problems into ones that are easier to approach and solve. Here, the **homogenization technique** [34–37] is of a significant importance and helps, under certain assumptions to replace the original heterogeneous microstructure with a comparable continuum. An array of heterogeneous thin plates are commonly employed to manufacture water wave metamaterials [38, 39]. To avoid complicated analysis involving an explicit representation of all heterogeneities due to the array of plates, the model of heterogeneous thin structures can be reduced using homogenization techniques.

Traditionally, as mentioned before, metamaterials are studied as a subwavelength structure. This assumption, essential for the homogenization technique, is necessary to obtain the effective model of the heterogeneous problem. Nonetheless, the exotic behavior of the wave can be acquired when the size of the structure is comparable to the wavelength [40, 41]. One of the approaches corresponds to the theory of topological insulators [42, 43] and is studied in this thesis.

The main objective of this thesis is to investigate both experimentally and theoretically the possible advances in the design of metamaterials for water surface waves.

Organization of the manuscript

The main body of this thesis consists of six chapters and is organized as follows.

Chapter 1 describes the theoretical foundation essential for the study of water surface wave systems. First, the mathematical description of linear water wave theory is specified, and the water wave dispersion relation is derived. Then, the notion of the propagating and evanescent mode is introduced in the case of a wave in a waveguide. Later on, we show the usefulness of the cavity eigenmodes when it comes to determining the solution of the Helmholtz equation, and a definition of cavity resonance is given. Finally, the last section of this chapter provides the comprehensive derivation of the effective model for the one-dimensional wave equation and the two-dimensional shallow water equation by means of the asymptotic homogenization technique for a stratified medium.

Chapter 2 briefly overviews two experimental techniques used throughout the presented research in order to measure the wavefield accurately. The Fourier transform profilometry method that allows for high-resolution space-time resolved measurement of the water surface elevation is presented. Moreover, we demonstrate the principle of confocal chromatic measuring, on which confocal displacement sensors used in our experiment are based.

Chapter 3 concentrates on the experimental study of the metamaterial for water waves, which consists of the stratified structure at a subwavelength scale, and is placed at the bottom of the cavity (*metabathymetry*). The metamaterial cavities of irregular shape are designed and manufactured using the 3D printing technique. Owing to the geometric transformation theory and the homogenization method, we are able to cloak the deformation of the cavities and make this deformation invisible for water waves.

Chapter 4 presents the homogenized model for the submerged plates array serving as a metamaterial for water surface waves. This approach, different from the one given in Chapter 3, allows to abandon shallow water approximation and gain considerable advantages in metamaterial design. The robustness of such a medium is studied experimentally, and its anisotropic capacities are investigated. Bloch-Floquet analysis is performed to compare the band structure of the submerged metamaterial to the dispersion relation obtained through the homogenization technique.

Chapter 5 focuses on the experimental investigation of the periodic structure comparable to the size of the wavelength and developed owing to the theory of topological insulators. The direct mapping between the one-dimensional Su-Schrieffer-Heeger model and the periodic water waveguide is shown. The presence of localized zero-energy edge modes is confirmed and studied both in the linear and nonlinear regimes.

Chapter 6 summarizes the obtained results. Main conclusions from the presented work are formed, and possibilities of further research opened by this study are offered.

Chapter 1

Theoretical background

1.1 Linear wave theory

In general, the motion of the fluid related to wave propagation can be described by the Navier-Stokes equation

$$\rho\left(\frac{\partial \mathbf{u}}{\partial t}+\mathbf{u}\cdot\nabla\mathbf{u}\right)=\rho\mathbf{g}-\nabla p+\mu\,\triangle\mathbf{u}, \tag{1.1}$$

where ρ stands for the density of the fluid, $\mathbf{u}=[u(\mathbf{x},t)\ v(\mathbf{x},t)\ w(\mathbf{x},t)]$ is a three-dimensional velocity field ($\mathbf{x}=[x\ y\ z]$), ∇p denotes the pressure gradient, and μ identifies dynamic viscosity. The vector of external forces $\mathbf{g}$ usually contains the gravitational acceleration and is of the form $\mathbf{g}=[0\ 0\ -g]$ (Fig. 1.1). This nonlinear equation (1.1) mathematically represents the general case of the viscous, compressible fluid flow that is nonstationary and undergoes external forces. The nabla ∇ and Laplace operator $\triangle$ are defined as

$$\nabla=\begin{bmatrix}\dfrac{\partial}{\partial x} & \dfrac{\partial}{\partial y} & \dfrac{\partial}{\partial z}\end{bmatrix} \quad \text{and} \quad \triangle\equiv\nabla\cdot\nabla=\frac{\partial^2}{\partial x^2}+\frac{\partial^2}{\partial y^2}+\frac{\partial^2}{\partial z^2}. \tag{1.2}$$

However, many assumptions can be used to considerably simplify the Navier-Stokes equation when it comes to the scale of the experimental laboratory setting. The linear wave theory, widely known as the Airy wave theory, is usually used to describe surface waves [44]. Many approaches scrupulously derive the linearized theory of water waves [45–47]. Below, we give the main points and relations that are used extensively throughout this thesis.

We choose z as the vertical axis, where $z = 0$ represents the undisturbed free surface (Fig. 1.1) that is bounded by the impervious bed with a constant depth $z = -h$. The surface elevation is denoted as $\zeta(x, y, t)$, where x and y stand for the horizontal coordinates. We assume that the fluid lying above $z = 0$ (i.e., air) has a density much lower than water ρ. Thus the influence of this fluid on the motion of the water can be neglected.

We consider the fluid to be inviscid ($\mu = 0$) and irrotational, meaning that there is no vorticity in the fluid, and the fluid velocity satisfies

$$\nabla \times \mathbf{u} = 0. \tag{1.3}$$

This assumption allows to introduce the scalar velocity potential ϕ

$$\mathbf{u} = \nabla\phi. \tag{1.4}$$

The compressibility of water can be neglected, thus the continuity equation takes forms

$$\nabla \cdot \mathbf{u} = 0. \tag{1.5}$$

Plugging (1.4) into (1.5), we conclude that the velocity potential ϕ satisfies the Laplace equation

$$\triangle\phi = 0 \quad \text{in } \Omega, \tag{1.6}$$

where Ω denotes the domain occupied by the fluid. The Euler equations, which represent the momentum conservation of a nonviscous fluid, allow the pressure in the fluid to be determined. Setting the pressure to be constant on a free surface and

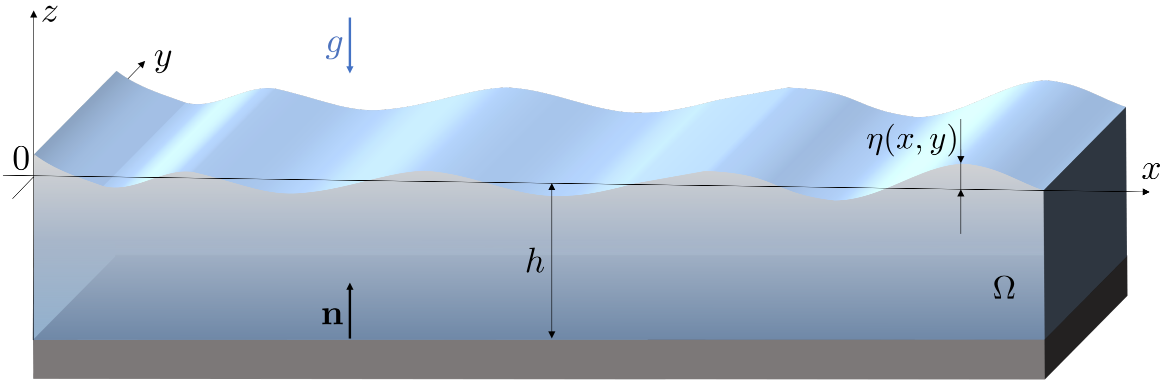

Fig. 1.1 Scheme of the water wave system.

linearizing around the mean level $z = 0$ as well as assuming a small gradient of surface elevation, we obtain the dynamic free surface boundary condition

$$\frac{\partial \phi}{\partial t} = -g\zeta \quad \text{at} \quad z = 0. \tag{1.7}$$

In a similar fashion, a linearized version of the kinematic free-surface condition of the surface is obtained. It links the vertical component of the velocity field with the vertical displacement on the mean water surface as follows

$$\frac{\partial \phi}{\partial z} = \frac{\partial \zeta}{\partial t} \quad \text{at} \quad z = 0. \tag{1.8}$$

These two above conditions (1.7) and (1.8) can be merged into

$$\frac{\partial^2 \phi}{\partial t^2} = -g\frac{\partial \phi}{\partial z} \quad \text{at} \quad z = 0, \tag{1.9}$$

and thus eliminate ζ. Another condition implies no flow through the impervious bottom

$$\mathbf{n} \cdot \nabla \phi = 0 \quad \text{at} \quad z = -h, \tag{1.10}$$

which in our case reduces to

$$\frac{\partial \phi}{\partial z} = 0 \quad \text{at} \quad z = -h. \tag{1.11}$$

The above approach is often transformed into the frequency domain. The advantage of getting rid of the time dependence is that we are also getting rid of the additional initial conditions that would have to be imposed. We benefit from the fact that the governing equations and boundary conditions for ϕ are linear, so if needed, any time domain solution can be obtained by inverse Fourier transform of the problem's solution in the frequency domain. Hence, we write

$$\phi(\mathbf{x}, t) = \mathrm{Re}\left[\varphi(\mathbf{x})\mathrm{e}^{-\mathrm{i}\omega \mathrm{t}}\right], \tag{1.12}$$

$$\zeta(x, y, t) = \mathrm{Re}\left[\eta(x, y)\mathrm{e}^{-\mathrm{i}\omega \mathrm{t}}\right], \tag{1.13}$$

where φ and η are now complex functions that depends on the frequency ω. The problem, following (1.6), and (1.9), now reduces to

$$\triangle\varphi = 0 \quad \text{in } \Omega, \tag{1.14}$$

$$\frac{\partial\phi}{\partial z} = \frac{\omega^2}{g}\varphi \quad \text{at} \quad z = 0, \tag{1.15}$$

$$\frac{\partial\phi}{\partial z} = 0 \quad \text{at} \quad z = -h. \tag{1.16}$$

Also, the vertical displacement can be expressed by the velocity potential (1.7)

$$\eta(x, y) = \frac{\mathrm{i}\omega}{g}\varphi(x, y, 0). \tag{1.17}$$

Ultimately, it can be shown that the velocity potential that satisfies the above conditions is exponentially decaying in the direction of increasing depth. For the propagating wave with an amplitude A, and whose wavenumber $\mathbf{k} = [k_x \ k_y]$, the potential is of the form

$$\varphi = \frac{\mathrm{i}gA}{\omega}\frac{\cosh k(z+h)}{\cosh kh}\mathrm{e}^{\mathrm{i}(k_x x + k_y y)}, \tag{1.18}$$

where $k = |\mathbf{k}|$, and the relation between the frequency ω and the wavenumber k coming from (1.15) is

$$\omega^2 = gk \tanh kh. \tag{1.19}$$

1.2 Dispersion relation for water waves

The relation (1.19) obtained in the previous section is called the dispersion relation for water waves

$$\boxed{\omega^2 = gk \tanh(kh).} \tag{1.20}$$

The phase velocity of the wave is defined as $c_p = \omega/k$, whereas group velocity $c_g = \partial\omega/\partial k$. Thus, using the dispersion relation, we have

$$c_p = \frac{\sqrt{gk \tanh kh}}{k} \quad \text{and} \quad c_g = \frac{\sqrt{gk \tanh kh}}{2k}\left(1 + \frac{2kh}{\sinh 2kh}\right). \tag{1.21}$$

However, for shallow water waves ($kh \ll 1$) the dispersion relation can be simplified to

$$\omega = \sqrt{gh}k. \tag{1.22}$$

When it comes to shallow water waves described by the dispersion relation (1.22), the angular frequency ω is directly proportional to the wavenumber k. It yields that the group velocity and phase velocity are equal, thus the wave is nondispersive ($\partial c_p/\partial\omega = 0$). For the deep water regime $kh \gg 1$, we have

$$\omega = \sqrt{gk}, \tag{1.23}$$

with the phase velocity $c_p = g/\omega$, and $c_g = c_p/2$ which shows the dispersive character of the wave ($c_p \neq c_g$).

1.3 Waves in a channel

Assuming harmonic regime with the time dependence chosen as $\mathrm{e}^{-\mathrm{i}\omega t}$ and constant water depth, the surface elevation η satisfies the homogenous Helmholtz equation

$$\triangle\eta + k^2\eta = 0, \tag{1.24}$$

with the boundary conditions on both walls of the channel (Fig. 1.2)

$$\left.\frac{\partial\eta}{\partial y}\right|_{y=0} = \left.\frac{\partial\eta}{\partial y}\right|_{y=w} = 0. \tag{1.25}$$

The wavenumber k is given through dispersion relation (1.19). The wavefield can be decomposed as follows

$$\eta(x,y) = \sum_n f_n(x)g_n(y), \tag{1.26}$$

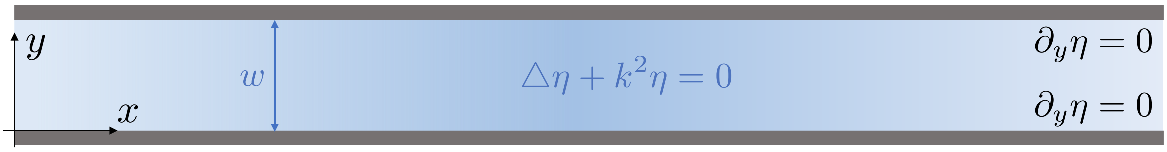

Fig. 1.2 Scheme of the waveguide of the width w with impermeable boundary conditions at the wall.

assuming g_n forms an orthonormal basis. Owing to the separation of variables, g_n has to satisfy

$$g_n'' + k^2 g_n = 0, \tag{1.27}$$

$$g_n'(0) = g_n'(w) = 0, \tag{1.28}$$

where $g' = \mathrm{d}g/\,\mathrm{d}y$, which yields an infinite set of modes of the form

$$g_n = A_n \cos \alpha_n y, \quad \text{where} \quad \alpha_n = \frac{n\pi}{w},\ n = 0, 1, 2, \ldots \tag{1.29}$$

Projecting the Helmholtz equation (1.24) on the basis $\int_0^w g_m g_n \,\mathrm{d}y = \delta_{mn}$ we have

$$\int_0^w g_m \sum_n \left[\ddot{f}_n g_n + (k^2 - \alpha_n^2) f_n g_n \right] \mathrm{d}y = 0, \tag{1.30}$$

where $\dot{f} = \mathrm{d}f/\,\mathrm{d}x$, and which gives

$$\ddot{f}_n + (k^2 - \alpha^2) f_n = 0. \tag{1.31}$$

The solution of the above equation can be expressed as

$$f_n = a_n \mathrm{e}^{\mathrm{i}k_n x} + b_n \mathrm{e}^{-\mathrm{i}k_n x}, \quad \text{where} \quad k_n^2 = k^2 - \alpha_n^2, \tag{1.32}$$

and where a_n, b_n stand for the complex amplitudes of the right and left going waves respectively. Ultimately, the sought wavefield is given by

$$\eta(x, y) = \sum_n A_n \left(a_n \mathrm{e}^{\mathrm{i}k_n x} + b_n \mathrm{e}^{-\mathrm{i}k_n x} \right) \cos \alpha_n y. \tag{1.33}$$

This approach lets us recognize two different kind of modes. For $k^2 - (n\pi/w)^2 > 0$ we have a **propagating** mode with

$$k_n = \sqrt{k^2 - \left(\frac{n\pi}{w} \right)^2}. \tag{1.34}$$

On the other hand for $(n\pi/w)^2 - k^2 > 0$, the wavenumber k_n becomes imaginary, thus the wavefield is exponentially decaying and the mode is **evanescent** with

$$k_n = \mathrm{i}\sqrt{\left(\frac{n\pi}{w} \right)^2 - k^2}. \tag{1.35}$$

The above analysis allows, in some cases, to proceed with the introduction of a one-dimensional model. The usefulness of this approach will be shown later in this work to perform the reduction of the model from two-dimensional to one-dimensional.

1.4 Cavity: resonance and modes

Similarly, as in Section 1.3, we assume harmonic regime with the time dependence $\mathrm{e}^{-\mathrm{i}\omega t}$ and constant water depth. The surface elevation η satisfies the Helmholtz equation

$$\triangle\eta + k^2\eta = 0, \tag{1.36}$$

where the wavenumber k is given through dispersion relation (1.19). The Helmholtz equation (1.36) has to be supplied with boundary conditions. In general for water waves, boundary conditions are of Neumann type ($\partial_{\mathbf{n}}\eta = 0$) and are applied in order to simulate a vertical hard wall or the impermeable seabed. Nonetheless, one can also apply Dirichlet ($\eta = 0$) or mixed boundary conditions depending on the physical problem.

The usual modes are solutions of the homogeneous Helmholtz equation (1.36). In the case of a closed cavity, the wave is unable to escape the cavity and the boundary conditions select a set of discrete frequencies k_n and eigenmodes η_n that satisfy

$$\triangle\eta_n + k_n^2\eta_n = 0, \tag{1.37}$$

with $\partial_{\mathbf{n}}\eta_n = 0$ at the boundary, where $\mathbf{n}$ is the normal to the boundary and n is the number of the mode. The set of modes η_n provides an orthonormal basis with the property

$$(\eta_m|\eta_n) = \delta_{nm}, \tag{1.38}$$

where the scalar product is defined as $(f|g) = \int \overline{f(\mathbf{x})}g(\mathbf{x})\mathrm{d}\mathbf{x}$. The benefits of the modes can now be shown when one wants to solve the Helmholtz equation in the same cavity with a source $s(\mathbf{x})$

$$\triangle\eta + k^2\eta = s(\mathbf{x}). \tag{1.39}$$

The wavefield η can be expanded on the mode basis as

$$\eta(\mathbf{x}) = \sum_n c_n \eta_n(\mathbf{x}). \tag{1.40}$$

Substituting this expansion to the wave equation and using the orthonormality (1.38), the coefficients c_n can be expressed as follows

$$c_n = \frac{(s|\eta_n)}{k^2 - k_n^2}. \tag{1.41}$$

Assuming that the projection of the source term $(s|\eta_n)$ is not zero, when $k \approx k_n$, the solution is given mainly by the mode η_n. It can be seen that the inherent character of the modes allows to find a set of functions that are independent of the source, and they predict the form of the wave when the imposed frequency is close to a resonance frequency.

1.5 Homogenization technique

Homogenization techniques serve as the foundation for replacing the actual heterogeneous microstructure with an analogous continuum, which helps to study the mechanical properties of metamaterials. Heterogeneous thin plates are commonly employed in state-of-the-art applications requiring unusual mechanical and thermal properties. Such structures include, e.g., a wide range of composite thin sheets and panels, which are widely used in the aerospace and automotive industries, where the need for increased lightness and strength is always desired. In our situation, they are used to provide a medium for controlling the propagation of water waves. To avoid the costly calculations involving an explicit representation of all heterogeneities, modeling heterogeneous thin structures necessitates homogenized models.

1.5.1 Homogenization of 1D wave equation

We begin with a generalized case of a 1D wave equation that shows the concept of the homogenization method. We assume a medium with periodically varying material parameters $a(\mathrm{x})$ and $b(\mathrm{x})$ with a period h (Fig. 1.3a), and introduce the one-dimensional wave equation as

$$\begin{cases} (a(\mathrm{x})\eta'(\mathrm{x}))' + k^2 b(\mathrm{x})\eta(\mathrm{x}) = 0 \\ \eta(\mathrm{x}),\ a(\mathrm{x})\eta'(\mathrm{x}) \in C^0, \end{cases} \tag{1.42}$$

where k is the wavenumber and $f' = \mathrm{d}f/\mathrm{dx}$. It is worth noticing that for constant values of parameters $a(\mathrm{x}) = a_1$ and $b(\mathrm{x}) = b_1$ the equation (1.42) takes a trivial form

$$\eta''(\mathrm{x}) + \tilde{k}^2\eta(\mathrm{x}) = 0, \tag{1.43}$$

where the new wavenumber is defined as $\tilde{k} = k\sqrt{b_1/a_1}$.

However, with a periodically varying medium, we can use the homogenization technique to simplify the problem. The periodic material parameters a and b cause the solution to have superimposed small perturbations that are negligible (Fig. 1.3b) yet make the equation more cumbersome to solve. Thus, we derive the equation satisfied by large scale variation (λ) with effective, constant parameters. We consider low frequency regime where

$$\lambda = \frac{2\pi}{k} \gg h, \tag{1.44}$$

and we define the small parameter

$$\epsilon = kh \ll 1. \tag{1.45}$$

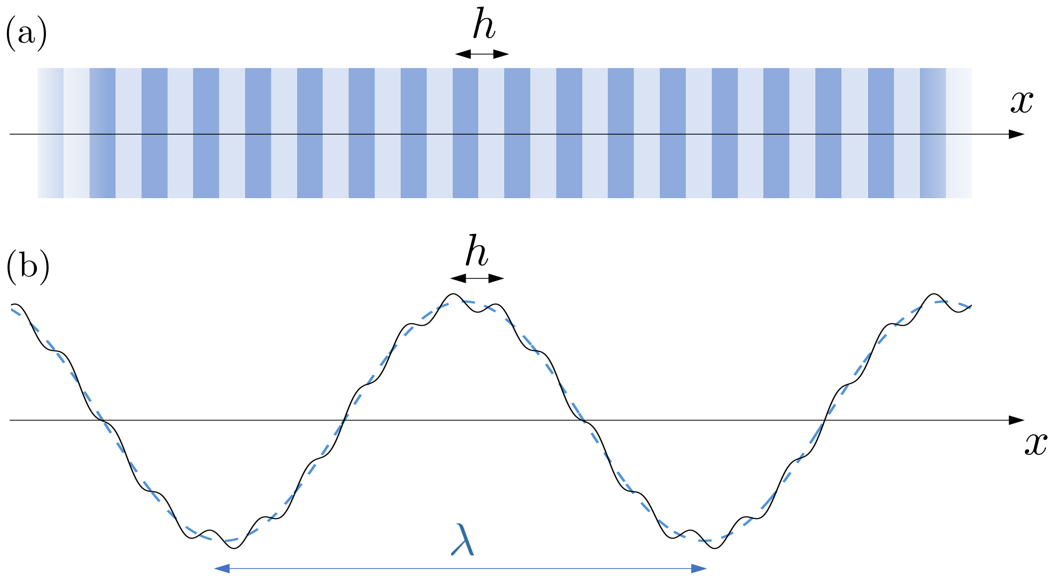

Fig. 1.3 (a) Periodically varying medium with material properties changing periodically with a period h. (b) Large scale variation λ (blue dashed curve) and variation of an actual field with a superimposed small perturbation h (plain black curve).

For simplicity, let us put the system in nondimensional form by introducing $x = k\mathrm{x}$

$$\begin{cases} (a(x)\eta'(x))' + b(x)\eta(x) = 0 \\ \eta(x),\ a(x)\eta'(x) \in C^0, \end{cases} \tag{1.46}$$

and now $f' = \mathrm{d}f/\mathrm{d}x$. This procedure lets us eradicate the wavenumber k. The parameters $a(x)$ and $b(x)$ are now periodic over x with period ϵ. Let us rewrite the problem, imposing

$$\begin{cases} u(x) = a(x)\eta'(x) \\ u'(x) + b(x)\eta(x) = 0 \\ u(x),\ \eta(x) \in C^0. \end{cases} \tag{1.47}$$

Now, we introduce two scales for homogenization. First, we associate the macroscopic scale x with the wavelength and the microscopic scale

$$\xi = \frac{x}{\epsilon} = \frac{\mathrm{x}}{h}. \tag{1.48}$$

We use expansions[1]

$$\begin{cases} \eta = \sum\limits_n \epsilon^n \eta^n = \eta^0(x,\xi) + \epsilon\eta^1(x,\xi) + \epsilon^2\eta^2(x,\xi) + \epsilon^3\eta^3(x,\xi) + \ldots \\ u = \sum\limits_n \epsilon^n u^n = u^0(x,\xi) + \epsilon u^1(x,\xi) + \epsilon^2 u^2(x,\xi) + \epsilon^3 u^3(x,\xi) + \ldots, \end{cases} \tag{1.49}$$

with the terms η^n and u^n being periodic with respect to ξ with period 1 on the interval $\xi \in (0,1)$. After changing the coordinates, the differential operator becomes

$$\frac{\mathrm{d}f(x,\xi)}{\mathrm{d}x} = \frac{\partial f(x,\xi)}{\partial x} + \frac{\partial \xi}{\partial x}\frac{\partial f(x,\xi)}{\partial \xi} \implies f' = \frac{\partial f}{\partial x} + \frac{1}{\epsilon}\frac{\partial f}{\partial \xi}. \tag{1.50}$$

Substituting (1.49) into (1.47) and having in mind that a and b depend only on microscopic scale ξ, we obtain

$$\begin{cases} u^0 + \epsilon u^1 + \epsilon^2 u^2 + \ldots = a(\xi)\left(\frac{\partial}{\partial x} + \frac{1}{\epsilon}\frac{\partial}{\partial x}\right)(\eta^0 + \epsilon\eta^1 + \epsilon^2\eta^2 + \ldots) \\ \left(\frac{\partial}{\partial x} + \frac{1}{\epsilon}\frac{\partial}{\partial x}\right)(u^0 + \epsilon u^1 + \epsilon^2 u^2 + \ldots) + b(\xi)(\eta^0 + \epsilon\eta^1 + \epsilon^2\eta^2 + \ldots) = 0. \end{cases} \tag{1.51}$$

---

[1] For η^n and u^n, n is the index placed at the top for clarity of writing. For the parameter ϵ^n, n is its power.

We can now write the equations for each order of the parameter ϵ. At the order $\mathcal{O}(-1)$ we have

$$\boxed{\epsilon^{-1}} \quad \begin{cases} a(\xi)\frac{\partial\eta^0}{\partial\xi} = 0 \\ \frac{\partial u^0}{\partial\xi} = 0 \end{cases} \quad \Longrightarrow \quad \begin{cases} \eta^0 = \eta^0(x) \\ u^0 = u^0(x), \end{cases} \tag{1.52}$$

from which we deduce that at the dominant order η^0 and u^0 do not see the variation due to the microstructure, i.e., depends only on x. At the order $\mathcal{O}(0)$ however, we have

$$\boxed{\epsilon^{0}} \quad \begin{cases} u^0 = a(\xi)\left(\frac{\partial\eta^0}{\partial x} + \frac{\partial\eta^1}{\partial\xi}\right) \\ \frac{\partial u^0}{\partial x} + \frac{\partial u^1}{\partial\xi} + b(\xi)\eta^0 = 0. \end{cases} \tag{1.53}$$

Now averaging (1.53) over $\xi \in (0,1)$ and taking advantage of the fact that u^0, η^0 are independent of ξ (1.52) and $u^1(x,\xi)$ is periodic, we can write

$$\begin{aligned} \int_0^1 \left(\frac{\partial u^0}{\partial x} + \frac{\partial u^1}{\partial\xi} + b(\xi)\eta^0\right) \mathrm{d}\xi = & \\ &= \frac{\partial u^0(x)}{\partial x} + \int_0^1 \frac{\partial u^1}{\partial\xi}\,\mathrm{d}\xi + \eta^0(x)\int_0^1 b(\xi)\,\mathrm{d}\xi = \\ &= \frac{\partial u^0(x)}{\partial x} + \underbrace{\left[u^1(x,1) - u^1(x,0)\right]}_{=0,\ \text{periodic over } \xi\in(0,1)} + \int_0^1 b(\xi)\,\mathrm{d}\xi = \\ &= \frac{\partial u^0(x)}{\partial x} + \langle b(\xi)\rangle\eta^0(x), \end{aligned}$$

where $\langle f\rangle = \int_0^1 f\,\mathrm{d}\xi$. Eventually

$$\frac{\partial u^0(x)}{\partial x} + \langle b\rangle\eta^0(x) = 0. \tag{1.54}$$

Continuing averaging (1.53) we have

$$\begin{aligned} u^0(x)\int_0^1 \frac{1}{a(\xi)}\,\mathrm{d}\xi = \int_0^1 \left(\frac{\partial\eta^0}{\partial x} + \frac{\partial\eta^1}{\partial\xi}\right)\mathrm{d}\xi &= \\ = \frac{\partial\eta^0(x)}{\partial x} + \int_0^1 \frac{\partial\eta^1}{\partial\xi}\,\mathrm{d}\xi &= \\ = \frac{\partial\eta^0(x)}{\partial x} + \underbrace{\left[\eta^1(x,1) - \eta^1(x,0)\right]}_{=0,\ \text{periodic over } \xi\in(0,1)}&. \end{aligned}$$

Hence, we obtain

$$u^0(x) = \left\langle \frac{1}{a} \right\rangle^{-1} \frac{\partial \eta^0(x)}{\partial x}. \tag{1.55}$$

Substituting (1.55) into (1.54) and coming back to the original variables with dimensions we obtain an **effective problem** at the dominant order on $\eta(\mathrm{x})$

$$\boxed{\eta'' + \langle a^{-1} \rangle \langle b \rangle k^2 \eta = 0}. \tag{1.56}$$

1.5.2 Homogenization of 2D shallow water equation

Having shown the idea of homogenization technique for the 1D case for the wave equation, we can now proceed with two-scale homogenization of the 2D shallow water equation with a stratified medium. The goal of this section is to transform the shallow water equation into its anisotropic form with constant effective parameters h_x and h_y, i.e.,

$$\nabla \cdot [h(\mathrm{x}, \mathrm{y}) \nabla \eta] + \frac{\omega^2}{g} \eta = 0 \quad \xrightarrow{\text{homogenization}} \quad \nabla \cdot \left[\begin{pmatrix} h_x & 0 \\ 0 & h_y \end{pmatrix} \nabla \eta \right] + \frac{\omega^2}{g} \eta = 0.$$

This approach allows to design a metamaterial structure, i.e., a periodic array of stratified plates, that create the anisotropy needed to control the water wave propagation. In this particular case we introduce h_1 and h_2 as alternating water depths along x (Fig. 1.4).

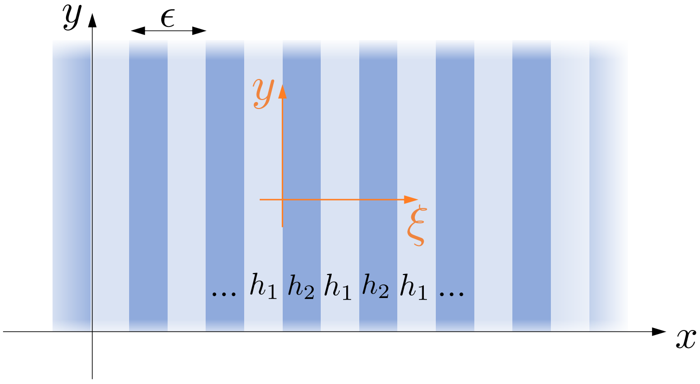

Fig. 1.4 Alternating water depths h_1 and h_2.

Let us rewrite the problem according to the previous assumptions in the similar fashion as in the previous Section 1.5.1

$$\begin{cases} \mathbf{u} = h(x)\nabla\eta \\ \nabla\cdot\mathbf{u} + \frac{\omega^2}{g}\eta = 0 \\ \mathbf{u},\, \eta \in C^0, \end{cases} \tag{1.57}$$

where $\mathbf{u} = [u_x\ u_y]^T$.

Introducing the microscopic scale $\xi = x/\epsilon$, where $\epsilon \ll 1$ and the wavelength is of the order $\lambda = \mathcal{O}(1)$, we shall adjust the differential operators

$$\begin{aligned} \nabla &\to \nabla + \frac{\mathbf{e}_x}{\epsilon}\frac{\partial}{\partial\xi}, \\ \nabla\cdot\mathbf{u} &\to \nabla\cdot\mathbf{u} + \frac{1}{\epsilon}\frac{\partial u_x}{\partial\xi}, \end{aligned} \tag{1.58}$$

where $\mathbf{e}_x$ denotes a unit vector along x axis. We use expansions[2]

$$\begin{cases} \eta = \sum\limits_n \epsilon^n\eta^n = \eta^0(x,y,\xi) + \epsilon\eta^1(x,y,\xi) + \epsilon^2\eta^2(x,y,\xi) + \epsilon^3\eta^3(x,y,\xi) + \ldots \\ \mathbf{u} = \sum\limits_n \epsilon^n\mathbf{u}^n = \mathbf{u}^0(x,y,\xi) + \epsilon\mathbf{u}^1(x,y,\xi) + \epsilon^2\mathbf{u}^2(x,y,\xi) + \epsilon^3\mathbf{u}^3(x,y,\xi) + \ldots, \end{cases} \tag{1.59}$$

where $\eta^n = \eta^n(x,y,\xi)$ and $\mathbf{u}^n = \mathbf{u}^n(x,y,\xi)$ are periodic functions over an interval $\xi \in (0,1)$. Substituting (1.59) to (1.57) and making use of (1.58) we get

$$\begin{cases} \mathbf{u}^0 + \epsilon\mathbf{u}^1 + \epsilon^2\mathbf{u}^2 + \ldots = h(\xi)\left(\nabla + \frac{\mathbf{e}_x}{\epsilon}\frac{\partial}{\partial\xi}\right)(\eta^0 + \epsilon\eta^1 + \epsilon^2\eta^2 + \ldots) \\ \nabla\cdot(\mathbf{u}^0 + \epsilon\mathbf{u}^1 + \epsilon^2\mathbf{u}^2 + \ldots) + \frac{1}{\epsilon}\frac{\partial}{\partial\xi}(u_x^0 + \epsilon u_x^1 + \epsilon^2 u_x^2 \ldots) + \frac{\omega^2}{g}(\eta^0 + \epsilon\eta^1 + \ldots) = 0. \end{cases} \tag{1.60}$$

It is straightforward to verify that at the order $\mathcal{O}(-1)$ we have

$$\boxed{\epsilon^{-1}} \quad \begin{cases} h(\xi)\mathbf{e}_x\frac{\partial\eta^0}{\partial\xi} = 0 \\ \frac{\partial u_x^0}{\partial\xi} = 0 \end{cases} \quad \Longrightarrow \quad \begin{cases} \eta^0 = \eta^0(x,y) \\ u_x^0 = u_x^0(x,y). \end{cases} \tag{1.61}$$

It allows to conclude that at the dominant order η^0 and u_x^0 do not see the variation of the microstructure, i.e., depend only on the macroscopic x and y. At the order $\mathcal{O}(0)$,

---

[2] For η^n and $\mathbf{u}^n$, n is the index placed at the top for clarity of writing. For the parameter ϵ^n, n is its power.

we get

$$\boxed{\epsilon^0} \qquad \begin{cases} \mathbf{u}^0 = h(\xi)\left(\nabla\eta_0 + \mathbf{e}_x \frac{\partial\eta^1}{\partial\xi}\right) \\ \nabla\cdot\mathbf{u}^0 + \frac{\partial u_x^1}{\partial\xi} + \frac{\omega^2}{g}\eta_0 = 0, \end{cases} \tag{1.62}$$

which can be rewritten as

$$\boxed{\epsilon^0} \qquad \begin{cases} u_x^0 = h(\xi)\left(\frac{\partial\eta^0}{\partial x} + \frac{\partial\eta^1}{\partial\xi}\right) \\ u_y^0 = h(\xi)\frac{\partial\eta^0}{\partial y} \\ \frac{\partial u_x^0}{\partial x} + \frac{\partial u_y^0}{\partial y} + \frac{\partial u_x^1}{\partial\xi} + \frac{\omega^2}{g}\eta_0 = 0. \end{cases} \tag{1.63}$$

Now averaging (1.63) over $\xi \in (0,1)$, taking advantage of the fact that u_x^0, η^0 are independent of ξ (1.61), η^1 is periodic, and dividing by $h(\xi)$ we can write

$$\begin{aligned} u_x^0(x,y)\int_0^1 \frac{1}{h(\xi)}\,\mathrm{d}\xi &= \int_0^1 \left(\frac{\partial\eta^0}{\partial x} + \frac{\partial\eta^1}{\partial\xi}\right)\mathrm{d}\xi = \\ &= \frac{\partial\eta^0(x,y)}{\partial x} + \int_0^1 \frac{\partial\eta^1}{\partial\xi}\,\mathrm{d}\xi = \\ &= \frac{\partial\eta^0(x,y)}{\partial x} + \underbrace{\Big[\eta^1(x,y,1) - \eta^1(x,y,0)\Big]}_{=0,\text{ periodic over }\xi\in(0,1)}, \end{aligned}$$

$$\begin{aligned} u_y^0(x,y) &= \int_0^1 \left(h(\xi)\frac{\partial\eta^0}{\partial y}\right)\mathrm{d}\xi = \\ &= \frac{\partial\eta^0(x,y)}{\partial y}\int_0^1 h(\xi)\,\mathrm{d}\xi. \end{aligned}$$

Ultimately it gives

$$\begin{aligned} u_x^0 &= \langle h^{-1}\rangle^{-1}\frac{\partial\eta^0}{\partial x}, \\ u_y^0 &= \langle h\rangle\frac{\partial\eta^0}{\partial y}. \end{aligned} \tag{1.64}$$

By substituting (1.64) into averaged (1.63) and having in mind that $\int_0^1 \partial u_x^1/\partial\xi\,\mathrm{d}\xi = 0$, by periodicity, we obtain

$$\frac{\partial}{\partial x}\langle h^{-1}\rangle^{-1}\frac{\partial\eta^0}{\partial x} + \frac{\partial}{\partial y}\langle h\rangle\frac{\partial\eta^0}{\partial y} + \frac{\omega^2}{g}\eta^0 = 0, \tag{1.65}$$

that can be written as

$$\boxed{\nabla \cdot \left[\begin{pmatrix} \langle h^{-1} \rangle^{-1} & 0 \\ 0 & \langle h \rangle \end{pmatrix} \nabla \eta^0 \right] + \frac{\omega^2}{g} \eta^0 = 0,} \tag{1.66}$$

where the volume average $\langle h \rangle = \int_0^1 h \, \mathrm{d}\xi = \theta h_1 + (1 - \theta) h_2$, θ being the filling fraction of the layers. The equation (1.66) is the **effective equation** at the dominant order for a stratified medium (Fig. 1.4) that eventually allows to design it for a desired degree of anisotropy.

This classical approach, based on the two-dimensional shallow water equation, is advantageous in various contexts. However, it has been shown that it cannot account for the three-dimensional near field effects of the stratified medium [48]. To accurately catch these effects, the homogenization of a three-dimensional problem has to be used [49, 50]. This issue is addressed later in Chapter 3.

Chapter 2

Experimental methods

Experimental studies of water wave phenomena require appropriate equipment and measurement techniques. The accurate reconstruction of free surface displacement, which reveals the inherent characteristics of the flow, is crucial.

In the last decades many techniques have been developed based on, *inter alia* determination of the wave gradient [51, 52], diffusing light photography [53], optical flow method [54], and many others. Unfortunately, each of these methods suffers from certain limitations and cannot always be applied to the study of water waves, especially for systems with variable bathymetry that we study in this thesis. The major drawbacks include, i.e., the measurement in only a few points, the intrusive character of the method, the complicated multi-camera system, or the need for integration of the wave's gradient field that might lead to error accumulation.

Precise measurements of free surface deformation on a laboratory scale necessitate methods that are nonintrusive and offer high temporal and spatial resolution. Here, we present two techniques that are used throughout this thesis and allow to reconstruct the wavefield efficiently and, most importantly, with high accuracy.

2.1 Fourier transform profilometry

A Fourier transform profilometry technique (FTP) allows to recover full three-dimensional wavefield. Originally used to retrieve the shape of solid bodies [55, 56], it was later on employed to the fluid surface deformation reconstruction [57]. The principle of this technique is fairly straightforward. The fringe pattern of known properties is projected onto the surface using a video projector that is placed above at a distance L and whose optical axis is perpendicular to the flat reference surface (Fig. 2.1). First, the reference image is taken by a camera whose optical axis is parallel to the one of the projector,

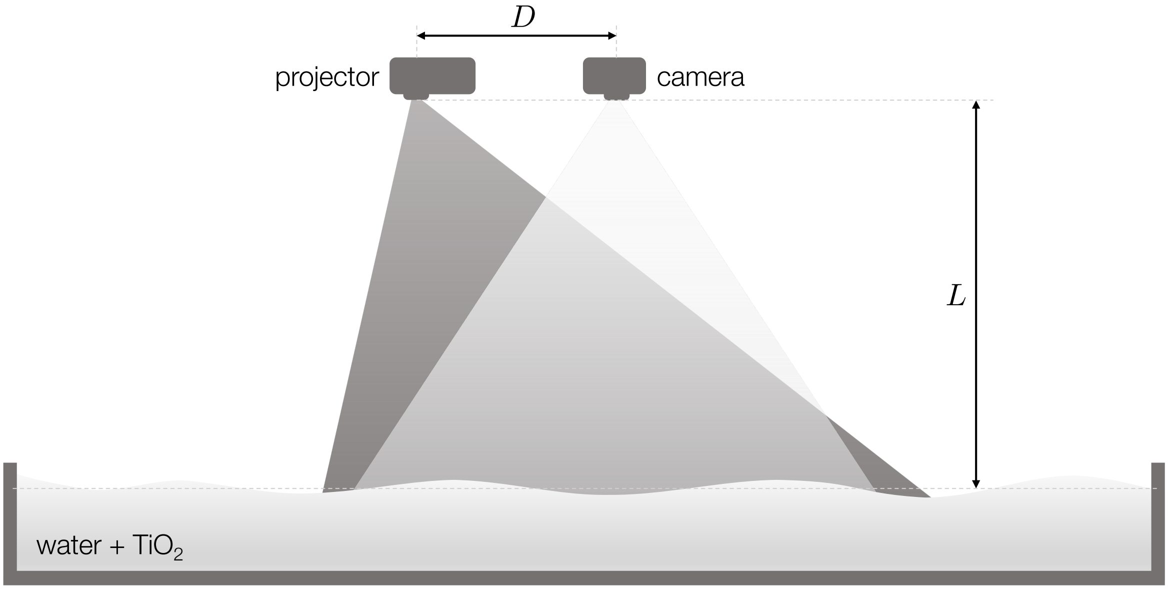

Fig. 2.1 Typical experimental setup needed for FTP measurements.

and the distance between them is known (D). The intensity of the reference image I_0 can be represented by

$$I_0(x,y) = A(x,y)\left(k_P x + \varphi_0(x)\right) + B(x,y), \tag{2.1}$$

where $k_P = 2\pi/\lambda_P$ with λ_P being the wavelength of the projected pattern. $A(x,y)$ and $B(x,y)$ represent the undesirable variation of the image intensity usually coming from the inhomogeneous illumination of the measured surface or the locally decreased reflectivity of the surface itself. In order to get rid of these, another image I_B is taken, where instead of the fringe pattern, the homogenous background is projected

$$I_B(x,y) = B(x,y). \tag{2.2}$$

Later on, the deformed surface is examined, which results in the deformation of the projected fringes and can be mathematically described as

$$I(x,y) = A(x,y)\left(k_P x + \varphi(x)\right) + B(x,y). \tag{2.3}$$

The difference of the measured phases $\Delta\varphi = \varphi(x) - \varphi_0(x)$ contains the information about the out-of-plane deformation of the surface and shall be extracted from the registered images. To do so, we perform a Hilbert transform of the recorded images I_0

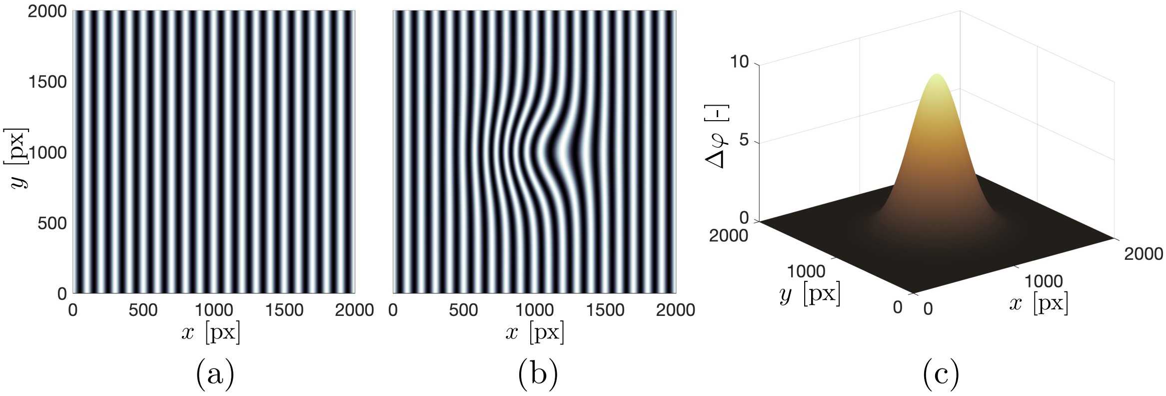

Fig. 2.2 Synthetic recovery of the phase difference. (a) Reference image I_0. (b) Image of a deformed surface I. (c) Recovered phase difference $\Delta\varphi$.

and I, from which the background intensity I_B is subtracted

$$\mathcal{H}(I_0 - I_B) = A(x,y)\exp[\mathrm{i}(k_P x + \phi_0(x))], \tag{2.4}$$

$$\mathcal{H}(I_0 - I_B) = A(x,y)\exp[\mathrm{i}(k_P x + \phi(x))], \tag{2.5}$$

where i is the imaginary unit. Now, it is straightforward to obtain the phase difference $\Delta\varphi$ by taking the imaginary part of the following expression

$$\ln[\mathcal{H}(I_0 - I_B)\cdot\mathcal{H}^*(I_0 - I_B)] = \ln|A|^2 + \mathrm{i}\Delta\varphi. \tag{2.6}$$

This approach allows to obtain $\Delta\varphi$ and fully weed out the unwanted intensity variations $A(x,y)$ and $B(x,y)$. The next step is to find the direct relation between the phase difference $\Delta\varphi$ and the surface elevation $\eta(x,y)$. This problem can be addressed using geometrical optics. Ultimately, we obtain the so-called phase-to-height ratio [58, 59, 56, 60]

$$\eta(x,y) = \frac{\Delta\varphi L}{\Delta\varphi - k_P D}, \tag{2.7}$$

from which the desired surface deformation is obtained. A synthetic example for a phase difference recovery is shown in Fig. 2.2. Here, the coefficients $A = 1$ and $B = 0$. The warp of the fringes due to the deformed surface is clearly visible (Fig. 2.2b). The imposed phase difference (Fig. 2.2c) matches exactly the recovered one.

When it comes to the application of this technique to the water surface waves measurements, particular difficulty arises since it requires diffusive reflection of light on the liquid surface. We shall ensure the reflectivity of the inherently transparent water surface without changing its physical properties that could have a detrimental effect on the studied phenomena. It has been shown that the use of titanium dioxide (TiO_2) as a pigment allows to avoid undesirable effects, especially the increase of attenuation that happens using other pigments or paint [61]. Sedimentation of the titanium dioxide particles is relatively slow unless they aggregate. When the surface is measured, this phenomenon could lead to the change of the plane in which the measurement is taken. To prevent the sedimentation and aggregation of the particles, we use clean deionized water.

In order to calibrate the method, we use a triangular wedge of known dimensions (Fig. 2.3). This way, we can verify the measured parameters L, D, and k_P. To translate the pixels into meters, we take a picture of a $1 \times 1\,\mathrm{cm}^2$ grid placed at the level of the reference plane. The spatial and temporal resolution of the method depend solely on the camera parameters. Typically, we use the image resolution of $2048 \times 2048\,\mathrm{px}^2$, with the resulting pixel size of 0.25 mm/px. The usual camera frame rate is set to 50 fps and corresponds to a sufficient number of points recorded in the time domain for a water surface wave of a given frequency.

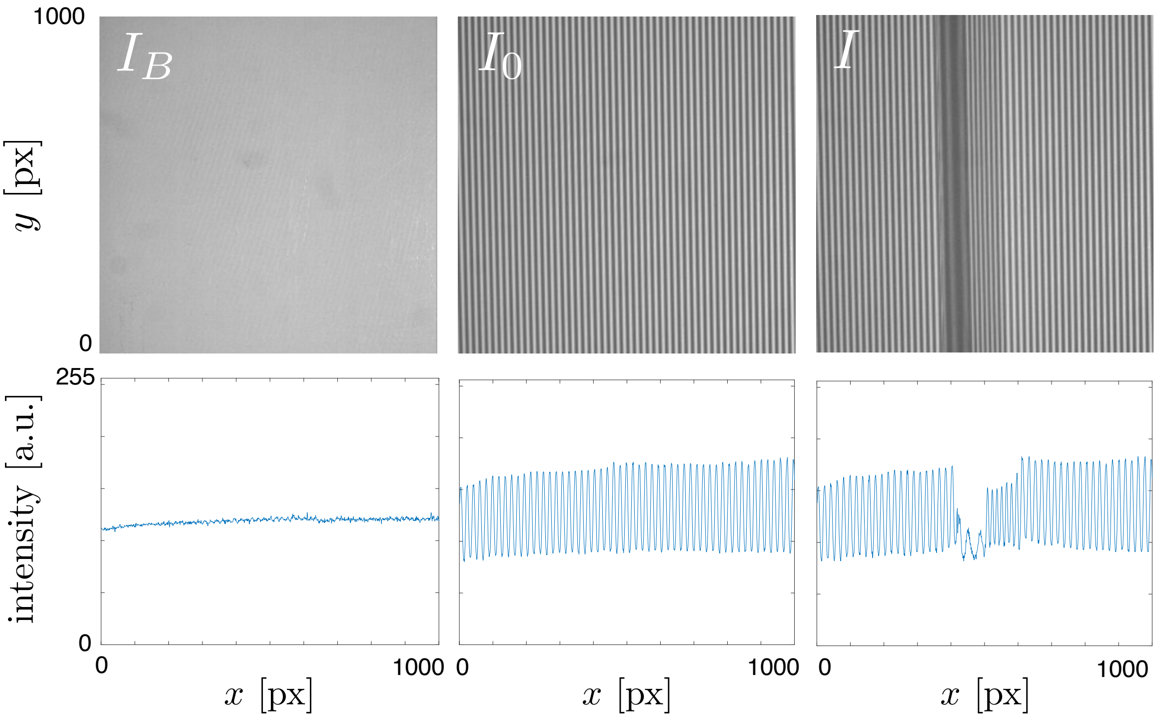

Fig. 2.3 The top panel represents typical images from the FTP technique (an example for a calibration wedge). The bottom panel shows corresponding intensity profiles through the centerline.

2.2 Confocal chromatic measuring

For even more precise measurements, confocal displacement sensors are used. Even though one sensor allows to measure the displacement at one point at a time, it offers a significant advantage compared to the previously described Fourier transform profilometry technique. Thanks to the confocal chromatic measuring principle, the sensor is able to measure the distance of a transparent object, in our case - the water surface. That is why the fluid does not have to be dyed in any way. Notably, compared to FTP, titanium dioxide does not have to be used. Moreover, sensors of this type are capable of detecting several layers of transparent material. In our experiments, this possibility is acknowledged to measure not only the vertical displacement of a free surface but also to determine with very high precision the water depth or thickness of a fluid layer which is of great importance when it comes to the repeatability of successive measurements.

The principle of confocal chromatic measurement is based on emitting a white polychromatic beam onto the target surface. Owing to a system of multiple optical lenses, the white light is dispersed into monochromatic beams (Fig. 2.4) by controlled chromatic deviation, which is assigned to each wavelength. Only the light at wavelengths that are perfectly focused on a target surface is used for the measurement. Reflected beams pass through an optical fiber to a spectrometer, then are split by wavelength and focused onto a CMOS image sensor. Furthermore, due to the fact that the emitter and receiver are arranged in the same axis, shadowing is avoided, which is a major drawback of regular laser triangulation sensors.

In our experiments two sensor heads Keyence CL-P070 are used along with the controller and optical unit [62]. This system allows to measure the distance or depth up to 70 mm and its resolution is equal to 0.25 μm.

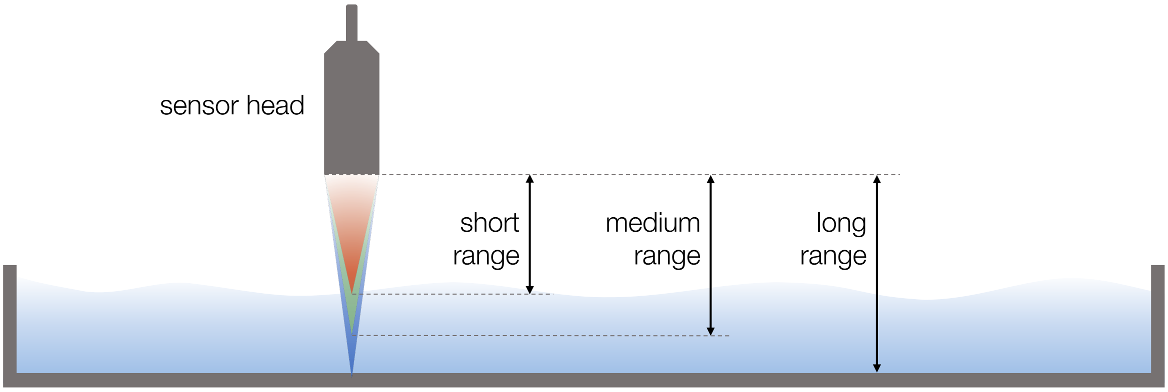

Fig. 2.4 Simplified scheme of the confocal chromatic measuring principle.

Chapter 3

Metabathymetry. Regular modes in irregular cavities

3.1 Motivation

It has been shown that water wave metamaterials can be used to redirect the wave and create reflectionless waveguide [32, 39]. However, the presented approach is limited by the degree of the deformation of the channel. The higher the deformation, the less effective the metamaterial structure becomes. Recent developments in the field have led to the conclusion that water wave metamaterials can produce a much higher level of anisotropy than predicted by the usual approach found in related problems for electromagnetic or acoustic waves [48]. Less attention has been devoted to sloshing dynamics, where resonance properties of a cavity strongly depend on its geometry yielding phenomena such as high spots [63, 64].

We benefit from these findings to create a metamaterial cavity whose deformation is *invisible* for the water wave even for a high degree of the bend (Fig. 3.1). To establish the effectiveness of the cloaking, we study the eigenmodes and eigenfrequencies of the cavity before and after the deformation, expecting that the behavior of the wave remains unchanged. In this case, the periodic, subwavelength structure that serves as a medium in which the water wave propagates (*metamaterial*) is put at the bottom of the cavity to change its shape (*bathymetry*) (Fig. 3.2). That is how the term **metabathymetry** is conceived to describe this particular ensemble of layered plates.

Mathematical approaches to metamaterial design vary significantly throughout the disciplines and the category of waves it serves. In this chapter we benefit from the coordinate transformation theory [9, 65] and the homogenization of the fully three-dimensional water wave problem [48, 36, 66].

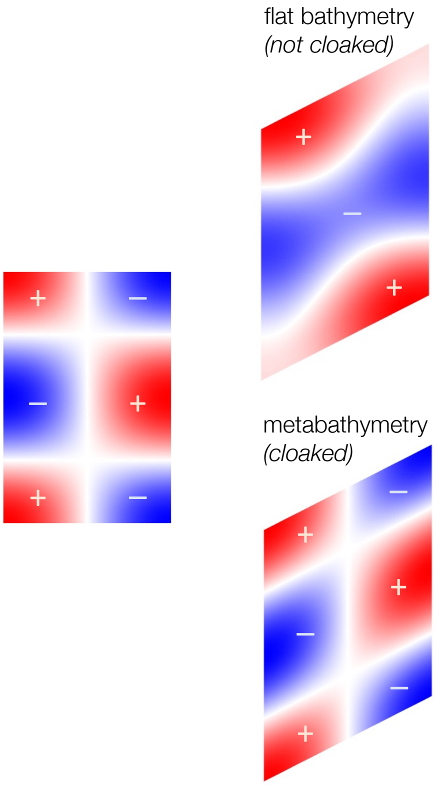

Fig. 3.1 Example of a rectangular cavity eigenmode (left) and its equivalent in a irregular cavity with and without cloaking (right).

Fig. 3.2 Top view of the deformed cavity with metabathymetry.

3.2 Geometric transformation of shallow water equation

Situations in fluid dynamics where the horizontal length scale is much greater than the vertical length scale are common, so the shallow water equations are widely applicable, e.g., they are used with Coriolis forces in atmospheric and oceanic modeling, as a simplification of the primitive equations of atmospheric flow. In our case, assuming harmonic regime, we can write that

$$\nabla \cdot (h\nabla\eta) + \frac{\omega^2}{g}\eta = 0, \tag{3.1}$$

where $h = h(x, y)$ stands for slowly varying water depth (where the wavelength $\lambda \gg h$), η is the vertical displacement of a free surface, ω is the angular frequency, and g is the gravitational acceleration. We assume the shallow water limit ($kh_0 \ll 1$), where the wavenumber k is given through the dispersion relation $\omega^2 = gh_0k^2$. However, in the case of periodic metabathymetry we cannot assume that the bathymetry is slowly varying. The homogenization technique for this problem is presented in the next sections. First, let us show that the shallow water equation under the change of coordinates preserves its form, i.e., of Helmholtz type, which is a crucial condition to a successful design of the metabathymetry. We consider the two dimensional shallow water equation in the form

$$\begin{aligned} &\nabla \cdot (h\nabla\eta) + \gamma\eta = 0 \\ &\mathbf{n} \cdot \nabla\eta = 0 \text{ on } \partial\Omega, \end{aligned} \tag{3.2}$$

defined in the virtual space (X, Y), where $\gamma = \omega^2/g$ denotes a constant introduced for clarity of writing, $\partial\Omega$ is the boundary, $\mathbf{n}$ stands for the vector normal to it, and $\nabla = [\partial/\partial X \ \partial/\partial Y]^T$. Multiplying the equation by an arbitrary test function $\psi \in H^1$, we can obtain a variational (weak) formulation of the problem:

$$\int_\Omega \nabla \cdot (h\nabla\eta)\,\psi \,\mathrm{d}X\,\mathrm{d}Y + \int_\Omega \gamma\eta\psi \,\mathrm{d}X\,\mathrm{d}Y = 0.$$

Using Green's first identity we obtain

$$-\int_\Omega (h\nabla\eta)^T \nabla\psi \,\mathrm{d}X\,\mathrm{d}Y + \int_{\partial\Omega} \mathbf{n} \cdot (h\nabla\eta)^T \psi \,\mathrm{d}S + \int_\Omega \gamma\eta\psi \,\mathrm{d}X\,\mathrm{d}Y = 0.$$

Taking advantage of the homogenous boundary condition (3.2), we can eliminate the boundary term and simply write that

$$-\int_{\Omega} (h\nabla\eta)^T \,\nabla\psi \,\mathrm{d}X\,\mathrm{d}Y + \int_{\Omega} \gamma\eta\psi \,\mathrm{d}X\,\mathrm{d}Y = 0. \tag{3.3}$$

Now, by changing variables from virtual (X, Y) to real (x, y) space, the gradient operator $\nabla = [\partial/\partial X \;\, \partial/\partial Y]^T$ becomes

$$\begin{aligned} \frac{\partial}{\partial X} &= \frac{\partial x}{\partial X}\frac{\partial}{\partial x} + \frac{\partial y}{\partial X}\frac{\partial}{\partial y}, \\ \frac{\partial}{\partial Y} &= \frac{\partial x}{\partial Y}\frac{\partial}{\partial x} + \frac{\partial y}{\partial Y}\frac{\partial}{\partial y}. \end{aligned}$$

Defining the Jacobian of the above transformation as

$$\mathbf{J} = \begin{bmatrix} \frac{\partial x}{\partial X} & \frac{\partial y}{\partial X} \\ \frac{\partial y}{\partial X} & \frac{\partial y}{\partial Y} \end{bmatrix},$$

we can write that

$$\nabla = \mathbf{J}^T \nabla_{xy}, \quad \text{where} \quad \nabla_{xy} = [\partial/\partial x \;\, \partial/\partial y]^T.$$

Then, knowing that

$$\begin{aligned} \mathrm{d}x &= \frac{\partial x}{\partial X}\,\mathrm{d}X + \frac{\partial y}{\partial X}\,\mathrm{d}Y, \\ \mathrm{d}y &= \frac{\partial x}{\partial Y}\,\mathrm{d}X + \frac{\partial y}{\partial Y}\,\mathrm{d}Y, \end{aligned}$$

we can define the relation between the products of exact differentials in real and virtual space using properties of exterior (wedge) product

$$\mathrm{d}x \wedge \mathrm{d}y = \left(\frac{\partial x}{\partial X}\,\mathrm{d}X + \frac{\partial y}{\partial X}\,\mathrm{d}Y\right) \wedge \left(\frac{\partial x}{\partial Y}\,\mathrm{d}X + \frac{\partial y}{\partial Y}\,\mathrm{d}Y\right),$$

which after reduction becomes

$$\mathrm{d}X \wedge \mathrm{d}Y = \frac{\mathrm{d}x \wedge \mathrm{d}y}{\det \mathbf{J}}. \tag{3.4}$$

On combining this result (3.4) with (3.3) and again integrating by parts, we conclude that

$$\int_{\Omega} \left(\nabla_{xy} \cdot \left(\frac{\mathbf{J} h \mathbf{J}^T}{\det \mathbf{J}} \nabla_{xy} \eta \right) + \frac{\gamma \eta}{\det \mathbf{J}} \right) \psi \, \mathrm{d}x \, \mathrm{d}y - \int_{\partial\Omega} \mathbf{n} \cdot \left(\frac{\mathbf{J} h \mathbf{J}^T}{\det \mathbf{J}} \nabla_{xy} \eta \right) \psi \, \mathrm{d}S = 0.$$

Since $\psi \in H^1$ is an arbitrary function, we can choose ψ such that it is equal to zero in the bulk and nonzero on the border or *vice versa*. Having in mind that $\gamma = \omega^2/g$, this fact allows to write

$$\begin{aligned} \nabla_{xy} \cdot \left(\frac{\mathbf{J} h \mathbf{J}^T}{\det \mathbf{J}} \nabla_{xy} \eta \right) + \frac{\omega^2}{g \det \mathbf{J}} \eta = 0, \\ \mathbf{n} \cdot \left(\frac{\mathbf{J} h \mathbf{J}^T}{\det \mathbf{J}} \nabla_{xy} \eta \right) = 0 \text{ on } \partial\Omega, \end{aligned} \tag{3.5}$$

which shows the invariant quality of the form of the shallow water equation to the change of coordinates.

3.3 Cavity design and homogenization

Let us consider the 2D SWE in a virtual space (X, Y)

$$\begin{aligned} \nabla_{XY} \cdot (h_0 \nabla_{XY} \eta) + \frac{\omega^2}{g} \eta = 0, \\ \mathbf{n} \cdot \nabla_{XY} \eta = 0 \text{ on } \partial\Omega, \end{aligned} \tag{3.6}$$

where h_0 is the reference water depth, η is the vertical displacement of a free surface, ω is the angular frequency, g is the gravitational acceleration, $\partial\Omega$ is the boundary, $\mathbf{n}$ is the vector normal to it, and $\nabla_{XY} = (\partial/\partial X,\, \partial/\partial Y)^T$. We assume shallow water limit ($kh_0 \ll 1$), where the wavenumber k is given through the dispersion relation $\omega^2 = g h_0 k^2$. Now, applying geometrical transformation from virtual (X, Y) to real (x, y) space, as shown in Section 3.2, we obtain

$$\begin{aligned} \nabla \cdot \left(\frac{\mathbf{J} h_0 \mathbf{J}^T}{\det \mathbf{J}} \nabla \eta \right) + \frac{\omega^2}{g \det \mathbf{J}} \eta = 0, \\ \mathbf{n} \cdot \left(\frac{\mathbf{J} h_0 \mathbf{J}^T}{\det \mathbf{J}} \nabla \eta \right) = 0 \text{ on } \partial\Omega, \end{aligned} \tag{3.7}$$

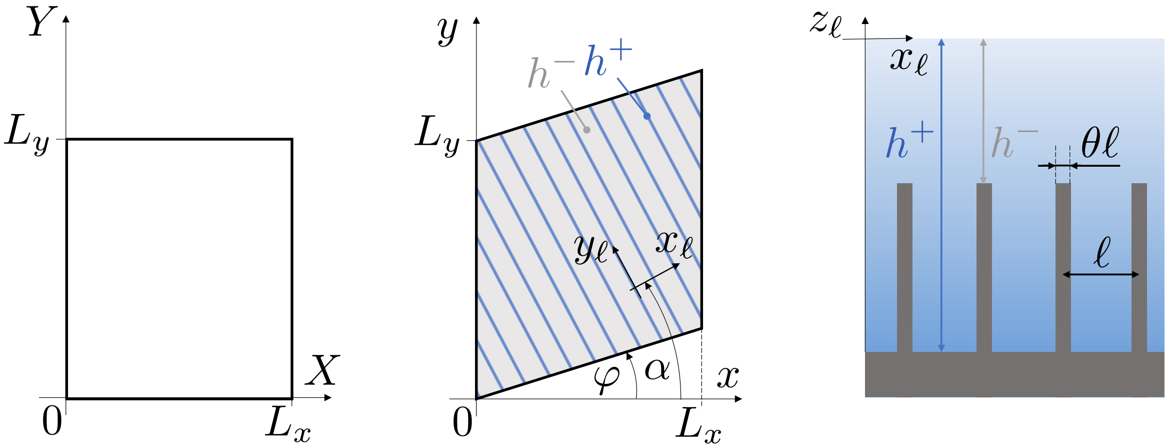

(a) (b) (c)

Fig. 3.3 (a) The cavity in the virtual space (X, Y), i.e., before coordinate transformation with width L_x and height L_y. (b) The cavity in the real space (x, y), i.e., after coordinate transformation with bending angle φ, with a local coordinate system of the metabathymetry with a rotation angle α (note a misprint in [32]). (c) Section scheme of the metabathymetry. The subwavelength structure consists of periodic layers with thickness $\theta\ell$, water depths h^+ and h^-, and periodicity ℓ.

where $\mathbf{J}$ stands for the Jacobian matrix of the transformation, and now $\nabla = (\partial/\partial x,\ \partial/\partial y)^T$. The 2D SWE preserves its form, i.e., of Helmholtz type. Due to the fact that g is not tunable in conventional conditions, we need a volume preserving (nonmagnetic) transformation ($\det \mathbf{J} = 1$). We choose a simple shear deformation of the cavity, which leads to the change of coordinates $x = X$, $y = \tan\varphi X + Y$, and whose Jacobian matrix is

$$\mathbf{J} = \begin{bmatrix} 1 & 0 \\ \tan\varphi & 1 \end{bmatrix}. \tag{3.8}$$

By changing the coordinates (Fig. 3.3), the anisotropy is introduced (3.7) and has to be realized in practice. To do so, we insert a particularly oriented anisotropic medium (with an angle α) with different effective water depths in x and y directions, i.e., h_x and h_y. We obtain

$$\nabla \cdot \left(\mathbf{R}_\alpha \mathbf{h} \mathbf{R}_\alpha^T \nabla\eta\right) + \frac{\omega^2}{g}\eta = 0, \quad \text{where} \quad \mathbf{h} = \begin{bmatrix} h_x & 0 \\ 0 & h_y \end{bmatrix}, \tag{3.9}$$

and $\mathbf{R}_\alpha$ is the conventional rotation matrix with a rotation through an angle α with respect to x axis (Fig. 3.3b).

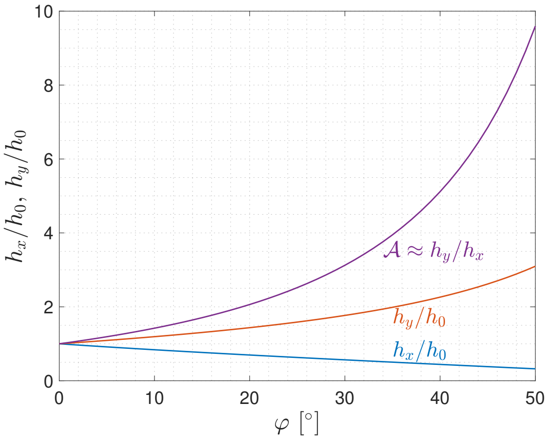

Fig. 3.4 Effective parameters h_x, h_y as functions of the angle φ.

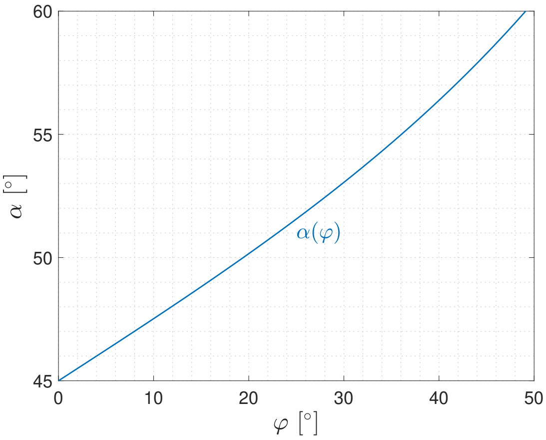

Fig. 3.5 Angle of rotation α as a function of the angle φ.

Now, by identifying (3.7) and (3.9), and having in mind the geometry of the cavity (3.8), we obtain explicit formulae for the water depths h_x, h_y, and the rotation angle α as functions of bending angle φ and the reference water depth h_0. Hence, the depths h_x, h_y, and the angle α are such that (note a misprint in [32])

$$\begin{aligned} h_x &= \frac{h_0}{2}(2 + \tan^2\varphi - \tan\varphi\sqrt{2+\tan^2\varphi}), \\ h_y &= \frac{h_0}{2}(2 + \tan^2\varphi + \tan\varphi\sqrt{2+\tan^2\varphi}), \\ \tan 2\alpha &= -2/\tan\varphi. \end{aligned} \tag{3.10}$$

It has been shown that the effective anisotropy, being the result of the presence of the metabathymetry, cannot be inferred from the shallow water equation even in the shallow water regime, as 3D effects affect the flow over a rapidly varying bathymetry due to the strong impact of the evanescent field [36, 48, 49]. Thus, the modelling, which predicts that the effective water depth tensor is related to the arithmetic and geometric averages (Section 1.5.2) of the actual water depths

$$h_x = \langle h^{-1}\rangle^{-1}, \quad h_y = \langle h\rangle, \tag{3.11}$$

underestimates the degree of the anisotropy due to the metabathymetry ($\langle h\rangle = \theta h^- + (1-\theta)h^+$, where θ is the filling fraction of the layers, Fig. 3.3). To properly model the aforementioned effects, the homogenization of the full 3D linear water wave problem must be used. Considering harmonic regime with time dependence $e^{i\omega t}$, assuming that the fluid is inviscid and incompressible, and knowing that the flow is irrotational, the velocity potential $\phi(x_\ell, y_\ell, z_\ell)$ satisfies

$$\begin{aligned}\triangle\phi &= 0,\\ \frac{\partial\phi}{\partial z_l} &= \frac{\omega^2}{g}\phi \text{ at } z_l = 0,\\ \mathbf{n}\cdot\nabla\phi &= 0 \text{ on } \Gamma,\end{aligned} \tag{3.12}$$

where Γ is the nonflat bottom, $\mathbf{n}$ is the vector normal to it, and $z_l = 0$ corresponds to the unperturbed free surface. Following the homogenization process as presented in [48–50] we obtain the cell problem defined with respect to undimensionalized variables

$$(x_r, z_r) = \left(\frac{x_\ell}{\ell}, \frac{z_\ell}{\ell}\right), \tag{3.13}$$

defined at the microscopic scale $\epsilon = \omega\sqrt{\ell/g} \ll 1$. Thus, the potential Φ in the unit cell Y (Fig. 3.6) satisfies

$$\begin{aligned}\triangle\Phi &= 0,\\ \frac{\partial\Phi}{\partial z_r} &= 0 \text{ at } z_r = 0,\\ \mathbf{n}\cdot\nabla\Phi &= 0 \text{ on } \Gamma,\\ \Phi\left(\frac{1}{2}, z_r\right) &= \Phi\left(-\frac{1}{2}, z_r\right) + 1,\\ \frac{\partial\Phi}{\partial x_r}\left(\frac{1}{2}, z_r\right) &= \frac{\partial\Phi}{\partial x_r}\left(-\frac{1}{2}, z_r\right).\end{aligned} \tag{3.14}$$

As shown in [48–50], the effective water depths h_x and h_y derived from a fully three dimensional problem (3.14) are of the form

$$h_x = \ell\int_Y \frac{\partial\Phi}{\partial x_r}\mathrm{d}Y, \quad h_y = \langle h\rangle, \tag{3.15}$$

where ℓ is the periodicity of the metabathymetry and Y is a unit cell with only one layer of the structure. Comparing (3.11) to (3.15), it comes into view that only h_x is affected by 3D near field effects. It has been shown that h_x in (3.15) might be much smaller than $\langle h^{-1}\rangle^{-1}$ predicted by 2D approach. As a consequence, the resulting anisotropy can be much larger than the one predicted by the classical homogenization of layered media.

The determination of h_x (3.15) is done by solving a cell problem of the homogenized three dimensional water wave problem (3.14). The solution can be provided by using

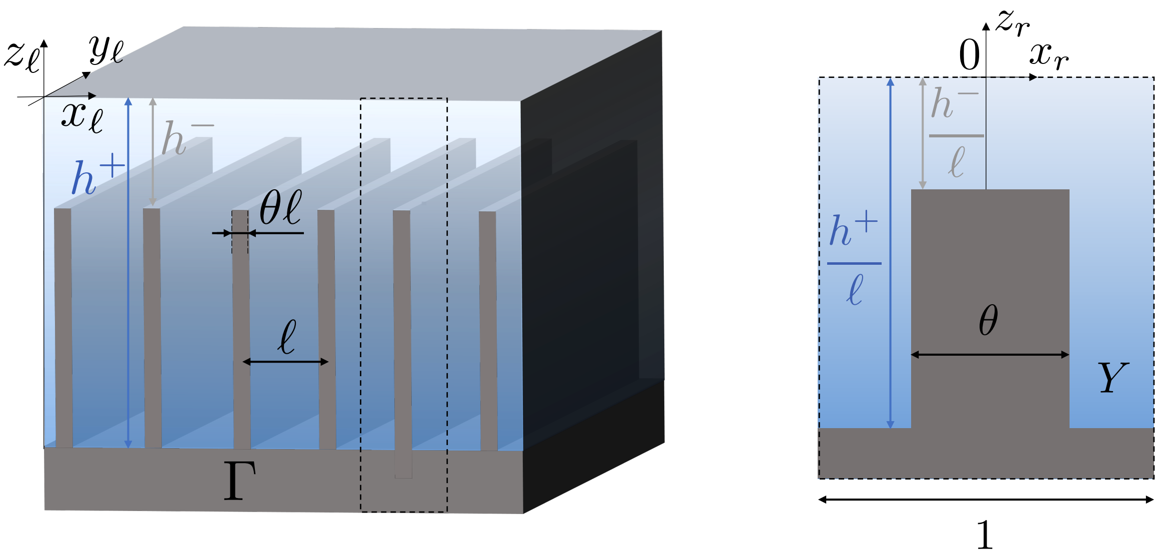

Fig. 3.6 Three dimensional structure of the metabathymetry in (x_ℓ, y_ℓ, z_ℓ) coordinate system and a zoom on the two-dimensional unit cell Y in (x_r, z_r) coordinates.

the modal method, whose principle is based on matching eigenfunction expansions. The corresponding example of the implementation of the modal method is described in detail in Appendix A.

3.4 Determination of real water depths

The method presented in previous sections allows to calculate the effective parameters for already existing geometry: h_x^* and h_y^*. This direct approach (Fig. 3.7) does not cause major problems when specifying the anisotropy produced by such a system, and it is straightforward to obtain the effective parameters. However, in our case, the values of h_x and h_y are already known (3.10) and are defined by the reference water depth h_0 and the bending angle of the cavity φ. With such assumptions, there are infinitely many geometries that realize the desired anisotropy. That is why we need to come up with an idea and additional assumptions to solve the inverse problem. Therefore, we use optimization routine for obtaining $\mathbf{h}^\pm = [h^+ \; h^-]^T$

$$\min_{\mathbf{h}^\pm \in \mathbb{R}^2} \left\| f(\ell, \theta, \mathbf{h}^\pm) - \begin{pmatrix} h_x^* \\ h_y^* \end{pmatrix} \right\|,$$
$$\text{subject to } h^+ - h^- \geq 0, \tag{3.16}$$

where $f(\ell, \theta, \mathbf{h}^{\pm})$ is a function whose output is a vector $[h_x\ h_y]^T$ and is simply the solution of the system using the modal method presented in Appendix A [48]. Here, the periodicity ℓ and the filling fraction θ are constant.

An example of the optimization routine for the cavity with the bending angle $\varphi = 30°$, being the solution of the problem (3.16) is presented in Fig. 3.8. Here, the periodicity ℓ and the filling fraction θ are constant and set to $\ell = 0.005$ m, $\theta = 0.2$. In order to solve this problem of optimization with constraints, we use the Nelder-Mead simplex search method [67] available in Matlab Optimization Toolbox. The starting point is chosen randomly from the region where $h^+ > h^-$. Ultimately, we end up with a value of the real water depths h^+ and h^- for a given value of the filling fraction θ and periodicity ℓ. The dependence of the real water depths on these two parameters (θ, ℓ) is shown in Fig. 3.9. We can see that the thicker the layers, the greater the water depth h^+ needs to be to achieve the desired anisotropy which suggests that the layers should be as thin as possible. The periodicity ℓ does not significantly change the values of the real water depths. However, we have to keep in mind that even a small decrease in h^- can be detrimental to wave generation. For that, we need a fluid layer thick enough to produce quality water waves in the cavity using the wavemaker.

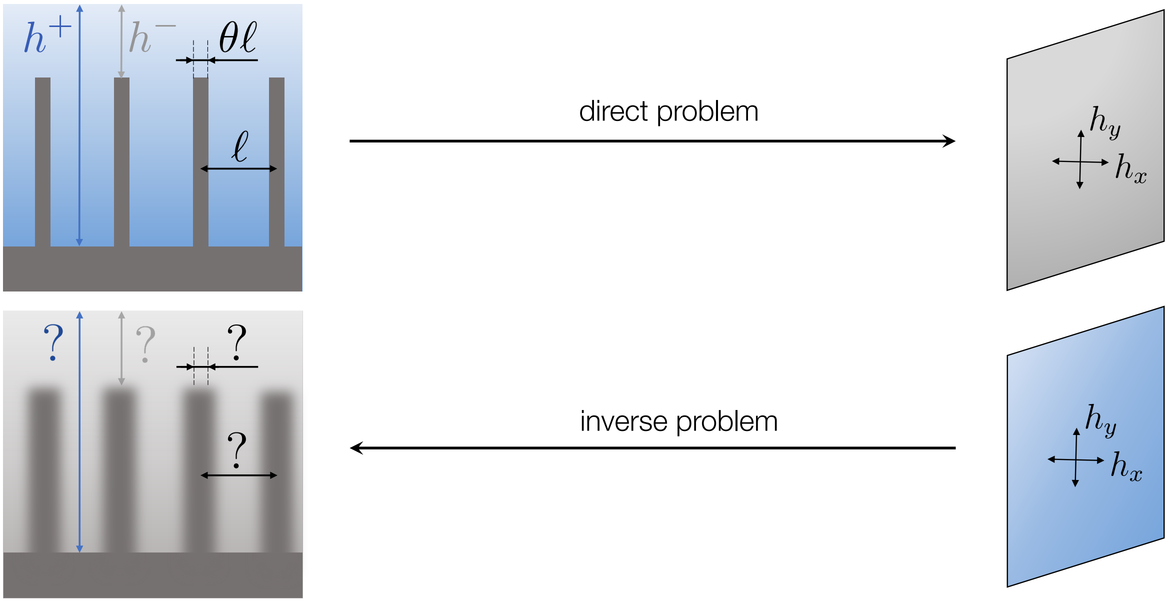

Fig. 3.7 The diagram of direct and inverse problem in calculating the anistropy coming from a layered structure.

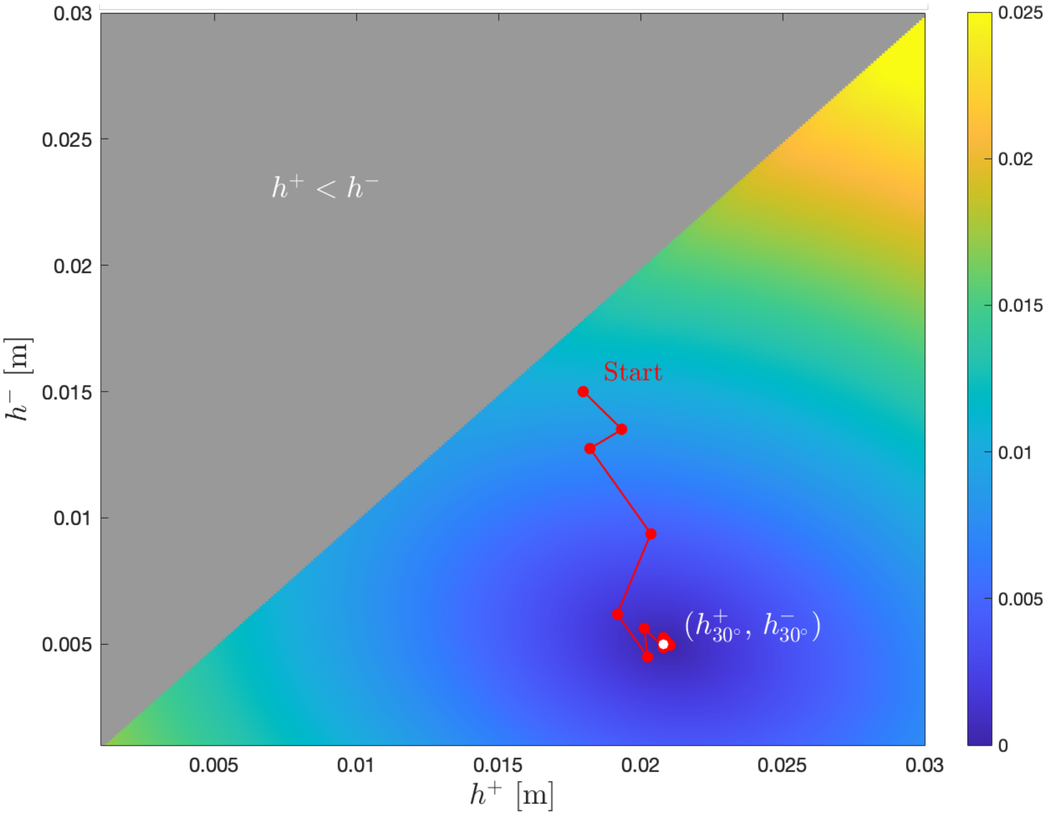

Fig. 3.8 An example of the minimization process (3.16) to find the real water depths h^+, h^- ($\ell = 0.005\,\mathrm{mm}$, $\theta = 0.2$).

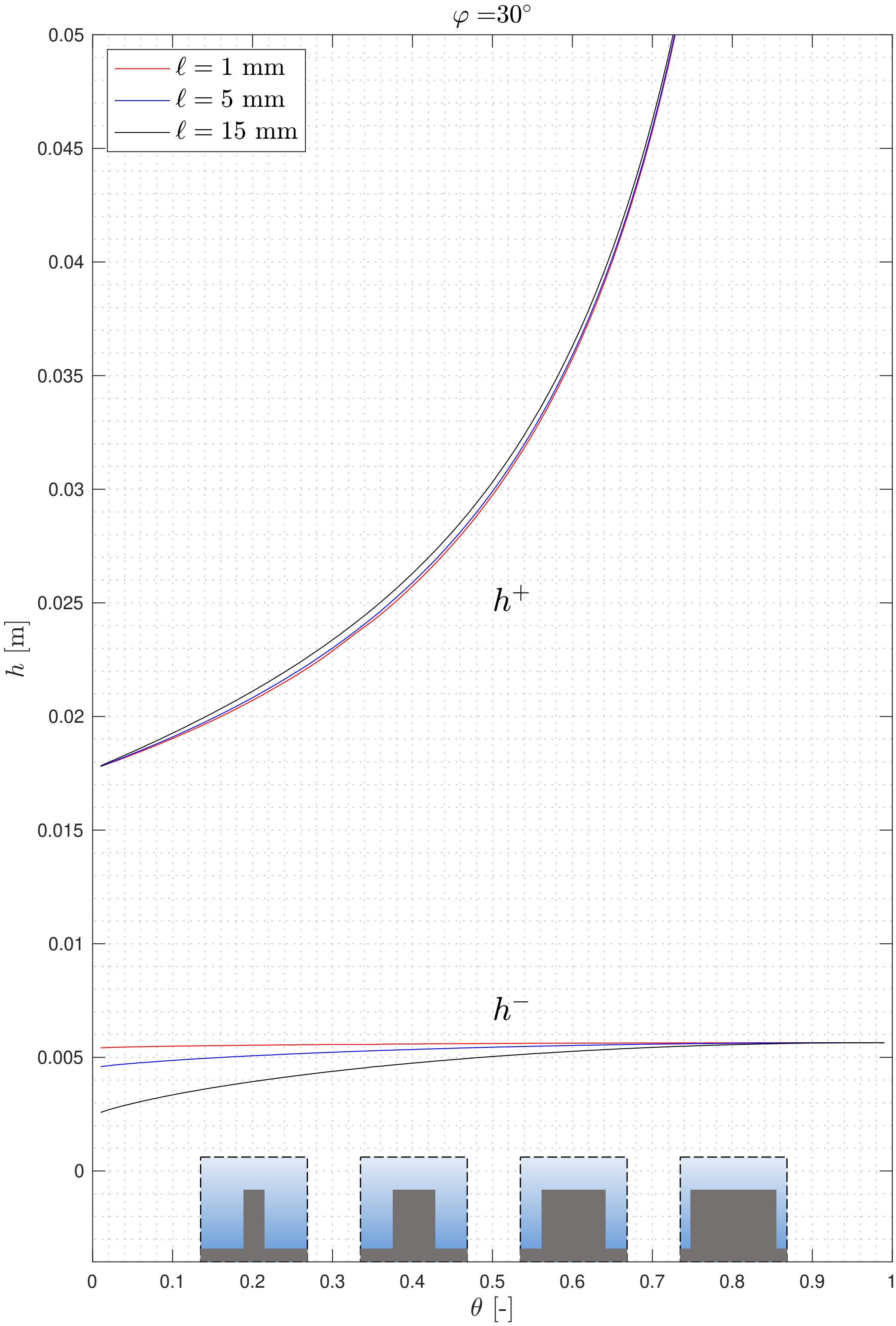

Fig. 3.9 Water depths h^+, h^- as a function of the filling fraction θ for different values of the periodicity ℓ ($\varphi = 30°$).

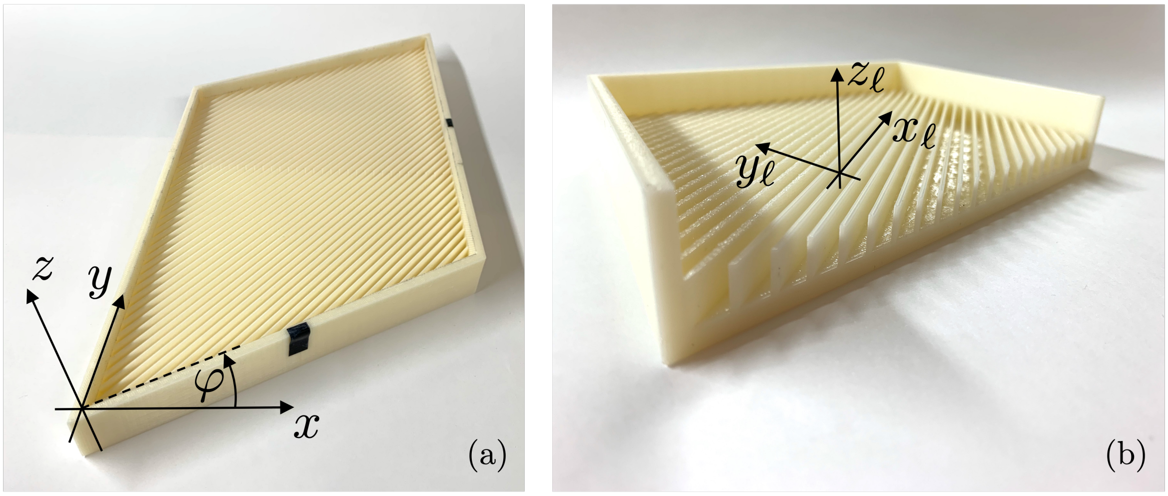

Fig. 3.10 (a) Metamaterial cavity used in experiments. The view from above with a coordinate system in the real space (x, y, z). (b) Section view with a local coordinate system used for metabathymetry design (x_ℓ, y_ℓ, z_ℓ).

3.5 Experimental setup

Three metamaterial cavities with bending angles $\varphi_1 = 15°$, $\varphi_2 = 30°$, and $\varphi_3 = 45°$ are designed and manufactured using rapid prototyping technique. Three reference cavities with flat bathymetry and of the same deviation angles φ_1, φ_2 and φ_3 are also built. The dimensions of the cavities are constant and set to $L_x = 200\,\mathrm{mm}$ and $L_y = 300\,\mathrm{mm}$. This fact allows to preserve the same volume throughout all cavities. The reference water depth is chosen as $h_0 = 10\,\mathrm{mm}$ as a trade-off between staying close to the shallow-water regime and undesirable attenuation caused by a bottom friction for small water depths. The parameters h_x, h_y, h^+, h^-, and α are calculated for each of the three systems based on the routine presented before, and they are summarised in Table 3.1. Considering wavemaker constraints ($h^- \geq 3\,\mathrm{mm}$) and rigidity limitations of the 3D printed structure ($\theta\ell \geq 1\,\mathrm{mm}$) we choose $\theta = 0.2$, and $\ell = 5\,\mathrm{mm}$.

The wave generator (point source) excites a system with a chirp signal whose frequency spectrum ranges from 0.3 Hz to 1.5 Hz. This range allows to recover the first five eigenmodes of the cavity. The partially immerged point source, creating a circular, linear wave, is placed in one of the corners of the cavity. The corner is chosen based on the shape of the eigenmodes so that it can be excited in the cavity. Occasionally the position of the source has to be changed since placing it in the node of the eigenmode would make it unfeasible to recover. The region where the wavemaker is placed is sufficiently cut out from the measurements so that the near-field effects are negligible.

To quantify the wavefield, we use the Fourier transform profilometry (FTP) technique [58] as well as confocal displacement sensors (2 lasers Keyence CL-P070). FTP is a technique that uses a fringe pattern projection on a measured surface. In our case, the water is painted with titanium dioxide (TiO_2) so that its surface becomes diffusive and ready for a fringe projection, whereas the change of physical properties of the painted water, including viscosity, is insignificant [61]. A high-resolution video projector EPSON EH-TW9200W is used to project the fringe pattern, and a high-speed camera Photron FASTCAM Mini WX100 records the deformation of the surface with an accuracy of more than 0.1 mm. Confocal displacement sensors allow us to measure the amplitude of the wave in the maxima of eigenmodes with much higher accuracy than FTP and with pure, transparent water confirming the results of the FTP technique. Using these methods, we obtain the space-time resolved measurements $\eta(x, y, t)$ that are later transformed into the frequency domain, resulting in the complex wavefield $\tilde{\eta}(x, y, \omega)$, to extract eigenfrequencies and eigenmodes.

Table 3.1 Cavities dimensions and design parameters.

φ [°]	15	30	45
α [°]	-41.18	-36.95	-31.72
h_x [mm]	7.66	5.66	3.82
h_y [mm]	13.06	17.68	26.18
h^+ [mm]	14.56	20.83	31.92
h^- [mm]	7.07	5.07	3.23

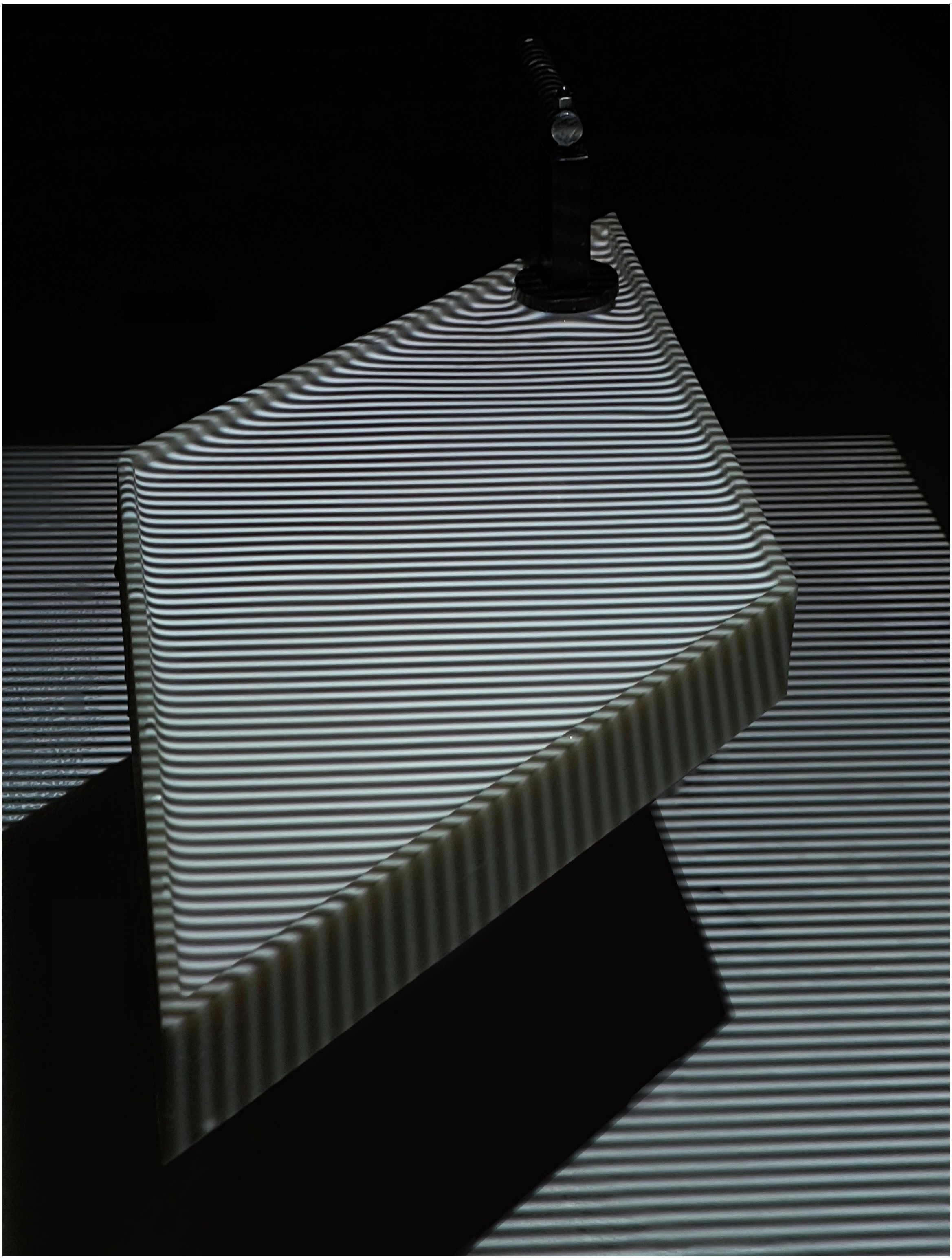

Fig. 3.11 Metamaterial cavity filled with water painted with titanium dioxide. The circular wavemaker in the corner produces the wave. The fringe pattern is projected onto the water surface and is necessary for FTP measurements.

Determination of eigenmodes and eigenvalues

Chirp signal

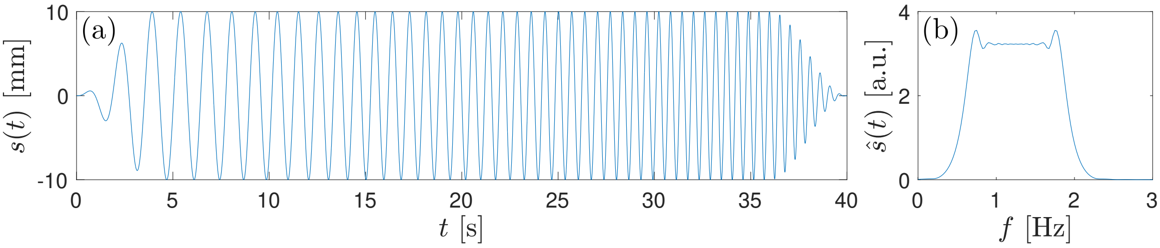

Fig. 3.12 (a) Example of the chirp signal $s(t)$ generated by the wavemaker. (b) Corresponding frequency spectrum of the signal.

Instead of measuring the system's response by exciting frequencies one by one, we use the chirp signal, whose wide frequency spectrum allows to recover all desired data with only one longer measurement. The signal sent to the motor is of the form

$$s(t) = A\cos\phi(t), \tag{3.17}$$

where $\dot{\phi} = \omega = 2\pi f(t)$. Assuming the linear change in frequency of the signal in time, i.e., $f(t) = f_0 + kt$, where $k = (f_1 - f_0)/(t_1 - t_0)$, we evaluate the phase $\phi(t)$ using

$$\phi = 2\pi \int_0^t f(\tau)\mathrm{d}\tau. \tag{3.18}$$

The example of the signal and its spectrum is given in Fig. 3.12 for the frequency range $f_0 = 0.5$ Hz, $f_1 = 2.5$ Hz and the time duration $t_1 - t_0 = 40$ s.

Mesh

Throughout the experiments in the rectangular cavity, it is noticeable that eigenfrequencies do not exactly match the predicted theoretical values (Fig. 3.13a) with an error up to 5% (Fig. 3.13b). However acceptable this error might be, we are able to reduce it by adding the mesh to the horizontal walls on every four sides of the cavity. The culprit of this behavior seems to be the meniscus [68] that deforms the wavefield by attaching the contact line to the wall. The meniscus changes the contact line, and the wave can be immobilized at the wall when the amplitude is small. By adding the mesh, we get rid of the undesirable wetting properties of the cavity's walls. This method allows a contact line to slide freely and now satisfy the homogenous

Neumann boundary condition assumed theoretically. With this approach, we are able to significantly reduce the error that now does not exceed 0.77% and is in the noise range.

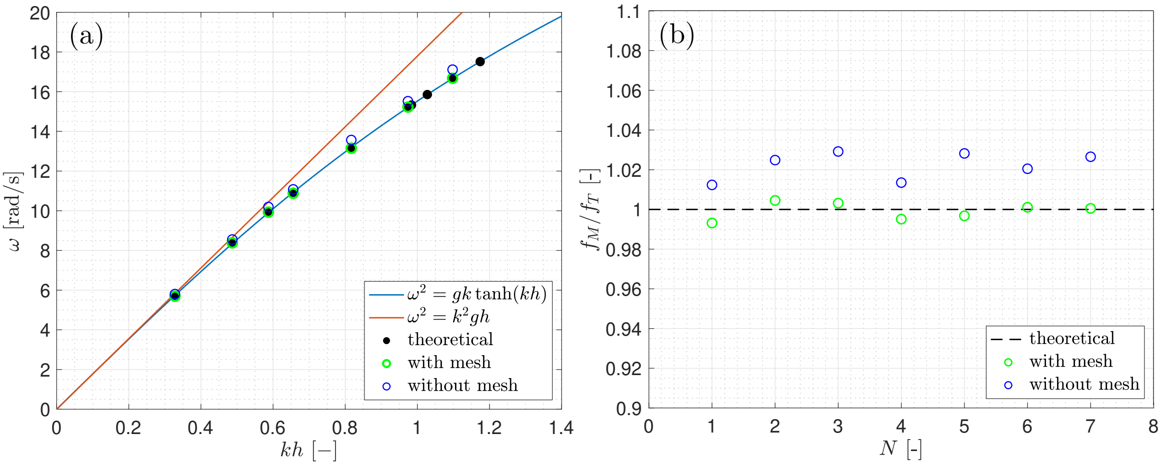

Fig. 3.13 (a) Measured eigenvalues with and without mesh over the dispersion relation. (b) Ratio of measured f_M and theoretical f_T eigenvalues for seven first eigenmodes N.

Determination of eigenmodes

The selection of eigenfrequencies from the experiments is made by finding the local maxima of $|\tilde{\eta}(x,y,\omega)|$ obtained by using Fourier transform of the original signal. Based on the reasoning presented in Section 1.4 we expect the eigenmodes to appear near the resonance frequencies of the cavity. That is why we assume that the peaks of the spectrum are equivalent to cavity eigenfrequencies. We measure the signal (s_A) using confocal displacement sensors in a few points of the cavity where the maximal amplitude is expected (Fig. 3.14a). We then extract the spectra (s_P) and average them ($\hat{s}_P$)

$$\hat{s}_P(f) = \frac{1}{N}\sum_{n=1}^{N}\left(\frac{1}{T}\int_0^T s_A^n(t)\mathrm{e}^{\mathrm{i}2\pi ft}\,\mathrm{d}t\right), \tag{3.19}$$

with $T = 1/f$, and N denotes a number of points. Then, the eigenmodes are chosen as the real part of $\tilde{\eta}(x,y,\omega)$ at the given eigenfrequencies using FTP technique. The example for a rectangular cavity with flat bathymetry is presented in Fig. 3.14.

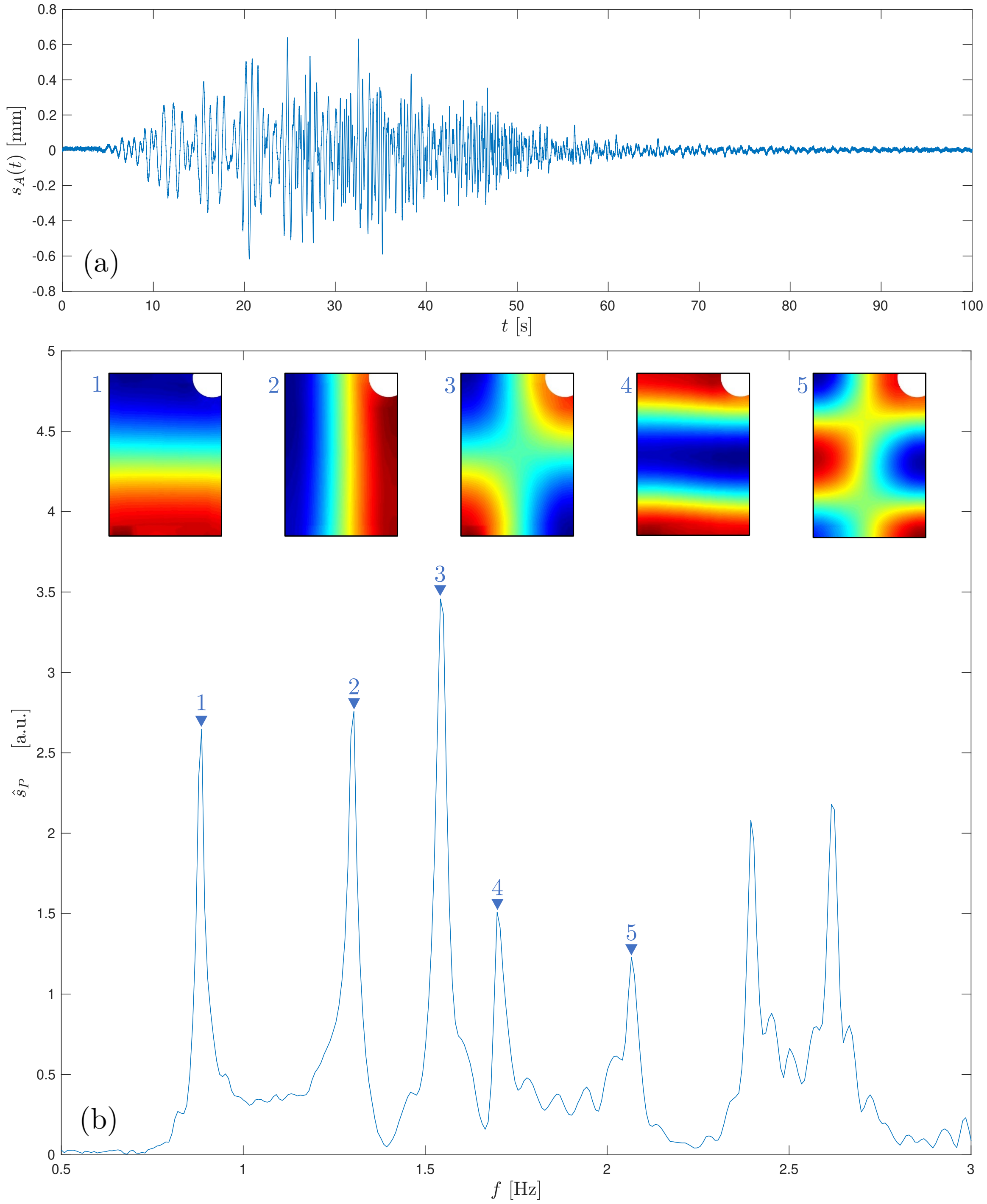

Fig. 3.14 (a) Measured signal in one point of the cavity. (b) Corresponding spectrum with identified eigenvalues and its measured eigenmodes using FTP method.

3.6 Experimental results

All of the five eigenmodes recovered in this experiment for the angles $\varphi = 15°$, $\varphi = 30°$, and $\varphi = 45°$ are reported in Fig. 3.15, 3.16, and 3.17 respectively. The higher modes were difficult to achieve for several reasons. First of all, as we increase the frequency, the eigenvalues become closer to each other, including degenerate cases, and are problematic if not impossible to distinguish experimentally. Moreover, when it comes to higher frequencies, dispersion and dissipation play a significant role in the water wave experiments, questioning the shallowness of the system and measurement techniques capacities, as the amplitude of the wave becomes extremely small. Please note that increasing the amplitude and the frequency of a water wave in our system would result in a nonlinear problem, which is not studied in this thesis.

The real part of the wavefield for the fifth eigenmode, i.e., the one whose frequency is the highest in the set of the measurements, is presented in Fig. 3.18 for rectangular reference cavity and the cavities with the bending angles φ of 0°, 15°, 30° and 45°. In the reference cavities without the metabathymetry the effect of the difference in geometry is clearly visible. The eigenmodes change their shape significantly with respect to the angle φ. The change in the position of nodes and maxima is easily noticeable. Introducing metabathymetry has an anticipated consequence. The eigenmode pattern remains the same throughout the measurements, even for the highest angle $\varphi = 45°$. It is worth mentioning that in this case, i.e., the mode with the highest frequency and the highest bending angle, the pattern remains the same, even though the shallow water approximation here is questionable ($h^+ = 31.92\,\mathrm{mm}$) and the friction of the metamaterial structure becomes more and more significant ($h^- = 3.23\,\mathrm{mm}$). This manifests a significant improvement and the benefit of using the homogenization of a fully three-dimensional linear water wave problem in comparison to previous works where 2D homogenization was used [32].

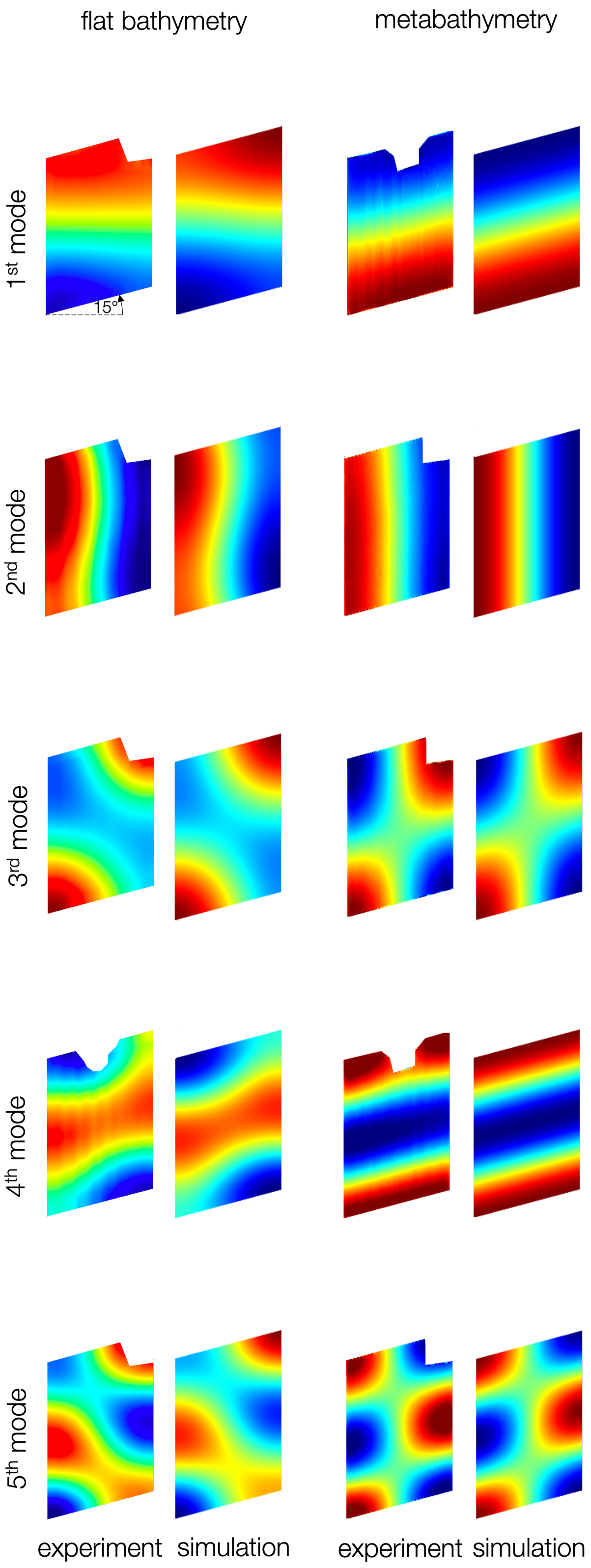

Fig. 3.15 The comparison of the real part of the measured wavefield $\tilde{\eta}(x, y, \omega)$ using FTP and the numerical prediction both for the cavities with the metabathymetry and the flat bottom for the first five eigenmodes and the lowest bending angle $\varphi = 15°$.

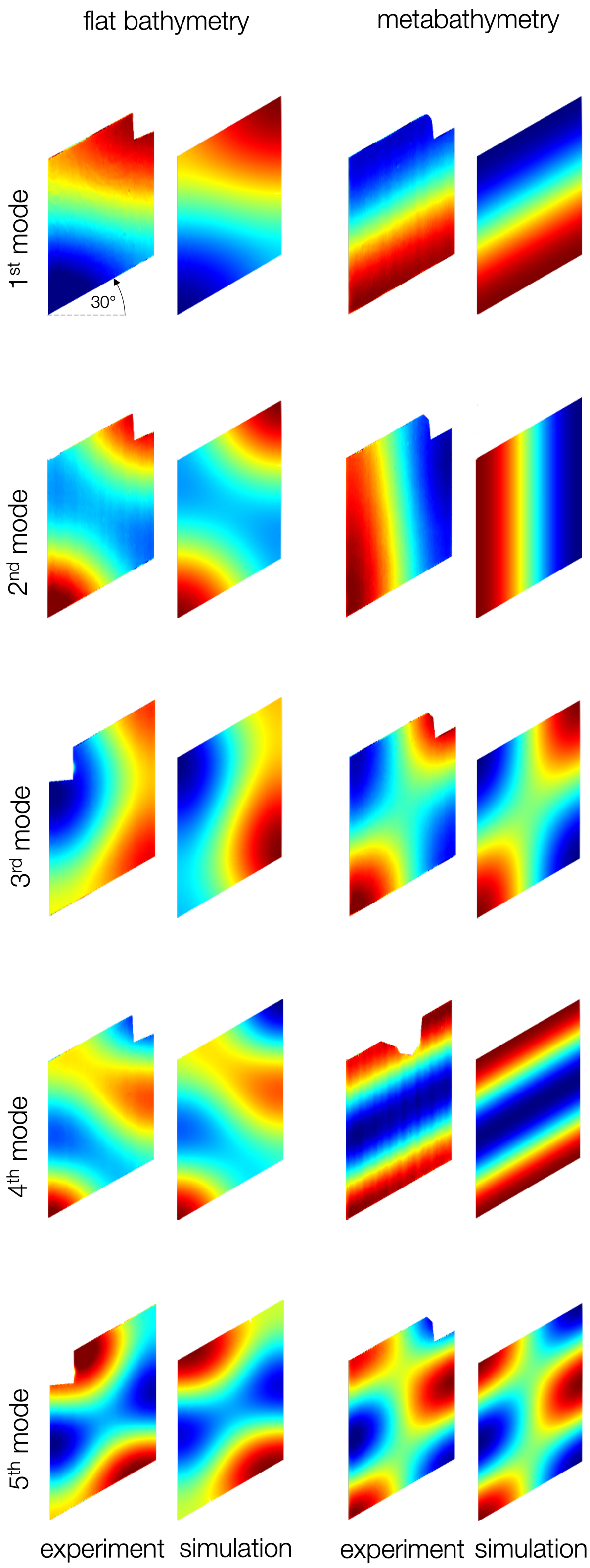

Fig. 3.16 The comparison of the real part of the measured wavefield $\tilde{\eta}(x, y, \omega)$ using FTP and the numerical prediction both for the cavities with the metabathymetry and the flat bottom for the first five eigenmodes and the bending angle $\varphi = 30°$.

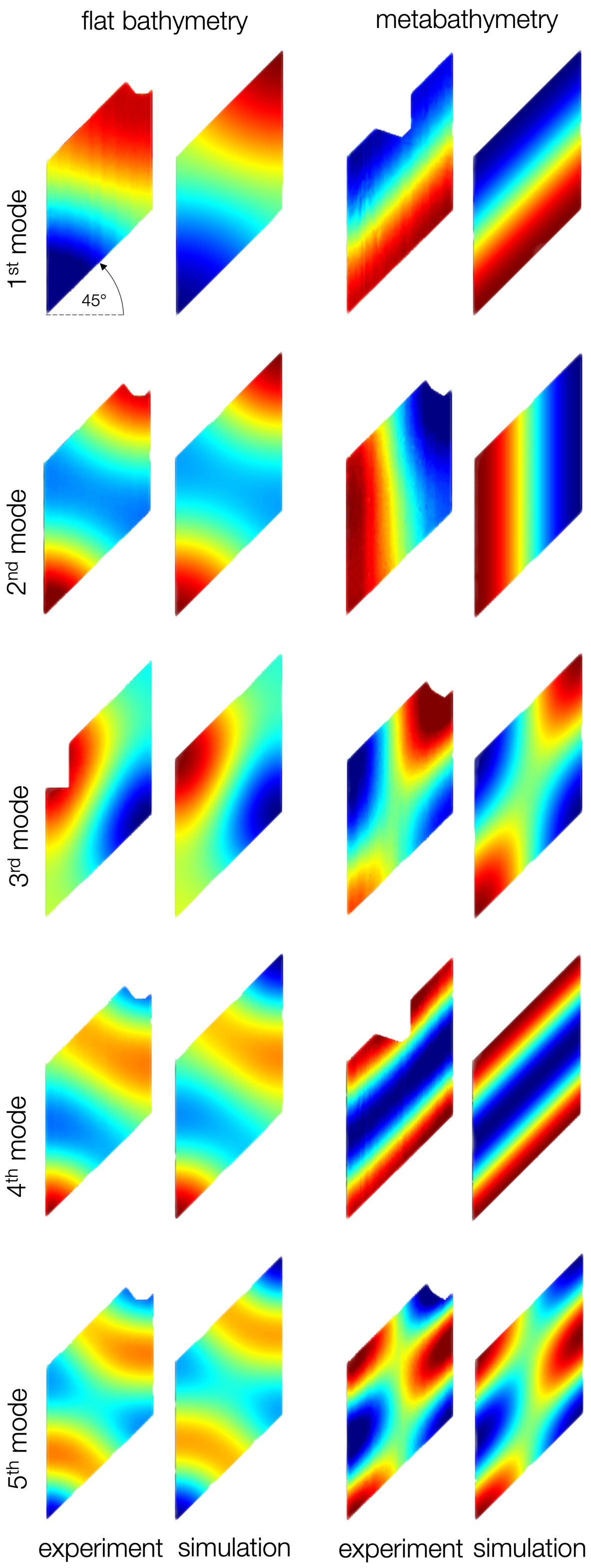

Fig. 3.17 The comparison of the real part of the measured wavefield $\tilde{\eta}(x, y, \omega)$ using FTP and the numerical prediction both for the cavities with the metabathymetry and the flat bottom for the first five eigenmodes and the greatest bending angle $\varphi = 45°$.

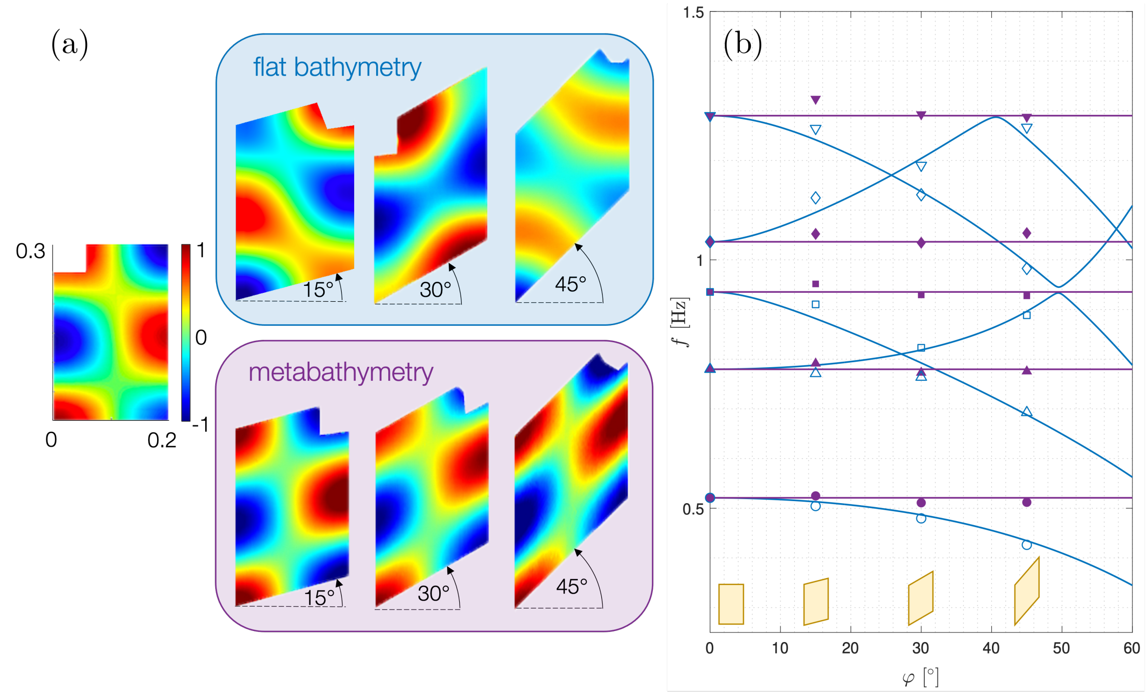

Fig. 3.18 (a) Experimental results for the real part of the fifth eigenmode $\tilde{\eta}(x, y, \omega)$ measured with the FTP technique for different bending angles φ. The wavefields for the flat bathymetry (top blue) and the results with the presence of the metabathymetry (bottom purple). (b) Experimental (symbols) and numerical (plain lines) values of eigenfrequencies as a function of the bending angle φ. Results are shown for the anisotropic bathymetry (purple) and the flat bathymetry (blue).

Comparing the experimental results with the numerical prediction, obtained by solving (3.9) using the Finite Element Method, we observe an excellent agreement of the eigenmodes. In order to quantitatively describe the difference between them, we introduce a pattern error defined as

$$\epsilon_P \equiv \frac{\iint_A |\eta_S(x, y, \omega) - \hat{\eta}(x, y, \omega)|^2 \, \mathrm{d}A}{\iint_A |\eta_S(x, y, \omega)|^2 \, \mathrm{d}A}, \tag{3.20}$$

where η_S is the normalized wavefield predicted numerically, $\hat{\eta}$ denotes the normalized wavefield measured in the experiments, and A is the area of the cavity. The normalization is accomplished by rescaling the wavefield amplitude so that it satisfies the following condition $\iint_A |\eta(x, y, \omega)|^2 \, \mathrm{d}A = 1$. The error increases both with the increasing angle φ and the frequency ω. However, in all of the cases, it does not exceed $\epsilon_P = 5.2\%$.

The summary of all the experimental values of the eigenfrequencies compared to the numerical predictions is shown in Fig. 3.18b. The horizontal axis represents the angle of the cavity deformation φ and the vertical axis - the frequency f. Consecutive lines correspond to the eigenvalues of the cavity with a bending angle φ. It can be seen that the use of the metabathymetry allows having a constant value of eigenfrequencies (purple symbols), hence meeting our goal and preserving the resonance properties of the deformed cavities as predicted with coordinate transformation theory.

The efficiency of the metabathymetry is quantified by the eigenfrequency error defined as

$$\epsilon_F = \frac{|f_S - f|}{|f_S|}, \tag{3.21}$$

where f_S is the predicted eigenfrequency, and f stands for the eigenfrequency measured using confocal displacement sensors. This error is always smaller than the pattern error ϵ_P, and its value varies from 1.4% to 3.1%.

3.7 Conclusions

The metabathymetry allows to retrieve the properties of a regular cavity in a shifted geometry. The example of one of the eigenmodes is reported in Fig. 3.18a for different angles φ. We are also able to maintain the same set of eigenfrequencies for the cavities with changed geometry (Fig. 3.18b).

The presented experiments show the robustness of the homogenization of the three-dimensional water wave problem and the coordinate transformation theory in designing metamaterials for water waves. The designed metabathymetry can be used for the control of water cavity resonance and the propagation of the wave inside of it. The efficiency of the anisotropic medium is shown using space-time resolved measurements of the full water wavefield. Very good agreement with numerical prediction is achieved.

Chapter 4

Submerged metamaterials and their anisotropic capacities

In Chapter 3 we evaluated the problem of designing the metabathymetry - metamaterial structure attached to the bottom of the fluid container. This approach works very well if the shallow water approximation is satisfied. However, for greater water depths, this assumption is violated. It is natural to think about a structure that would not necessitate being attached to the bottom of the tank and would be independent of how deep the container is. That is why we propose a possible solution to this problem that involves **submerged metamaterials**.

In this chapter, we study both theoretically and experimentally the array of plates put between two layers of liquid. Moreover, the homogenized model of such a structure is shown, and its robustness is verified experimentally.

4.1 Homogenization and dispersion relation

In the bulk, the single submerged plate satisfies the problem

$$\triangle\phi = 0, \tag{4.1}$$

where the boundary conditions are given by

$$\frac{\partial \phi}{\partial \mathbf{n}} = 0 \quad \text{on walls,} \tag{4.1a}$$

$$\frac{\partial \phi}{\partial z} = \frac{\omega^2}{g}\phi \quad \text{at } z = 0. \tag{4.1b}$$

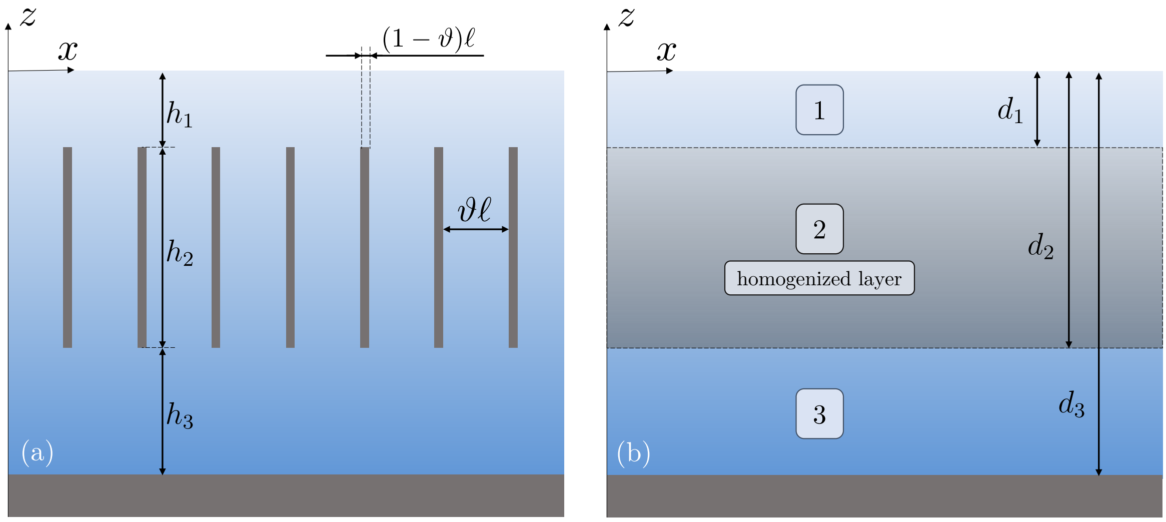

Fig. 4.1 (a) Scheme with dimensions of submerged metamaterials. (b) System with defined regions (layers) with the homogenized layer corresponding to the metamaterial structure.

After homogenization at the dominant order of the metamaterial structure (Fig. 4.1b), we can write corresponding equations in layers 1, 2, 3, where 2 is the homogenized layer. Defining a fraction of fluid between the metamaterial as ϑ, we have

$$\triangle\phi_1 = 0, \tag{4.2}$$

$$\nabla \cdot \left[\begin{pmatrix} 0 & 0 & 0 \\ 0 & \vartheta & 0 \\ 0 & 0 & \vartheta \end{pmatrix} \nabla\phi_2 \right] = 0, \tag{4.3}$$

$$\triangle\phi_3 = 0. \tag{4.4}$$

Due to the homogenized model, we shall ensure the continuity of the potential ϕ and its horizontal derivative. At each layers' boundary, we write

$$\text{at } z = 0 \qquad \frac{\partial\phi_1}{\partial z} = \frac{\omega^2}{g}\phi_1, \tag{4.5a}$$

$$\text{at } z = -d_1 \qquad \frac{\partial\phi_1}{\partial z} = \vartheta\frac{\partial\phi_2}{\partial z}, \qquad \phi_1 = \phi_2, \tag{4.5b}$$

$$\text{at } z = -d_2 \qquad \vartheta\frac{\partial\phi_2}{\partial z} = \frac{\partial\phi_3}{\partial z}, \qquad \phi_2 = \phi_3, \tag{4.5c}$$

$$\text{at } z = -d_3 \qquad \frac{\partial\phi_3}{\partial z} = 0. \tag{4.5d}$$

Owing to the separation of variables we can rewrite the problem (4.2) and its solutions as

$$\begin{aligned}
\frac{\partial^2\varphi_1}{\partial z^2} - k^2\varphi_1 = 0 \qquad &\Longrightarrow \qquad \varphi_1 = a_1\mathrm{e}^{kz} + b_1\mathrm{e}^{-kz},\\
\frac{\partial^2\varphi_2}{\partial z^2} - k_y^2\varphi_2 = 0 \qquad &\Longrightarrow \qquad \varphi_2 = a_2\mathrm{e}^{k_y z} + b_2\mathrm{e}^{-k_y z},\\
\frac{\partial^2\varphi_3}{\partial z^2} - k^2\varphi_3 = 0 \qquad &\Longrightarrow \qquad \varphi_3 = a_3\mathrm{e}^{kz} + b_3\mathrm{e}^{-kz},
\end{aligned} \tag{4.6}$$

where the wavenumber $k = \sqrt{k_x^2 + k_y^2}$. For the sake of the simplicity of calculations we rewrite boundary conditions (4.5) as follows

$$\text{at } z = 0 \qquad \frac{\partial_z\varphi_1}{\varphi_1} = \frac{\omega^2}{g}, \tag{4.7a}$$

$$\text{at } z = -d_1 \qquad \frac{\partial_z\varphi_1}{\varphi_1} = \vartheta\frac{\partial_z\varphi_2}{\varphi_2}, \tag{4.7b}$$

$$\text{at } z = -d_2 \qquad \frac{\partial_z\varphi_2}{\varphi_2} = \frac{1}{\vartheta}\frac{\partial_z\varphi_3}{\varphi_3}, \tag{4.7c}$$

$$\text{at } z = -d_3 \qquad \partial_z\varphi_3 = 0, \tag{4.7d}$$

where $\partial_z = \partial/\partial z$. Starting with the boundary condition at the bottom (4.7d), and substituting (4.6), we obtain

$$\frac{\partial_z\varphi_3}{\varphi_3} = k\tanh(k(z + d_3)). \tag{4.8}$$

On combining this result with the matching condition at $z = -d_2$, we deduce that

$$\left.\frac{\partial_z\varphi_2}{\varphi_2}\right|_{z=-d_2} = \frac{1}{\vartheta}k\tanh(kh_3). \tag{4.9}$$

Continuing this bottom-up approach, we can write similarily for (4.7c) and (4.7b), and ultimately using (4.7a), we obtain the dispersion relation for the homogenized submerged metamaterial structure

$$\boxed{\frac{\omega^2}{g} = k\frac{\tanh\left(kh_1\right) + \frac{\vartheta}{k}k_y\frac{\tanh(k_y h_2) + \frac{k}{\vartheta k_y}\tanh(kh_3)}{1 + \tanh(k_y h_2)\frac{k}{\vartheta k_y}\tanh(kh_3)}}{1 + \tanh\left(kh_1\right)\frac{\vartheta}{k}k_y\frac{\tanh(k_y h_2) + \frac{k}{\vartheta k_y}\tanh(kh_3)}{1 + \tanh(k_y h_2)\frac{k}{\vartheta k_y}\tanh(kh_3)}}.} \tag{4.10}$$

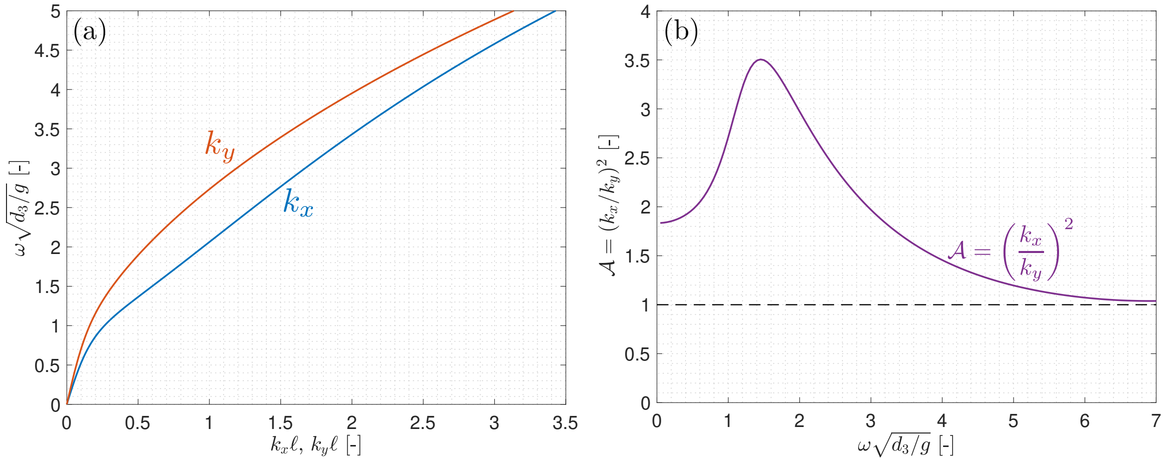

Fig. 4.2 The dispersion relation coming from the homogenized model (4.10) for submerged metamaterial (a) and the resulting anisotropy (b).

4.2 Bloch-Floquet analysis

In order to further investigate the dispersive characteristics of the submerged metamaterials, we perform the Bloch-Floquet analysis of the system with the support of the modal method presented in Appendix A. This analysis is carried out in a symmetric unit cell whose dimensions are $(-\ell/2, \ell/2) \times (-d_3, 0)$ (Fig. 4.3a). We benefit from the approach presented in [48] where a similar calculation was done for the plate array situated at the bottom (as in Chapter 3).

To evaluate the Bloch-Floquet spectrum, we solve the full 3D problem (4.1) in the unit cell. Since the geometry is independent of y, we can proceed with the reduction of the model to two dimensions. Thus, following Bloch's theorem, we obtain

$$\phi(x+\ell, y, z) = \mathrm{e}^{\mathrm{i}k_x\ell}\phi(x, y, z), \tag{4.11}$$

$$\frac{\partial\phi}{\partial x}(x+\ell, y, z) = \mathrm{e}^{\mathrm{i}k_x\ell}\frac{\partial\phi}{\partial x}(x, y, z), \tag{4.12}$$

where a dependence along y takes form $\mathrm{e}^{\mathrm{i}k_y\ell}$. We start with computing the scattering matrix S using the modal method, akin to the one shown in Appendix A. Due to the invariance of the geomtry along y axis we can write

$$\phi(x, y, z) = \mathrm{e}^{\mathrm{i}k_y\ell}\tilde{\phi}(x, z). \tag{4.13}$$

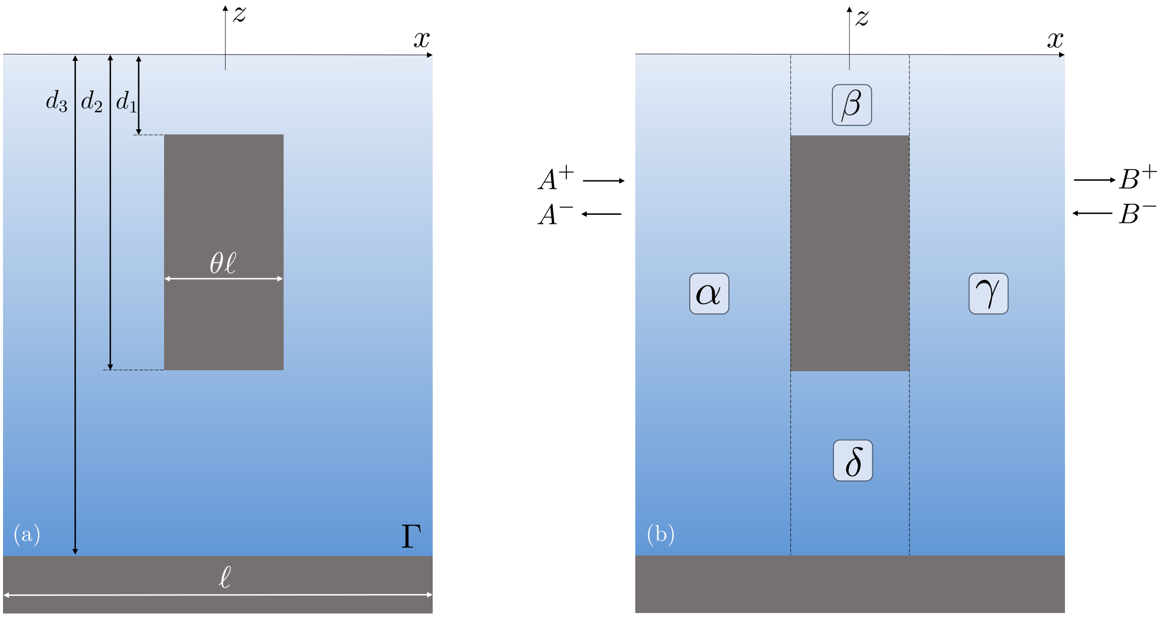

Fig. 4.3 (a) Scheme of the symmetric unit cell with dimensions of submerged metamaterial structure. (b) System with defined regions used to solve the full 3D problem using Bloch-Floquet analysis and the modal method. A^+ and A^- stand for the vectors of the outgoing and ingoing waves respectively at $x = -\ell/2$. B^+ and B^- denote the vectors of the outgoing and ingoing waves respectively at $x = \ell/2$.

Now, we shall consider the mode expansion outside the boundary, with ingoing (A^+, B^-) and outgoing (A^-, B^+) waves (Fig. 4.3b)

$$\tilde{\phi}(x,z) = \sum_n \left(A_n^+ \mathrm{e}^{\mathrm{i}k_n(x+\ell/2)} + A_n^- \mathrm{e}^{-\mathrm{i}k_n(x+\ell/2)}\right)\varphi_n(z) \qquad \text{for} \quad x \leq -\frac{\ell}{2}, \tag{4.14}$$

$$\tilde{\phi}(x,z) = \sum_n \left(B_n^+ \mathrm{e}^{\mathrm{i}k_n(x-\ell/2)} + B_n^- \mathrm{e}^{-\mathrm{i}k_n(x-\ell/2)}\right)\varphi_n(z) \qquad \text{for} \quad x \geq \frac{\ell}{2}. \tag{4.15}$$

The normalized transverse functions adapted to the boundary conditions (4.1a), (4.1b) are of the form

$$\varphi_n = N_n \cosh(K_n(z+d)), \tag{4.16}$$

where the normalization factor is

$$N_n = \left[\frac{d}{2}(\mathrm{sinhc}(2K_n d) + 1)\right]^{-\frac{1}{2}}. \tag{4.17}$$

The transverse functions satisfy the boundary conditions provided that K_n satisfies the dispersion relation for water waves

$$\frac{\omega^2}{g} = K_n \tanh(K_n d). \tag{4.18}$$

The relation between wavenumbers comes from ϕ satisfying the Laplace equation (4.1) and reads

$$k_n^2 = K_n^2 - k_y^2. \tag{4.19}$$

Similar procedure is applied to the regions $\alpha \in (-\ell/2, -\theta\ell/2) \times (-d_3, 0)$, $\beta \in (-\theta\ell/2, \theta\ell/2) \times (-d_1, 0)$, $\gamma \in (\theta\ell/2, \ell/2) \times (-d_3, 0)$, and $\delta \in (-\theta\ell/2, \theta\ell/2) \times (-d_3, -d_2)$, where expansions of ϕ^α, ϕ^β, ϕ^γ, and ϕ^δ are written using corresponding bases φ_n^α, φ_n^β, φ_n^γ, and φ_n^δ. Subsequently, the mode matching of ϕ and $\partial_x \phi$ is performed at the junctions $x = \pm\ell/2$ and $x = \pm\theta\ell/2$ as in (A.20). An example of the solution ϕ for the unit cell is presented in Fig. 4.4 for $d_1 = 0.005$, $d_2 = 0.055$, $d_3 = 0.1$, $\theta = 1/6$ and $\ell = 0.012$. This approach allows the relations of ingoing (A_n^+, B_n^-) and outgoing (A_n^-, B_n^+) waves to be found[1]. Hence, we obtain

$$\begin{pmatrix} A^- \\ B^+ \end{pmatrix} = S \begin{pmatrix} A^+ \\ B^- \end{pmatrix}, \quad \text{where} \quad S = \begin{pmatrix} R & T \\ T & R \end{pmatrix}, \tag{4.20}$$

with R and T being the reflection and transmition matrices. Let us rewrite the system (4.20) as

$$M_1 \begin{pmatrix} A^+ \\ A^- \end{pmatrix} = M_2 \begin{pmatrix} B^+ \\ B^- \end{pmatrix}, \tag{4.21}$$

where

$$M_1 = \begin{pmatrix} T & 0 \\ -R & I \end{pmatrix}, \quad M_2 \begin{pmatrix} I & -R \\ 0 & T \end{pmatrix}. \tag{4.22}$$

---

[1] For the sake of clarity of writing we identify the vector of the components of ingoing and outgoing waves as $A^\pm = A_n^\pm$ and $B^\pm = B_n^\pm$.

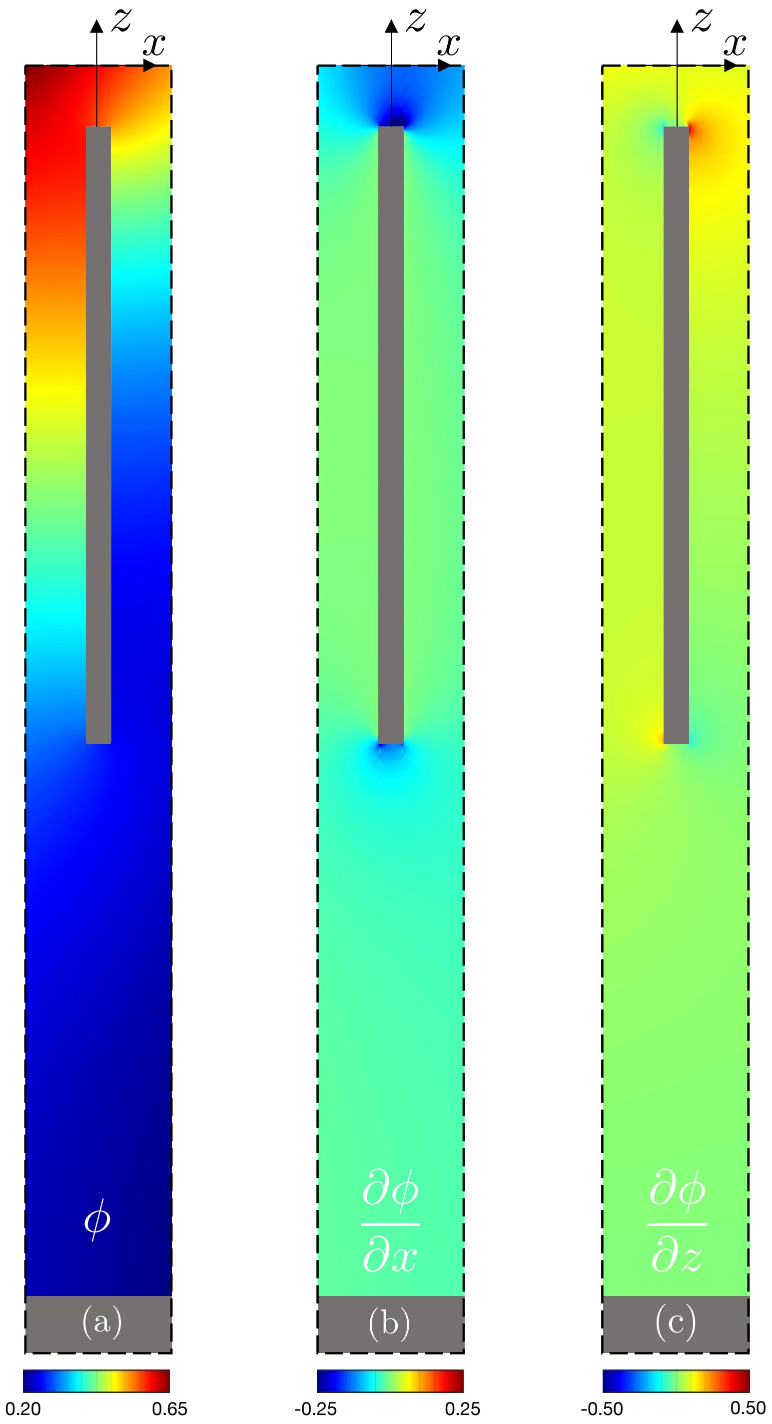

Fig. 4.4 (a) Solution $\phi(x, 0, z)$ in the unit cell and its horizontal (b) and vertical (c) derivatives.

Using the expansions of ϕ and following the Bloch-Floquet condition (4.11) we deduce that

$$\begin{pmatrix} B^+ \\ B^- \end{pmatrix} = \mu \begin{pmatrix} A^+ \\ A^- \end{pmatrix}, \tag{4.23}$$

with $\mu(\omega, k_y) = \mathrm{e}^{\mathrm{i}k_x\ell}$. On combining this result with (4.23), we conclude that

$$M_1 \begin{pmatrix} A^+ \\ A^- \end{pmatrix} = \mu M_2 \begin{pmatrix} A^+ \\ A^- \end{pmatrix} . \tag{4.24}$$

The above eigenvalue problem (4.24) eventually allows to obtain the Bloch-Floquet wavenumber $k_x\ell$ as a function of ω and $k_y\ell$ in the first Brillouin zone $(-\pi, \pi)$. The example of this approach is shown in Fig. 4.5 where the band structure is calculated and compared to the homogenized model from Chapter 4.1 for $d_1 = 0.005$, $d_2 = 0.055$, $d_3 = 0.1$, $\theta = 1/6$ and $\ell = 0.012$.

The homogenized model is able to reproduce the band structure with good accuracy for low frequencies. However, the higher the frequency, the more visible the differences are. In Fig. 4.5a, we can see that the homogenized model underestimates the value of the wavenumber k_x. Introducing the anisotropy value as

$$\mathcal{A} = \left(\frac{k_x}{k_y}\right)^2 , \tag{4.25}$$

it is noticeable that the anisotropy is the highest for one particular frequency (Fig. 4.5b). The homogenized model seems to overestimate the anisotropic capacities of the submerged structure. This behavior may be attributed to the limitations of the dominant order homogenization and possibly be explained by performing higher order homogenization. Interestingly enough, our model can predict the frequency for which maximum anisotropy occurs as reported in Fig. 4.5b.

In Fig. 4.5c, we show the dispersion relation of the homogenized model (4.10) and compare it to the Bloch-Floquet prediction (white dashed lines, Fig. 4.5d). First of all, it is clearly visible that the stratified submerged medium is able to produce a high degree of anisotropy for low frequencies. When frequency increases, the degree of the anisotropy decreases, which translates to the fact that the metamaterial structure is no longer at the subwavelength scale and it cannot support relatively small wavelengths. Consequently, it is inevitable to admit that the presented metamaterial structure can be designed and optimized for a narrowband frequency spectrum.

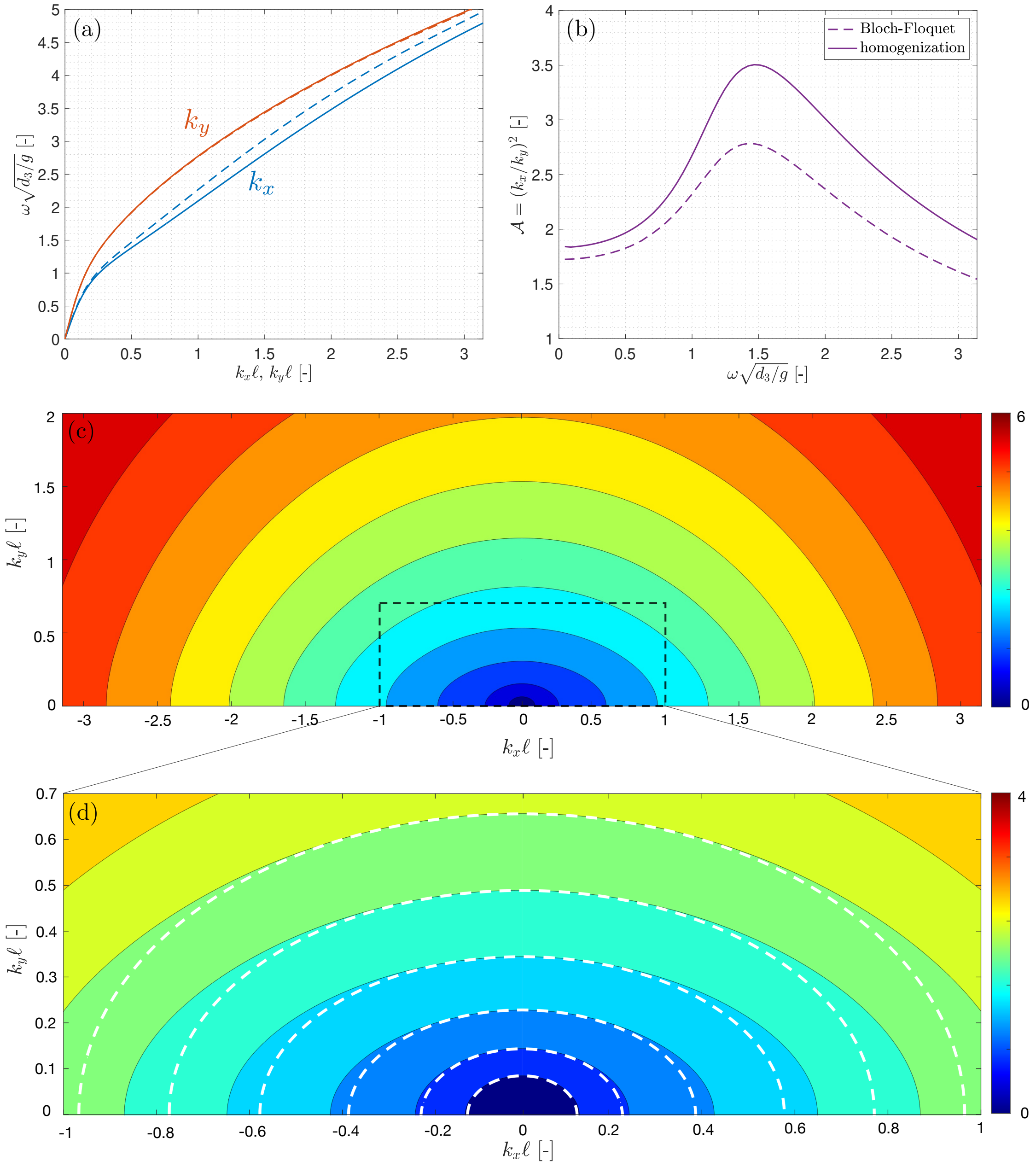

Fig. 4.5 (a) Nondimensional wavenumbers $k_x\ell$ (blue) and $k_y\ell$ (orange) over the nondimensional frequency $\omega\sqrt{d_3/g}$ obtained both from the homogenized model (plain lines) and the Bloch-Floquet analysis (dashed lines). (b) Comparison of the anisotropy of the submerged metamaterials as a function of the nondimensional frequency $\omega\sqrt{d_3/g}$ predicted by the homogenized model (dashed lines) and the Bloch-Floquet analysis (plain lines). (c) The dispersion relation given by the homogenized model as a function of nondimensional wavenumbers $k_x\ell$ and $k_y\ell$. (d) Zoom of the dispersion relation from the homogenized model (4.10) with the band structure obtained by Bloch-Floquet analysis (white dashed lines).

4.3 Experimental setup

The anisotropy of the submerged metamaterials is studied experimentally in order to verify both the numerical prediction given by Bloch-Floquet analysis and the homogenized model. With the aim of quantifying the wavefield, the Fourier transform profilometry technique is employed.

The experimental setup consists of a high-definition videoprojector and a camera with the temporal resolution set as 50 frames per second and whose spatial resolution is $2048 \times 2048\,\mathrm{px}^2$. Both are suspended on an aluminium profile at the height of $L = 1000\,\mathrm{mm}$ over a water tank with dimensions $600 \times 1760\,\mathrm{mm}^2$. The distance between the lenses of the camera and the videoprojector is equal to $D = 400\,\mathrm{mm}$.

The submerged metamaterial structure (Fig. 4.6) is designed to be of total width and length of $L_x = L_y = 590\,\mathrm{mm}$ to fit the water tank both parallelly and perpendicularly. The structure is manufactured using 48 laser-cut plexiglass plates of height $h_2 = 50\,\mathrm{mm}$ and thickness $\theta\ell = 2\,\mathrm{mm}$, where the periodicity $\ell = 12\,\mathrm{mm}$ and the filling fraction $\theta = 1/6$. Further thinning of the plates would make them too flexible and therefore not rigid enough to withstand forces generated by the water waves. The periodicity $\ell = 12\,\mathrm{mm}$ is chosen to be sufficiently smaller than the typical wavelength comparable to the size of the tank. Meeting the experimental constraints such as the depth of the tank (120 mm), or the dispersion relation of water waves, leaves us with placing the plates at the height of $h_3 = 45\,\mathrm{mm}$. Such a structure is verified numerically and should be able to produce anisotropy of the order $\mathcal{A} \approx 5$.

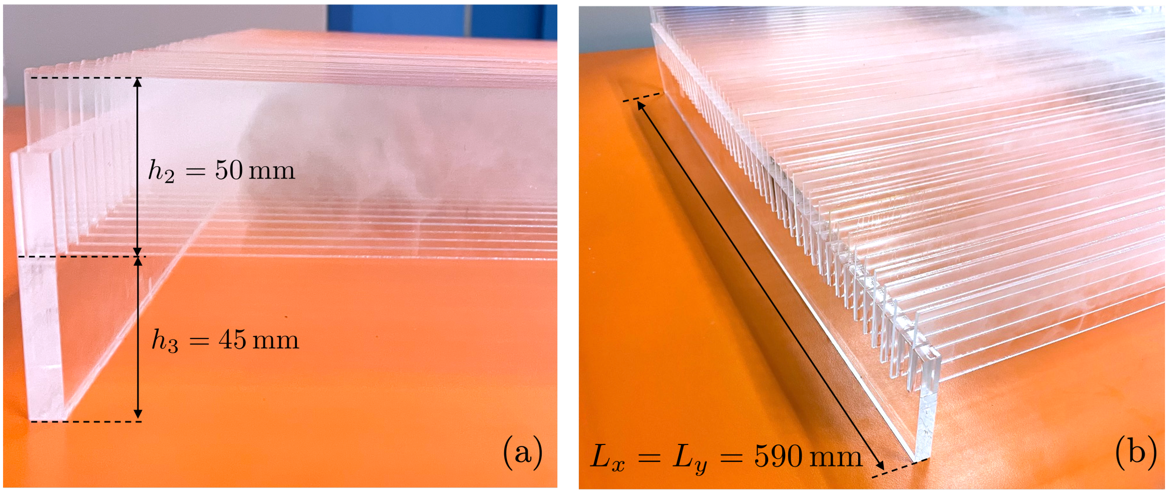

Fig. 4.6 (a) Side view of the metamaterial structure manufactured using laser-cut plexiglass and its dimensions. (b) View from the above of the metamaterial structure with its total width and length.

The region of interest is of the size $512\times335\,\mathrm{mm}^2$ which corresponds to the resolution of the image $2048 \times 1340\,\mathrm{px}^2$ with a pixel size of 0.25 mm/px. The obtained image represents the area of the tank entirely covered with the metamaterial structure.

The wavemaker with a circular end of diameter $\phi_{\mathrm{source}} = 40\,\mathrm{mm}$ is placed at the center of the region of interest (Fig. 4.7). The tip of the wavemaker is connected to the motor with an aluminum rod to diminish the shadow and, therefore, maximize the measurement area. The linear motor realizes vertical sinusoidal motion with a frequency range of $f_{\mathrm{source}} \in [2, 7]\,\mathrm{Hz}$ and typical amplitude of $A_{\mathrm{source}} \in [1, 3]\,\mathrm{mm}$ creating a source of the circular wave for our system. The wavefield is measured frequency by frequency with a step of $\Delta f = 0.5\,\mathrm{Hz}$.

4.4 Experimental results

The Fourier transform profilometry technique provides the space-time resolved measurements of the free surface elevation $\eta(x, y, t)$ and can detect waves whose amplitude is as small as 0.1 mm. The wavefield measured at each frequency is later transformed in the frequency domain using Fourier transform as follows

$$\hat{\eta}(x, y, f) = \frac{1}{T}\int_0^T \eta(x, y, t)\mathrm{e}^{-\mathrm{i}2\pi ft}\,\mathrm{d}t, \tag{4.26}$$

where $T = 1/f$. The temporal signal starts usually 2 s before the emission of the wave by the source and ends when the wave reaches the closest boundary of the water tank. This is to avoid the reflection in the measurement region that could make the data treatment more cumbersome.

The complex fields of $\hat{\eta}(x, y, f)$ at the fundamental frequency are computed and presented in Fig. 4.8 and Fig. 4.9. The fundamental frequency is chosen as one that presents a maximum in the spectrum and corresponds to the frequency of the source with a negligible error smaller than 0.3%. The contribution of the higher harmonics is also negligible and usually of the order of 2-4% when it comes to the first harmonic ($2f_0$). The maximum amplitude of the wave near the source depends on the water depth h_1 that varies throughout the experiments but usually is in the range of $0.5 - 5\,\mathrm{mm}$.

In order to examine the anisotropic behavior of the submerged metamaterial structure, the measurements are performed for three different water depths h_1: 2 mm, 5 mm, and 10 mm. The water depths h_2 and h_3 are constant and equal to 50 mm and 45 mm, respectively.

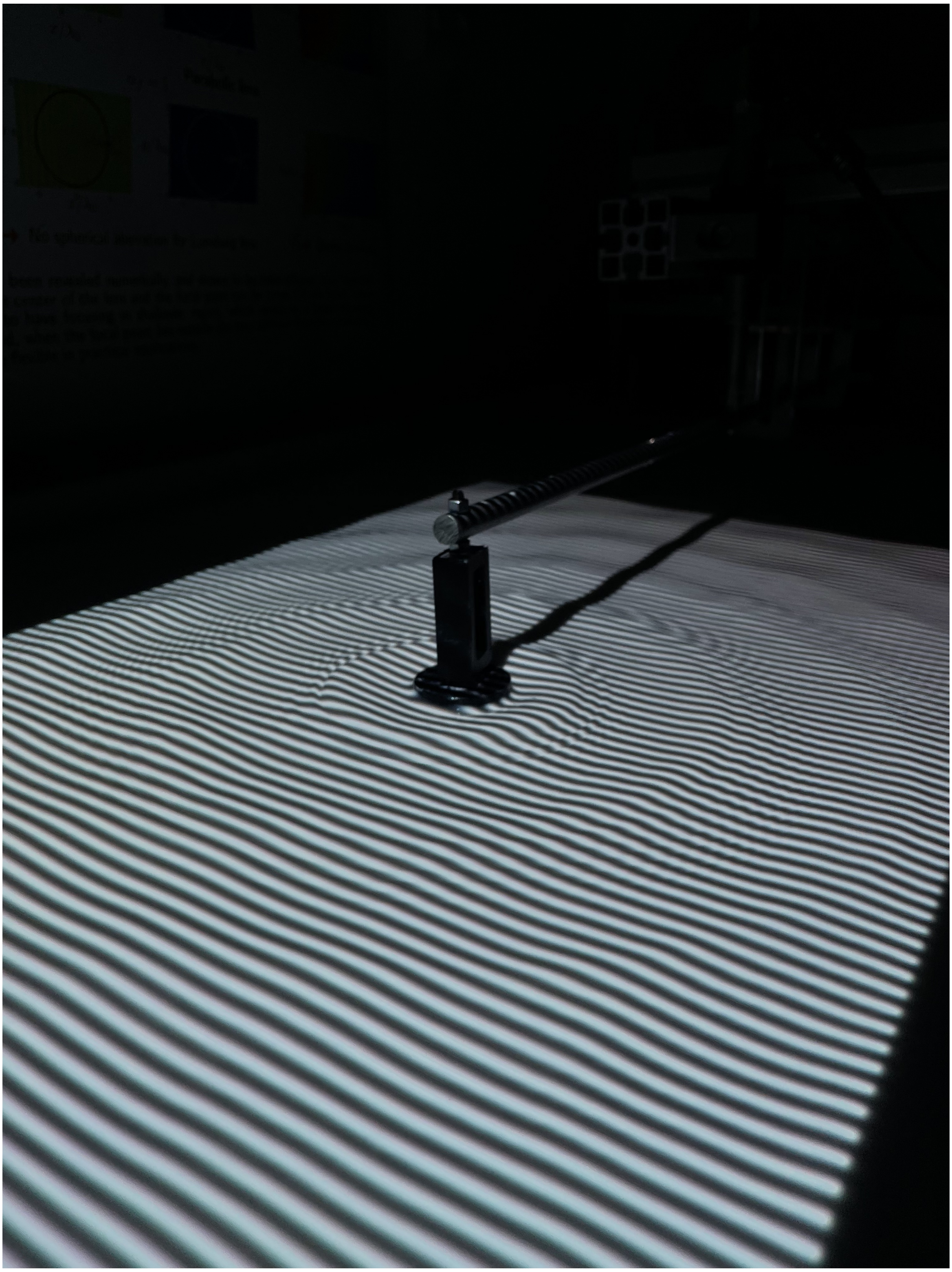

Fig. 4.7 Experimental setup. The circular wavemaker is placed in the middle of the region of interest creating the wave. The fringe pattern is projected on the surface to allow Fourier transform profilometry measurements.

The real parts of the complex fields $\hat{\eta}(x, y, f)$ for three different water depths h_1 are reported in Fig. 4.8 for the frequencies f: 2 Hz, 3 Hz, and 4 Hz and in Fig. 4.9 for the frequencies f: 5 Hz, 6 Hz, and 7 Hz. It can be clearly seen that the submerged metamaterial medium is able to produce the anticipated anisotropy. This effect is evident for low frequencies and small water depth h_1.

In order to examine the anisotropic behavior of the structure more quantitatively, we measure the wavelength in x and y direction. We benefit from previously obtained complex wavefields to obtain λ_x measured at $\hat{\eta}(x, y = 0)$ and λ_y measured at $\hat{\eta}(x = 0, y)$. The wavelength is calculated in two ways. First, we measure the distance between two peaks of the waves as presented in the (Fig. 4.10). The second approach consists of the fitting of the wave with the Hankel function of the first kind defined as

$$H_0^{(1)}(k_x x) = J_0(k_x x) + \mathrm{i} Y_0(k_x x), \tag{4.27}$$

where J_0 stands for the Bessel function of the first kind, and Y_0 denotes the Bessel function of the second kind. In general, they are defined by

$$J_\nu(k_x x) = \left(\frac{k_x x}{2}\right)^\nu \sum_n \frac{(-(k_x x)^2/4)^n}{n!\Gamma(\nu + n + 1)}, \quad Y_\nu(k_x x) = \lim_{\nu \to \mu} \frac{J_\mu(k_x x)\cos(\mu\pi) - J_{-\mu}(k_x x)}{\sin(\mu\pi)}, \tag{4.28}$$

where Γ is the Gamma function and the wavenumber $k_x = 2\pi/\lambda_x$. A similar approach is adopted for the wavelength λ_y. In our case, the Bessel functions are of order 0. Using these two methods to obtain the wavelengths, we can define the errorbar in Fig. 4.11, where we present the ensemble of the experimental data. When it comes to calculating the anisotropy

$$\mathcal{A} = \left(\frac{k_x}{k_y}\right)^2 = \left(\frac{\lambda_y}{\lambda_x}\right)^2, \tag{4.29}$$

we must evaluate the value of the error mentioned above according to the error propagation theory. The error of the value of the anisotropy $\epsilon_\mathcal{A}$ can be calculated as

$$\frac{\epsilon_\mathcal{A}}{\mathcal{A}} = 2\sqrt{\left(\frac{\epsilon_{\lambda_x}}{\lambda_x}\right)^2 + \left(\frac{\epsilon_{\lambda_y}}{\lambda_y}\right)^2}. \tag{4.30}$$

This leaves us with quite considerable uncertainty concerning the value of anisotropy. However, its mean value corresponds very well to the value predicted by the Bloch-Floquet analysis.

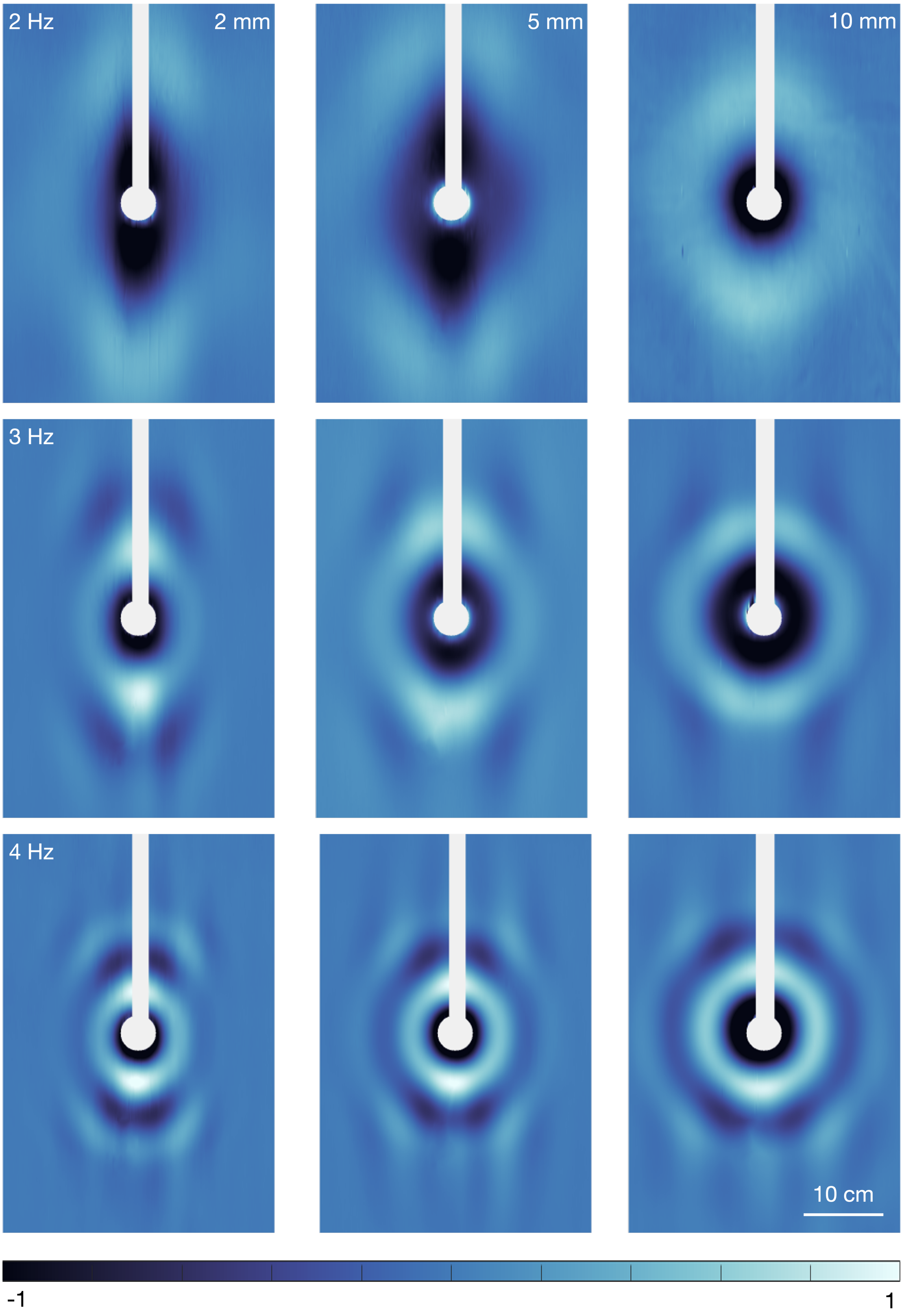

Fig. 4.8 Real part of $\hat{\eta}(x, y, f)$ for different water depths h_1 (2 mm, 5 mm, 10 mm - from left to right) and varying frequency f (2 Hz, 3 Hz, 4 Hz - from top to bottom).

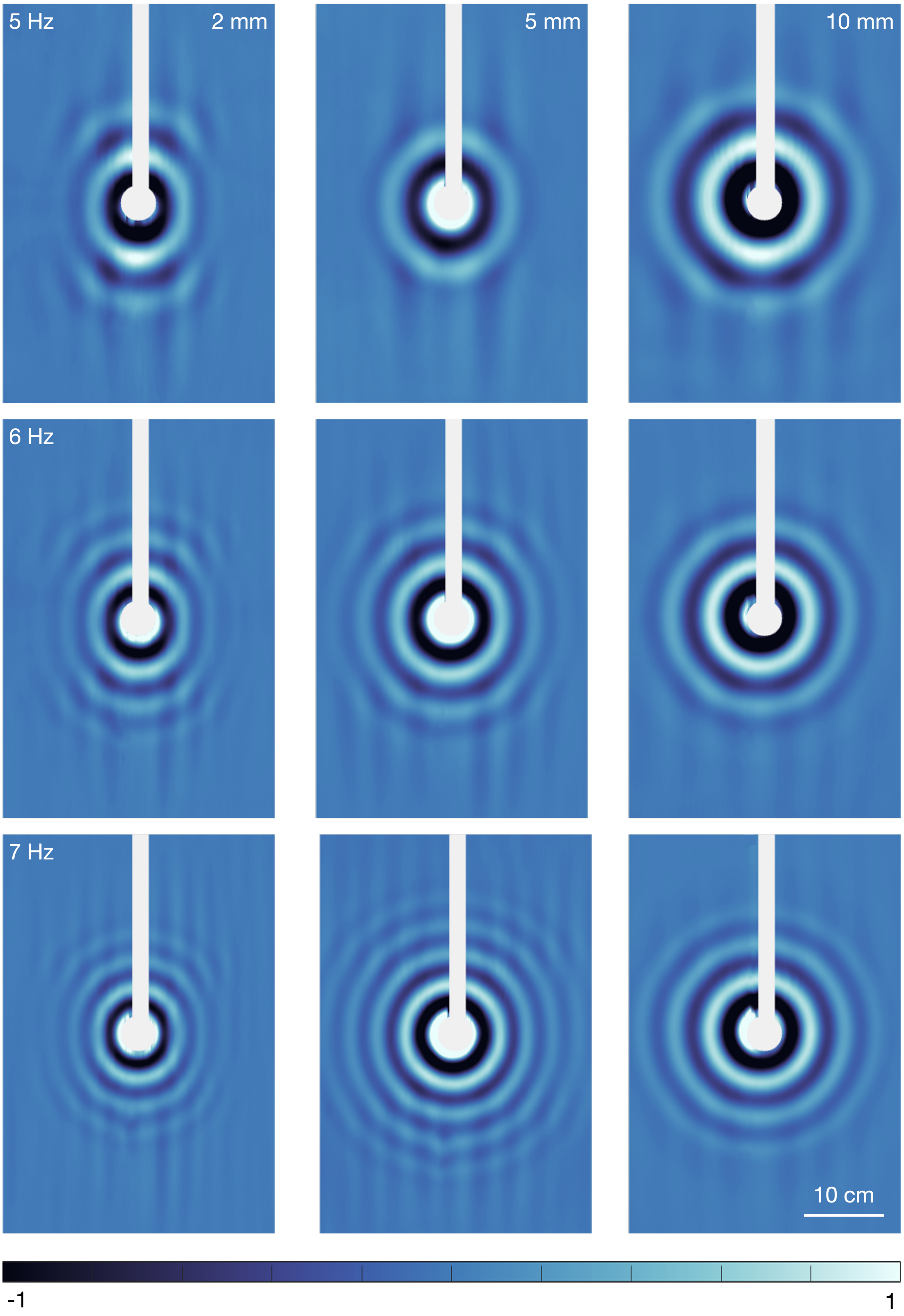

Fig. 4.9 Real part of $\hat{\eta}(x, y, f)$ for different water depths h_1 (2 mm, 5 mm, 10 mm - from left to right) and varying frequency f (5 Hz, 6 Hz, 7 Hz - from top to bottom).

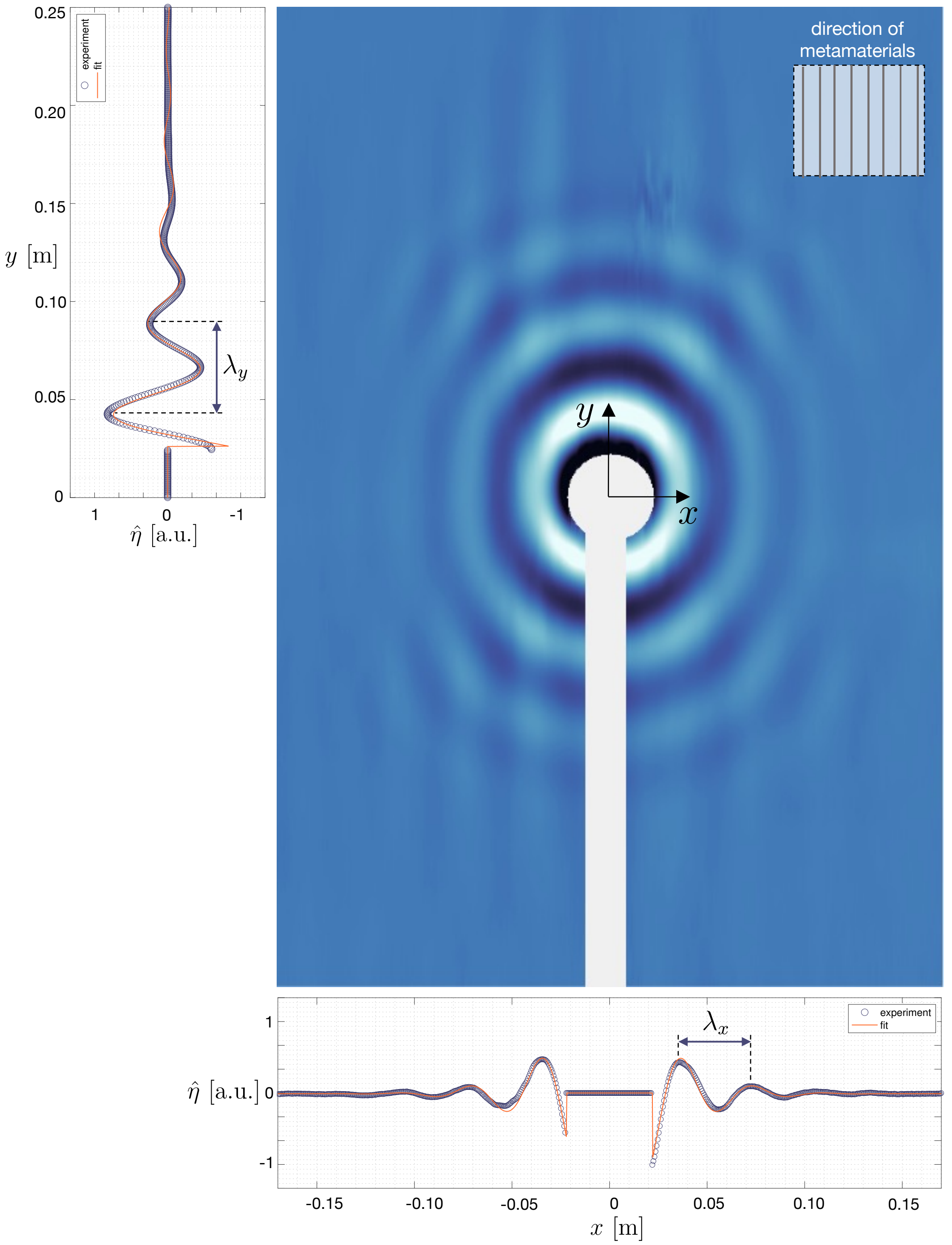

Fig. 4.10 The colormap shows the real part of $\hat{\eta}(x, y, f)$ from the experimental measurement for $f = 6$ Hz and $h_1 = 2$ mm. The plots show the horizontal and vertical profiles for $x = 0$ mm and $y = 0$ mm respectively with the best fits of Hankel function $H^0(k_x x)$ and $H^0(k_y y)$ (orange curves).

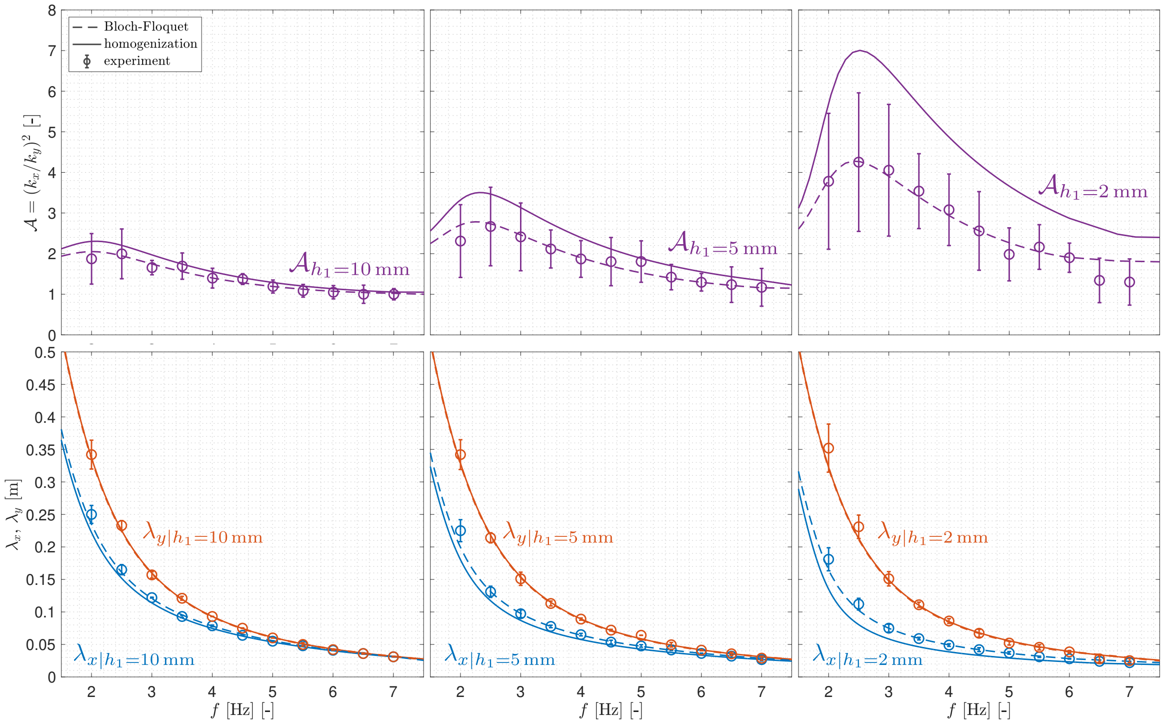

Fig. 4.11 Experimental values (symbols) for the wavelengths λ_x (orange), λ_y (blue) and resulting anisotropy $\mathcal{A}$ (purple) compared to the prediction of homogenized model (plain curves) and Bloch-Floquet analysis (dashed lines). The data is presented for different water depths h_1: 10 mm (left), 5 mm (center), 2 mm (right).

All the experimental values of λ_x, λ_y, and the resulting anisotropy are reported in Fig. 4.11. Under the scrutiny of the experimental data, it is evident that the anisotropy increases with decreasing water depth h_1. As expected, experiments confirm the decrease of the anisotropy for higher frequencies. The highest value of the anisotropy is obtained for the lowest water depth $h_1 = 2\,\mathrm{mm}$ and reaches $\mathcal{A} = 4$. The anisotropic behavior is still visible even for higher frequencies. For the water depth of $h_1 = 10\,\mathrm{mm}$, the anisotropic capacity of the metamaterial is still noticeable for low frequencies to disappear almost completely for higher ones.

The Bloch-Floquet analysis is able to predict very well the anisotropic characteristics of the submerged metamaterials. Even though the homogenized model slightly underestimates the value of the wavelength λ_x (perpendicular to the direction of the metamaterial structure) it represents a useful alternative to predict maximal anisotropy efficiently.

4.5 Conclusions

The homogenized model for submerged water-wave metamaterials presented in this chapter offers a valuable tool when it comes to metamaterial design. It can accurately foresee the anisotropic capacities of such a structure, particularly the frequency band for which maximal anisotropy is manifested. This result is verified using Bloch-Floquet analysis that can further and more precisely determine the dispersion relation for submerged metamaterials. The experimental data confirm with a very good agreement the theoretical analysis.

In order to further improve the homogenized model, higher order homogenization can be done to explain the discrepancies between the model and the actual behavior of the system. Since it has been seen that we can expect high anisotropy for thin fluid layers ($h_1 \to 0$), it might also be advantageous to consider replacing the layer with an effective boundary condition [69] that could possibly compensate for the differences between the presented homogenized model and the actual metamaterial structure.

Chapter 5

Su-Schrieffer-Heeger model for water waves in a periodic channel

Conventionally, metamaterials are considered as artificially structured media, with a unit cell whose dimensions are much smaller than the wavelength. This subwavelength condition, much needed in the context of the homogenization process, plays a crucial role in obtaining the approximation of the effective medium. However, it is also possible to design a structure where the peculiar behavior of the wave can be observed even though its length is comparable or even greater than the size of the unit cell [40, 41]. In this chapter, we focus on such structure for water waves developed owing to the theory of topological insulators.

The study of topological insulators was set in motion after the discovery of the quantum Hall effect [70, 71]. Since then, it has been investigated and realized for the wave systems in various contexts, *inter alia*, in acoustics [72–75], photonics [76–79], phononics [80–82], or mechanics [83–86]. A fundamental feature of topological metamaterials is the presence of edge modes, i.e., topologically protected modes localized on the boundaries.

Undoubtedly, one of the simplest and most famous representations of the topological states is given by the Su-Schrieffer-Heeger model (SSH) [87, 42], whose properties generated a lot of interest in acoustic [88–90] or water wave system [91]. However, to benefit from the SSH model, these approaches usually use coupled resonator systems or band structure analysis thanks to the Zak phase.

Our study uses a different, more direct approach to describe a water wave system using the SSH model. A periodic water wave channel with alternating cells of two different widths and equal lengths is studied, allowing to map the 1D SSH model onto our system straightforwardly.

5.1 Model reduction. From 2D Helmholtz equation to SSH model

The infinite water wave channel with periodically varying width w_1, w_2 and the length of a cell d is considered as shown in Fig. 5.1a. The free surface elevation of the wave $\eta(x, y)$ with time harmonic dependence chosen as $\mathrm{e}^{-\mathrm{i}\omega t}$ satisfy the two-dimensional Helmholtz equation with the homogenous Neumann boundary condition corresponding to vanishing normal velocity on the walls

$$\triangle\eta + k^2\eta = 0, \tag{5.1}$$

$$\frac{\partial\eta}{\partial\mathbf{n}} = 0 \text{ on walls}, \tag{5.2}$$

where $\mathbf{n}$ is a vector normal to the boundaries of the channel and the wavenumber k satisfies the dispersion relation for water waves $\omega^2 = gk\tanh(kh)$, where g denotes the gravitational acceleration, ω stands for the angular frequency, and h is a depth of the channel. Further reduction of the 2D Helmholtz equation is obtained by assuming that the wavelengths are sufficiently large (low frequencies). Assuming the cut-off as $k < \pi/w_2$ (Section 1.3), preventing the propagation of the transverse modes, we can

(a) 2D continuous

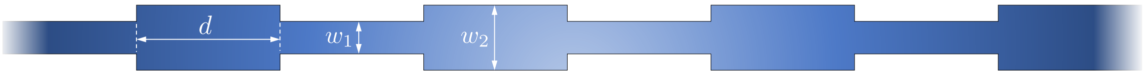

(b) 1D continuous

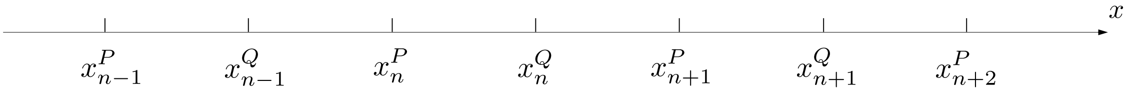

(c) 1D discrete

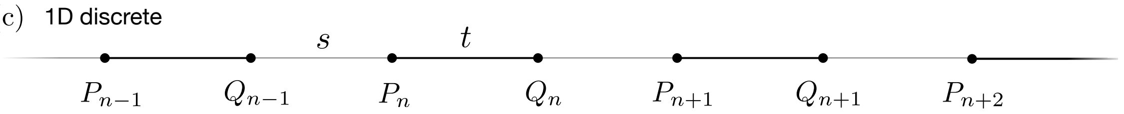

Fig. 5.1 (a) Scheme of the two-dimensional water wave periodic channel consisting of the cells with different widths w_1, w_2 and the length d. (b) One-dimensional continuous approximation leaves us with η depending only on x. On the axis, we identify points corresponding to the change of the channel widths. (c) Scheme of the one-dimensional discrete SSH model corresponding to the water wave channel.

proceed with the one-dimensional, continuous wave equation

$$\eta'' + k^2\eta = 0, \tag{5.3}$$

where now $\eta = \eta(x)$ depends only on the horizontal direction x. There are two types of cross sections: P and Q; section P occurs where $w_1 \to w_2$; section Q occurs where $w_2 \to w_1$. At each cross section, where the width of the channel is changing, we must ensure the continuity of the free surface elevation and its derivative (flow rate) with the jump conditions

$$[\eta] = 0, \tag{5.4}$$

$$[w\eta'] = 0, \tag{5.5}$$

where $[f] = f^+ - f^-$ describes the difference at each cross section from the right side limit (f^+) and the left side limit (f^-). Having reduced the two-dimensional continuous model into the one-dimensional continuous, we can proceed with a further reduction to the one-dimensional discrete description. Owing to the known analytical solution to the equation (5.3) with the condition (5.4) we derive the relationship between the neighboring points (here for sections Q)

$$\eta(x_n^Q) = \eta(x_n^P)\cos kd + \frac{\eta'(x_n^{P+})}{k}\sin kd, \tag{5.6}$$

$$\eta(x_{n-1}^Q) = \eta(x_n^P)\cos kd - \frac{\eta'(x_n^{P-})}{k}\sin kd. \tag{5.7}$$

Multiplying equation (5.6) by w_2, equation (5.7) by w_1 and summing them, we obtain

$$w_2\eta(x_n^Q) + w_1\eta(x_{n-1}^Q) = (w_1 + w_2)\eta(x_n^P)\cos kd + \frac{\sin kd}{k}\underbrace{\left(w_2\eta'(x_n^{P+}) - w_1\eta'(x_n^{P-})\right)}_{=0,\text{ by continuity (5.5)}}. \tag{5.8}$$

As shown above, taking advantage of the condition (5.5) we can eliminate the derivatives at given points. Following the same approach for the sections P we have

$$w_2\eta(x_n^P) + w_1\eta(x_{n+1}^P) = (w_1 + w_2)\eta(x_n^Q)\cos kd + \frac{\sin kd}{k}\underbrace{\left(-w_2\eta'(x_n^{Q-}) + w_1\eta'(x_n^{Q+})\right)}_{=0,\text{ by continuity (5.5)}}. \tag{5.9}$$

We introduce the coupling coefficients s and t as

$$s = \frac{w_1}{w_1 + w_2} \quad \text{and} \quad t = \frac{w_2}{w_1 + w_2}. \tag{5.10}$$

They depend only on the geometry of the system, are positive, and their sum is equal to unity

$$s + t = 1. \tag{5.11}$$

Now, identifying $E \equiv \cos kd$, and for the sake of simplicity writing that

$$Q_n \equiv \eta(x_n^Q) \quad \text{and} \quad P_n \equiv \eta(x_n^P), \tag{5.12}$$

we can ultimately describe our system by

$$sQ_{n-1} + tQ_n = EP_n, \tag{5.13}$$

$$tP_n + sP_{n+1} = EQ_n. \tag{5.14}$$

which in fact corresponds to the eigevalue problem

$$\mathbb{H}\mathbf{X} = E\mathbf{X}, \tag{5.15}$$

where

$$\mathbb{H} = \begin{pmatrix} \ddots & \ddots & & & & \\ \ddots & 0 & s & & & \\ & s & 0 & t & & \\ & & t & 0 & s & \\ & & & s & 0 & \ddots \\ & & & & \ddots & \ddots \end{pmatrix} \quad \text{and} \quad \mathbf{X} = \begin{pmatrix} \vdots \\ Q_{n-1} \\ P_n \\ Q_n \\ P_{n+1} \\ \vdots \end{pmatrix}. \tag{5.16}$$

The above representation of our system **directly matches the SSH model**. Moreover, the pseudoenergy $E(k) = \cos kd$ is analogous to its SSH model counterpart. Since the SSH Hamiltonian $\mathbb{H}$ depends exclusively on the geometry, the eigenfrequencies k are directly given by the eigenvalues of $\mathbb{H}$.

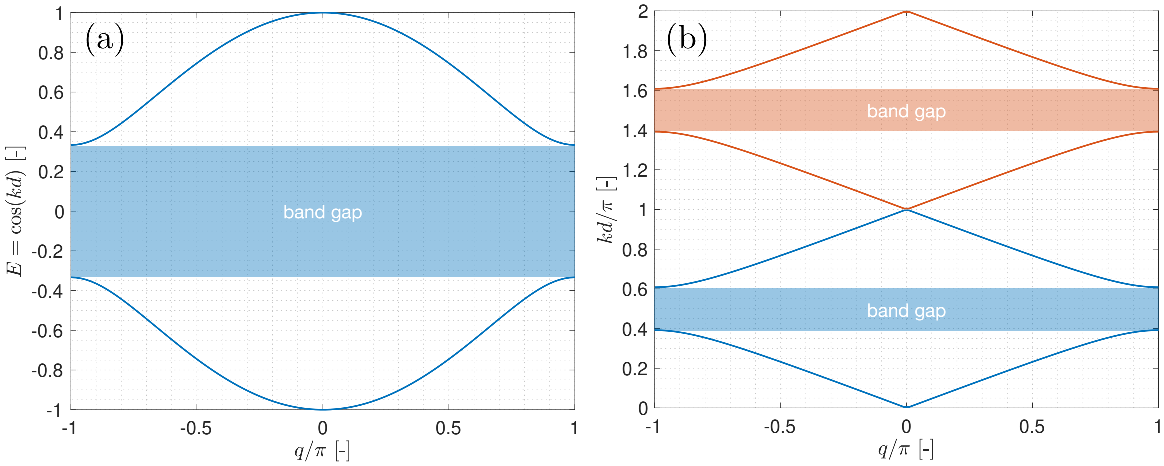

Fig. 5.2 The dispersion relation of the SSH model (5.19). (a) Pseudoenergy E as a function of the Bloch wavenumber q for $s = 1/3$. (b) The unwound dispersion relation - undimensionalized wavenumber k over the Bloch wavenumber q for $s = 1/3$.

In order to find the dispersion relation of the system, we assume the Bloch wave solution given by

$$P_n = P\mathrm{e}^{\mathrm{i}qn} \quad \text{and} \quad Q_n = Q\mathrm{e}^{\mathrm{i}qn}, \tag{5.17}$$

where q is the Bloch wavenumber. By substituting (5.17) into (5.13) and (5.14), we end up with an eigenvalue problem

$$\begin{pmatrix} 0 & s\mathrm{e}^{-\mathrm{i}q} + t \\ s\mathrm{e}^{\mathrm{i}q} + t & 0 \end{pmatrix} \begin{pmatrix} P \\ Q \end{pmatrix} = E \begin{pmatrix} P \\ Q \end{pmatrix}. \tag{5.18}$$

This 2×2 Hamiltonian matrix of the periodic one-dimensional SSH system allows to find directly the dispersion relation of the system

$$E = \cos kd = \pm\sqrt{s^2 + 2st\cos q + t^2}. \tag{5.19}$$

Owing to the chiral symmetry [42], the dispersion relation is symmetric around $E = 0$ (Fig. 5.2a) that can be unwound as $kd = (m + 1/2)\pi$ $(m = 0, 1, 2\ldots)$ (Fig. 5.2b).

Moreover, it appears that the first zero energy mode ($E = 0$) occurs when the wavelength λ is four times larger than the length of the segment d. It can be easily derived as $E = 0 \rightarrow kd = \pi/2 \rightarrow \lambda = 4d$.

5.2 Numerical illustration

To further illustrate the usefulness of the SSH model for water waves, we consider a finite channel with $2N = 14$ segments and its symmetric analog with $2N + 1 = 15$ segments. The channel is closed on both ends, which is accounted for by the homogenous Neumann boundary condition on each wall, where normal velocity vanishes. This fact can be represented by changing the first and last equation and introducing so-called *ghost nodes*: $G_0 \equiv Q_0$ at the beginning of the channel, and $G_1 \equiv Q_N$ at the end, that satisfy $EG_0 = P_1$, and $EG_1 = P_N$ for the case with even number of segments ($2N$). The Hamiltonian and the vector of unknowns of the eigenvalue problem $\mathbb{H}\mathbf{X} = E\mathbf{X}$ then becomes

$$\mathbb{H} = \begin{pmatrix} 0 & 1 & 0 & \dots & \dots & \dots & 0 \\ s & 0 & t & & & & \vdots \\ 0 & t & 0 & s & & & \vdots \\ \vdots & & \ddots & \ddots & \ddots & & \vdots \\ \vdots & & & t & 0 & s & 0 \\ \vdots & & & & s & 0 & t \\ 0 & \dots & \dots & \dots & \dots & 1 & 0 \end{pmatrix} \quad \text{and} \quad \mathbf{X} = \begin{pmatrix} G_0 \\ P_1 \\ Q_1 \\ \vdots \\ Q_{N-1} \\ P_N \\ G_1 \end{pmatrix}. \tag{5.20}$$

Similarly, we can obtain the Hamiltonian $\mathbb{H}$ for the case with an odd number of segments. The eigenvalues obtained from the SSH model for the case with an even number of segments is shown in Fig. 5.3a and for the case with an odd number of segments is reported in Fig. 5.3b (for all possible values of s and $t = 1 - s$). Due to the recurrent nature of the model (5.13, 5.14) it is straightforward to obtain an explicit form of the zero energy mode localized at the edge for the system (5.20)

$$\begin{pmatrix} P_n \\ Q_n \end{pmatrix} = c \begin{pmatrix} 0 \\ 1 \end{pmatrix} \left(-\frac{s}{t}\right)^n, \tag{5.21}$$

where c is the normalization constant.

Parallelly to this analysis, we numerically solve the full two-dimensional eigenvalue problem corresponding to the even and odd case separately

$$\triangle\eta = -k^2\eta, \tag{5.22}$$

$$\frac{\partial\eta}{\partial\mathbf{n}} = 0 \text{ on walls.} \tag{5.23}$$

The solution is obtained using Finite Element Method for $w_1 = 0.05$, $w_2 = 0.1$, $d = 0.1$, $L = 1.4$ (L being the total length of the channel), and is shown in Fig. 5.3a for the case with an even number of segments, and in Fig. 5.3b for the case case with an odd number of segments. It can be clearly seen that for an even number of segments ($2N = 14$, Fig. 5.3a) the system hosts one localized mode with zero energy. For $s < t$ the edge wave is localized on the left side of the channel (Fig. 5.4a) and *vice versa*, for $s > t$ the mode is localized on the right side (Fig. 5.4c). This behavior can be easily explained when we look again at the form of the edge wave (5.21) derived from the SSH model. It appears that only the edge segments where $w_1 < w_2$ are able to host the edge wave.

Analyzing the case where we have an odd number of segments ($2N + 1 = 15$, Fig. 5.3a), we see that for $s < t$, our system can host two zero energy modes - one localized at the left end and the other localized at the right end. For $s > t$, the edge mode disappears, as our system is unable to host the localized edge wave since on both ends we have segments with $w_1 > w_2$. It is worth mentioning that for $s = t$, we obtain the case where the channel is rectangular, thus the localization of the zero energy mode does not occur (Fig. 5.4b).

The slight difference between eigenvalues obtained by the SSH model and the numerical solution can be explained by the fact that one-dimensional approximation is not able to account for the actual widths of the channel. However, the one-dimensional approximation is still satisfactorily accurate as long as the aspect ratio of the segments is small enough and the wavelength is large compared to the width of the channel.

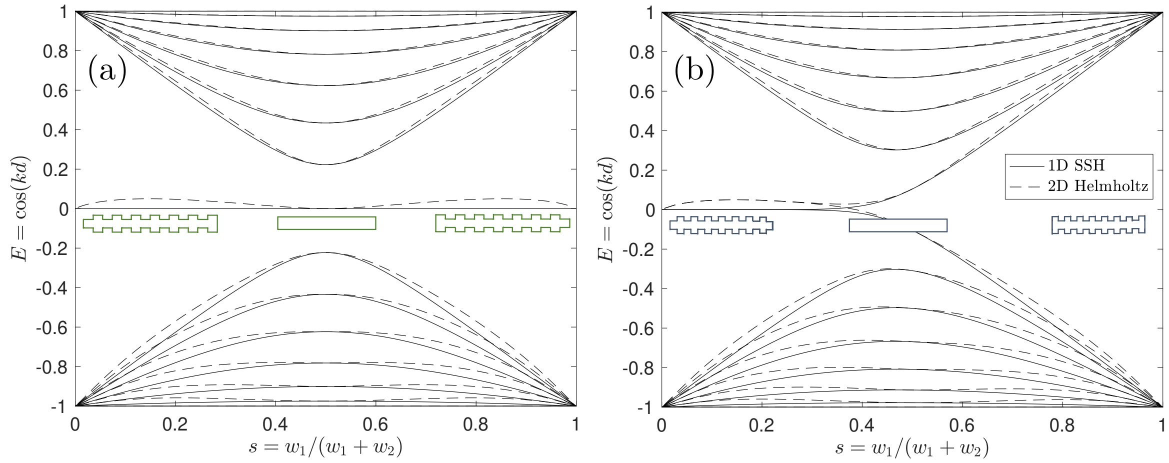

Fig. 5.3 The eigenvalues of the channel with (a) an even number of segments ($2N = 14$) and (b) an odd number of segments ($2N + 1 = 15$) obtained by the SSH model (plain curves) and the numerical simulation (dashed curves) as a function of the parameter s.

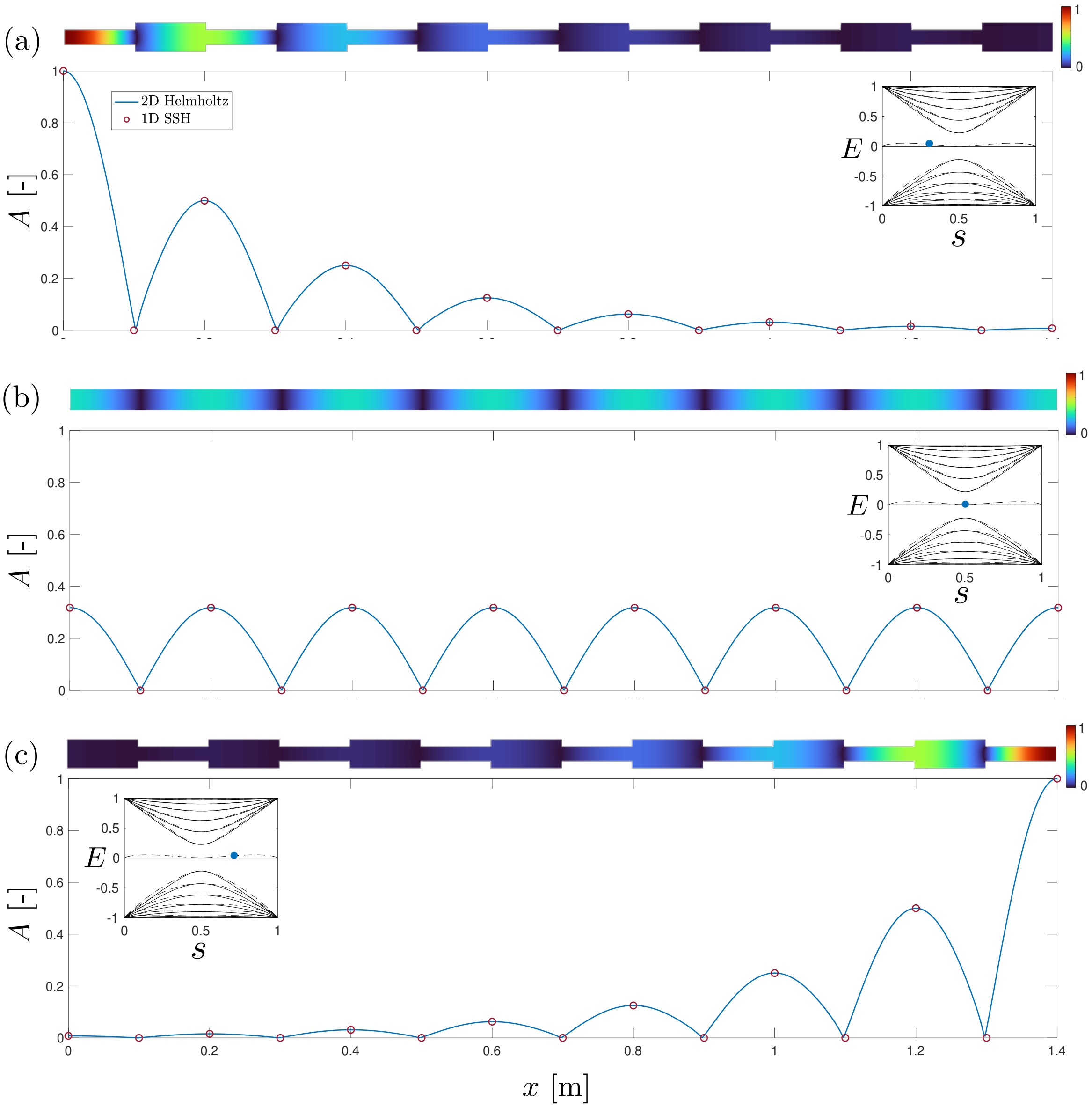

Fig. 5.4 The amplitude of the edge mode defined as the absolute value of the free surface elevation $A = |\eta(x, y)|$ for different values of the coupling coefficient: (a) $s = 1/3$, (b) $s = 1/2$, and (c) $s = 2/3$. The comparison between the SSH model prediction (symbols) and the numerical simulation using Finite Element Method (plain curves).

5.3 Experimental setup

The experimental setup is based on a periodic channel (Fig. 5.5a) of the length $L = 140\,\text{cm}$ and periodically varying width $w_1 = 5\,\text{cm}$ and $w_2 = 10\,\text{cm}$ that corresponds to $s = 1 - t = 1/3$. The channel consists of 14 segments of the length $d = 10\,\text{cm}$. The height of the channel is equal to 5 cm so that it can accommodate the layer of water of the depth $h = 2\,\text{cm}$ that is constant throughout the experiments. The aspect ratio of the cells is small enough to accurately mimic the characteristics of the SSH model, as shown in the previous section. On the other hand, it has to be sufficiently big in order to avoid the detrimental effects of the meniscus that forms on the walls of the channel and whose size is of the order of 2 mm. Its presence in the channel with a small aspect ratio could lead to the undesirable shift in eigenfrequencies of the channel [92]. The reference rectangular channel of the same length and width $w = 5\,\text{cm}$ is also

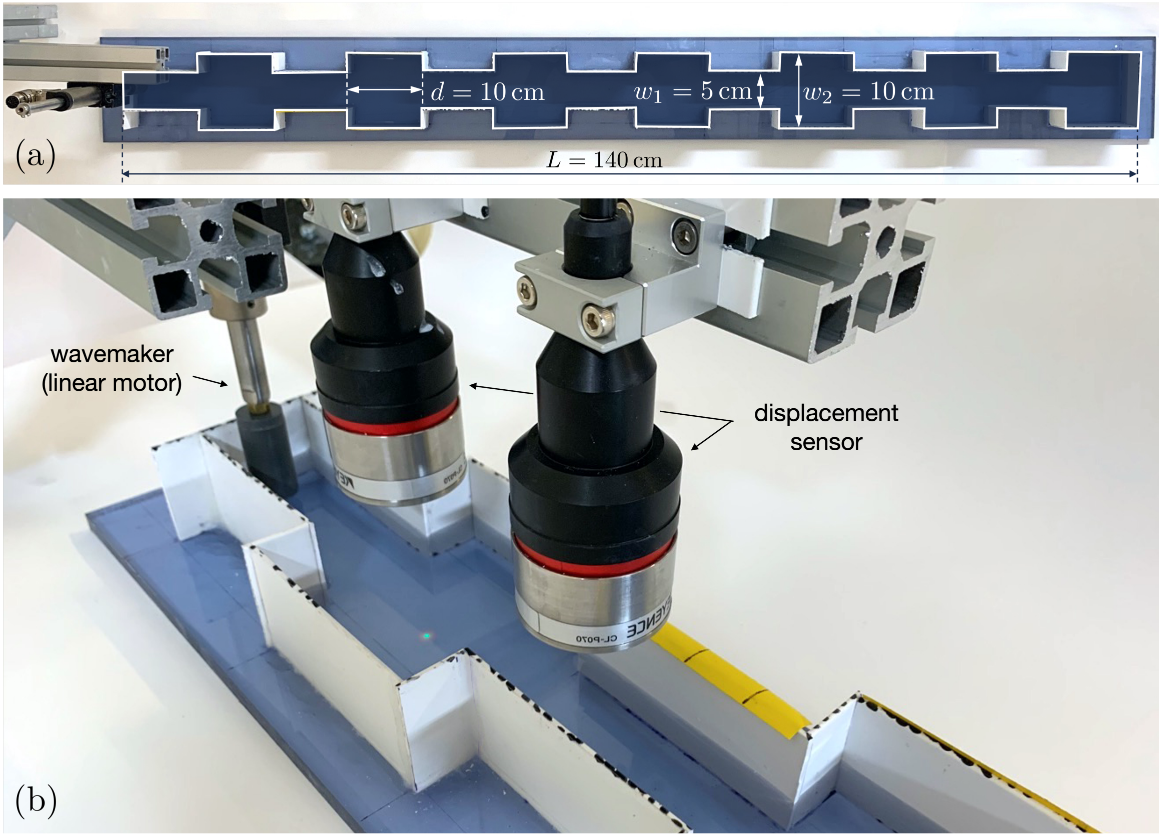

Fig. 5.5 (a) The photo of the periodic channel with dimensions. The wavemaker is placed at the left end of the channel (top view). (b) The picture of the left end of the channel with the wavemaker and the two confocal displacement sensors suspended above the channel.

manufactured in order to verify the regular modes of a straight cavity ($s = t$).

The realization of the point source is done by placing the wavemaker consisting of the linear motor with cylindrical tip (Fig. 5.5b) of the diameter $\phi_s = 2\,\text{cm}$ and that is placed on the left end of the channel in the segment of smaller width, 0.5 cm from the wall. The wavemaker realises vertical sinusoidal motion of the amplitude range $A_s \in [0.5\,\text{mm}, 15\,\text{mm}]$ and the frequency up to $f_s = 2.5\,\text{Hz}$, which corresponds to the cut-off needed by the one-dimensional approximation.

Two confocal displacement sensors are placed above the channel (Fig. 5.5b) and are separated by the interval of 10 cm, corresponding to the length of the segment, allowing to measure at two cross sections simultaneously to facilitate the measurements. The sensors are connected to the trolley to quickly change its position and measure at different points along the channel.

5.4 Experimental results

The confocal displacement sensors provide the signal with an acquisition frequency of 1 kHz. The source is positioned at the left end of the channel where the maximum amplitude of the edge mode is expected.

5.4.1 Linear regime

The wavemaker realizes the vertical pseudoperiodic motion corresponding to the chirp signal (Section 3.5), whose length is $t = 60\,\text{s}$ and whose frequency spectrum varies from 0.1 to 2.5 Hz so that the first cut-off frequency is fully covered. The spectrum is measured every 2.5 cm. We report in Fig. 5.6a the average of all measured spectra for the periodic channel with $s = 1/3$. The edge mode is visible at $f_E = 1.097\,\text{Hz}$ which corresponds to $kd = \pi/2$ and is represented by the most prominent resonance peak surrounded by the large band gap. Vertical dashed lines correspond to the eigenvalues given by the numerical solution of the two-dimensional Helmholtz eigenproblem (5.23) and are in excellent agreement with the experimental results.

A similar procedure is done for the rectangular channel ($s = 1/2$). We can see that resonance modes are now equally spaced (Fig. 5.6b) and follow the regular modes of the rectangular cavity as expected ($kL = m\pi$ with $m = 1, 2, \dots$). The comparison between the experimental values (dots), one-dimensional prediction by the SSH model (plain curves), and the two-dimensional eigenproblem solved numerically (dashed curves) is shown in Fig. 5.6c. Local maxima obtained experimentally for $s = 1/3$ (blue dots)

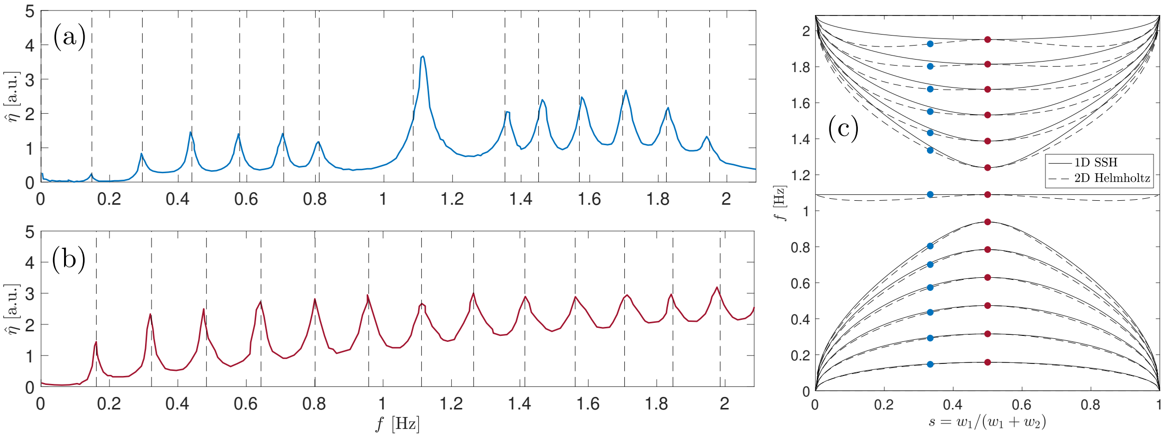

Fig. 5.6 (a) Averaged spectrum of the free-surface elevation for $s = 1/3$ (blue curve) with a 2D numerical prediction (dashed lines). (b) Averaged spectrum of the free-surface elevation for $s = 1/2$ (orange curves) with a numerical prediction (dashed lines). (c) Comparison of the 1D (plain lines) and the 2D (dashed lines) prediction of the eigenvalues with the experimental values for $s = 1/3$ (blue dots) and $s = 1/2$ (orange dots).

and $s = 1/2$ (orange dots) are reported. An excellent agreement of theoretical and experimental results is obtained with a slight difference between 1D and 2D models coming from the geometry's aspect ratio.

The ensemble of the experimental results is presented in Fig. 5.7b and is compared to the numerical simulation using Finite Element Method Fig. 5.7a. The simulation is carried out as follows. We solve the two-dimensional Helmholtz equation with a source term $s(x, y)$

$$\triangle\eta + k^2\eta = s(x, y), \tag{5.24}$$

$$\frac{\partial\eta}{\partial\mathbf{n}} = 0 \text{ on walls.} \tag{5.25}$$

for wavenumbers $k = \kappa + \mathrm{i}\beta$, where the imaginary part of the wavenumber accounts for the viscous attenuation in the bulk and is given by Stokes equation

$$\beta = \frac{4\kappa^2\mu\omega}{\rho g + 3\gamma\kappa^2}, \tag{5.26}$$

where μ denotes dynamic viscosity, ρ is water density, g stands for the gravitational acceleration, and γ is the surface tension. The source is modelled as a Gaussian bell of

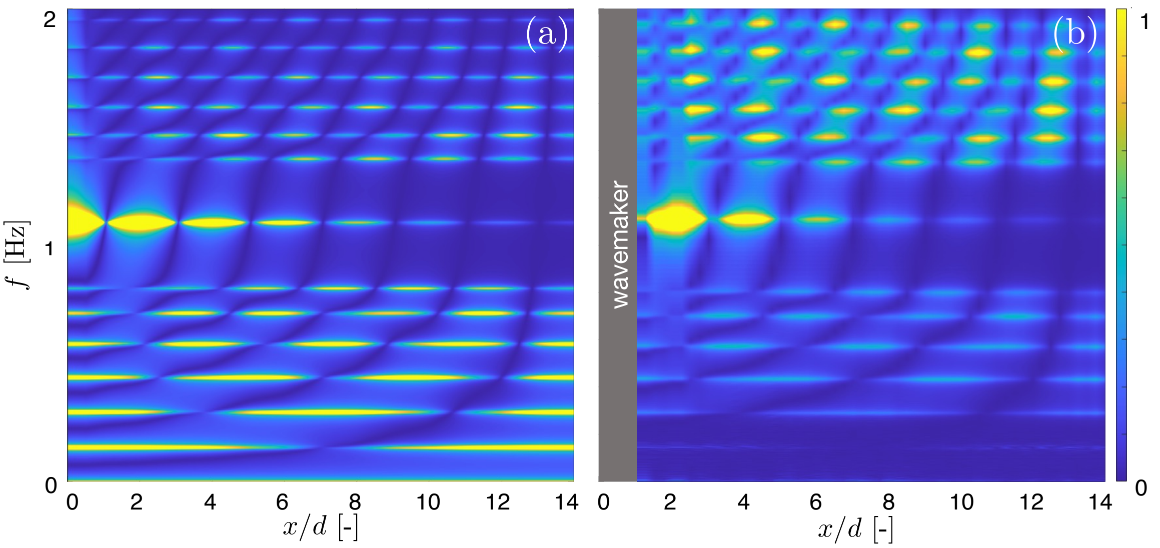

Fig. 5.7 (a) The absolute value of the free surface elevation obtained using Finite Element Method. (b) Experimental results for $s = 1/3$.

the form

$$s(x,y) = \frac{1}{2\pi\sigma_x\sigma_y}\exp\left[-\left(\frac{(x-x_0)^2}{2\sigma_x^2}+\frac{(y-y_0)^2}{2\sigma_y^2}\right)\right], \tag{5.27}$$

where $\sigma_x = \sigma_y = w_1/30$, $x_0 = d/2$, and $y_0 = w_2/2$. The profile of the wave is obtained by averaging the result along the y axis and is presented in Fig. 5.7a for different frequencies $f = \omega/2\pi$, where $\omega^2 = gk\tanh(kh)$.

The edge mode localized at the left side of the channel is clearly visible and corresponds very well to the numerical simulation. It is surrounded by the band gap after which we see the bulk modes of the channel. The profile of the absolute value

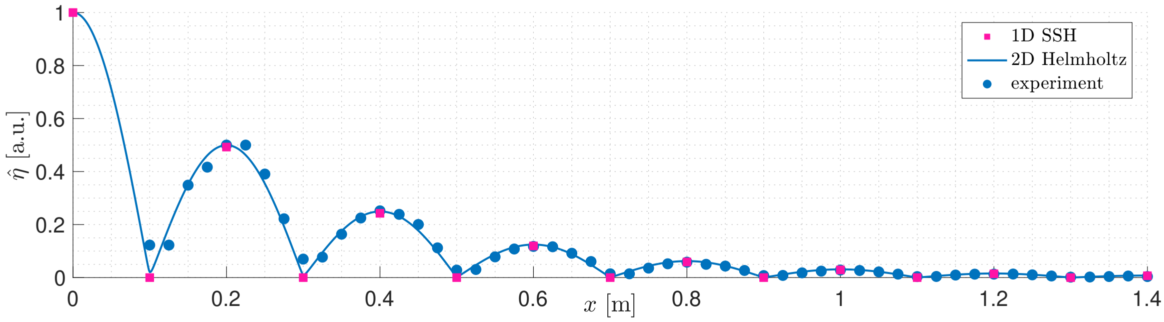

Fig. 5.8 The edge mode localized at the left side of the channel obtained experimentally (blue dots), by 2D simulation (plain curve), and by the SSH model (5.21) (pink symbols).

of the free surface elevation for the edge mode is presented in Fig. 5.8. An excellent agreement is obtained between the experiment and both 2D and 1D SSH prediction.

5.4.2 Nonlinear regime

With increasing amplitude of the source, i.e., the wave's amplitude, the appearance of secondary peaks around the resonance peak of the edge mode is observed. To further investigate this phenomenon, the dependence of the spectrum on the amplitude is studied. Since we are no longer in the linear regime, the approach using a chirp signal that benefits from the linear properties of the Fourier transform can no longer be used. Therefore, the point source realizes vertical sinusoidal motion with the frequency f_s and the amplitude A_s. Two sets of measurements are studied for different values of f_s and A_s. Both of them are focused around the frequency of the edge mode. The first set is done for

$$\begin{aligned} A_s &\in [0.5, 0.6, 0.7, \ldots, 1.9, 2.0, 2.5, \ldots, 4.5, 5, 6, \ldots, 9, 10]\,\mathrm{mm}, \\ f_s &\in [1.040, 1.160]\mathrm{Hz}, \quad \Delta f_s = 0.002\,\mathrm{Hz}, \end{aligned} \tag{5.28}$$

and the second set

$$\begin{aligned} A_s &\in [0.5, 0.7, 0.9, 1.1, 1.3, 1.5, 2.0, 2.5, 5, 10, 15]\,\mathrm{mm}, \\ f_s &\in [0.900, 1.200]\,\mathrm{Hz}, \quad \Delta f_s = 0.003\,\mathrm{Hz}. \end{aligned} \tag{5.29}$$

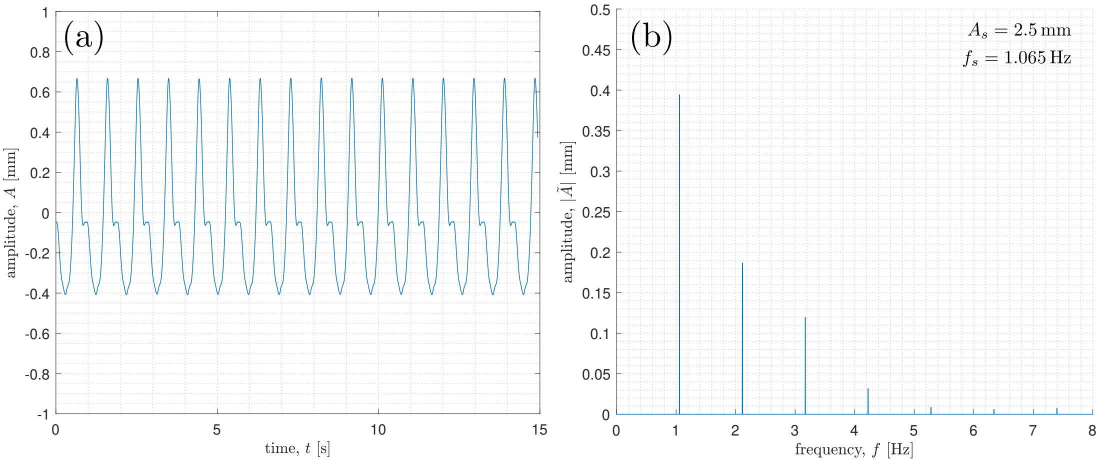

Fig. 5.9 (a) The example of the experimental measurement for $A_s = 2.5\,\mathrm{mm}$, $f_s = 1.065\,\mathrm{Hz}$ and (b) corresponding spectrum.

For each amplitude of the source A_s, the amplitude of the wave is registered using a confocal displacement sensor at $x/d = 4$. The signal of the length $t = 20\,\mathrm{s}$ is measured for a given frequency f_s, then the frequency is increased by Δf_s, and the stationary state of the wave is anticipated before registering the next signal. Usually it takes around 80 s to measure one signal for the pair (A_s, f_s). Due to the time consuming procedure, an automatic script is put in place that changes both A_s and f_s and registers the signals. To avoid the change of the water properties, the channel is covered with a transparent foil preventing the surface from being polluted, and also to suppress the evaporation that would result in decreasing the water depth and therefore changing the resonant frequencies. The example of the measurement for one pair of $(A_s, f_s) = (2.5\,\mathrm{mm}, 1.065\,\mathrm{Hz})$ is shown in Fig. 5.9. The signal is carefully trimmed to obtain an integer number of periods to extract the exact values of its spectrum.

The determination of the resonance curves is done by extracting the values of the fundamental frequency, first five harmonics $(f_0, \ldots, f_5)$ and its amplitudes $(A_0, \ldots, A_5)$ (Fig. 5.10). One measurement for the pair of (A_s, f_s) represents one point on the resonance curve.

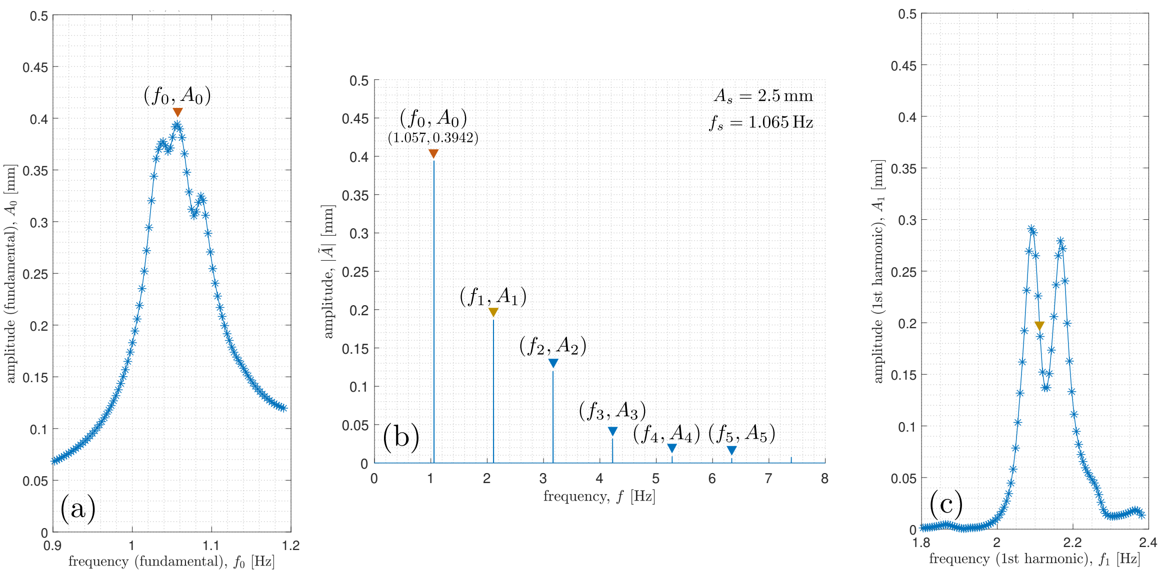

Fig. 5.10 The determination of the resonance curves. The resonance curve of (a) the fundamental frequency $A_0(f_0)$ and (c) the first harmonic $A_1(f_1)$ for $A_s = 2.5\,\mathrm{mm}$. (b) The spectrum of the the measurement for $(A_s, f_s) = (2.5\,\mathrm{mm}, 1.065\,\mathrm{Hz})$ from which the values of the frequencies $(f_0, \ldots, f_5)$ and the amplitudes $(A_0, \ldots, A_5)$ are extracted. The example shows the position of (f_0, A_0) (red triangle) and (f_1, A_1) (yellow triangle) on the corresponding resonance curves (a) and (c) respectively.

We report in Fig. 5.11 three different regimes of the resonant behavior of the edge mode for $A_s = 0.7\,\mathrm{mm}$ (Fig. 5.11a), $A_s = 2.5\,\mathrm{mm}$ (Fig. 5.11b), and $A_s = 15\,\mathrm{mm}$ (Fig. 5.11c). As the driving frequency f_s corresponds almost exactly to the fundamental frequency f_0 and the harmonics ($f_1 = 2f_0, f_2 = 3f_0, \dots$) (with an error smaller than 1%, inset Fig. 5.11a) we compare them on the same horizontal axis f_s.

We can see that for $A_s = 0.7\,\mathrm{mm}$ we obtain only one resonant peak of the edge mode, and the contribution of higher harmonics is relatively small (less than 20 %). For the amplitude of the source of $A_s = 2.5\,\mathrm{mm}$ (Fig. 5.11b) secondary peaks around the main resonant peak of the edge mode appear (first bifurcation). The contribution of the harmonics becomes more important. It seems that the peak on the right side of the peak of the fundamental frequency (blue curve) of the edge mode corresponds to the maximum of the second harmonic (yellow curve). On the other hand, the left side peak correlates with the maximum of the first harmonic (orange curve). With further increase of the amplitude A_s we can observe the emergence of two more peaks (second bifurcation) reported in Fig. 5.11c where the resonant curves for $A_s = 15\,\mathrm{mm}$ are shown. The amplitudes of the first and second harmonic are now higher than the fundamental frequency amplitude.

Experimental measurements show the existence of strong nonlinear interactions near the resonant frequency of the edge mode. Similar behavior for the rectangular channel was obtained experimentally and described theoretically in [93–95]. The apparent energy transfer between the fundamental frequency and the harmonics can be obtained using the approach presented in [96].

To further investigate the emergence of the resonant peaks around the edge mode, we introduce the Ursell number as follows

$$U = \frac{A_s \lambda^2}{h^3}, \tag{5.30}$$

where $\lambda = 4d$ stands for the wavelength of the edge mode and h denotes the water depth. The ensemble of the measurements is shown in Fig. 5.12 for the range (5.29) and in Fig. 5.13 for the range (5.30). It appears that the first bifurcation, where two secondary peaks emerge, happens when the Ursell number $U \approx 25$. The peaks are placed almost symmetrically at around $\pm 5\% f_E$ away from the main resonance of the edge mode (f_E). The second bifurcation, i.e., when two additional peaks arise at approximately $\pm 10\% f_E$ away from the original edge mode resonance, occurs at $U \approx 100$.

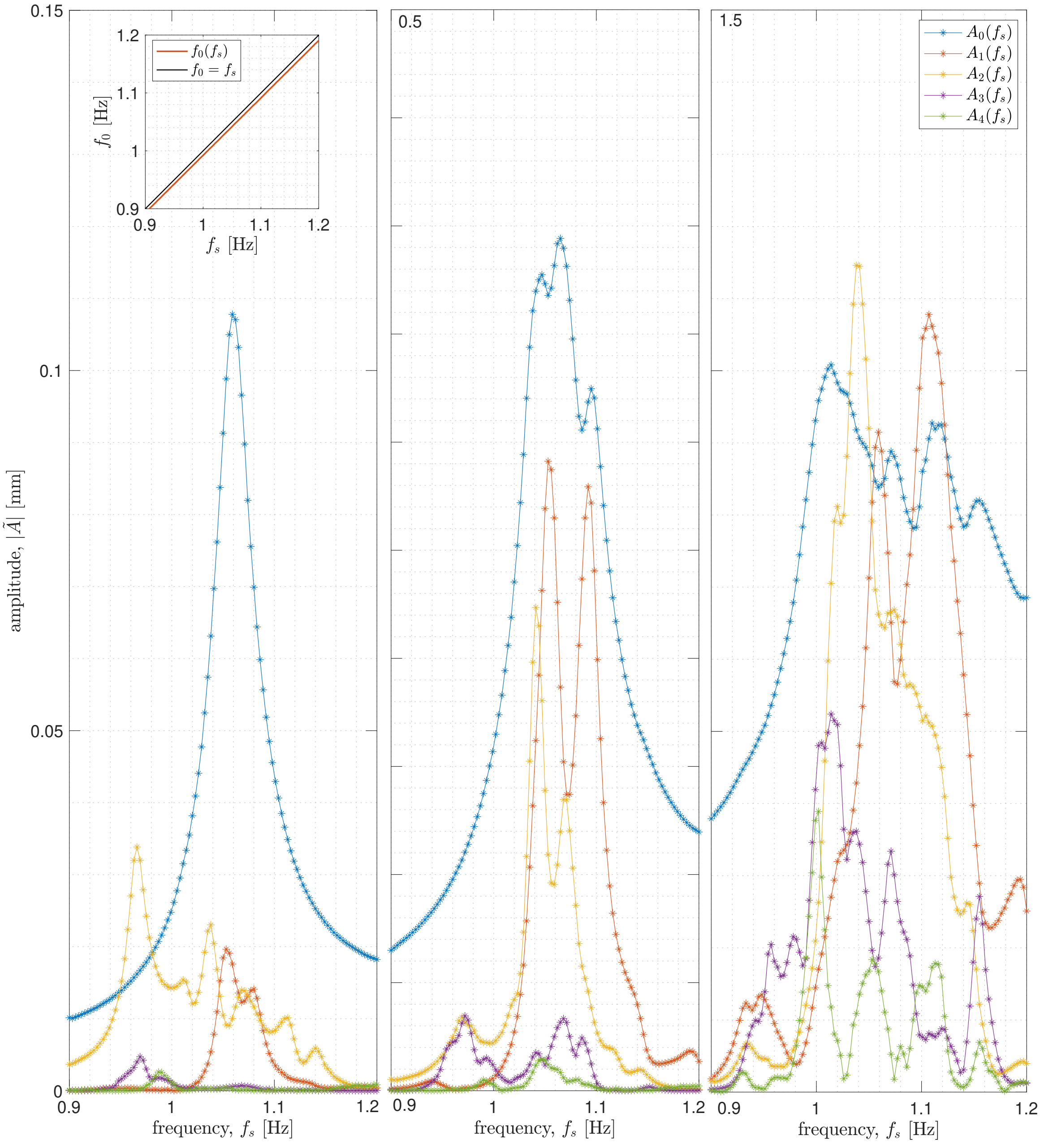

Fig. 5.11 Resonant curves of the fundamental frequency $A_0(f_s)$ (blue curve), the first harmonic $A_1(f_s)$ (orange curve), the second harmonic $A_2(f_s)$ (yellow curve), the third harmonic $A_3(f_s)$ (purple curve), and the fourth harmonic $A_4(f_s)$ (green curve) for (a) $A_s = 0.7\,\text{mm}$, (b) $A_s = 2.5\,\text{mm}$, and (c) $A_s = 15\,\text{mm}$. The inset of (a) shows the relation between the driving frequency f_s and the measured fundamental frequency f_0.

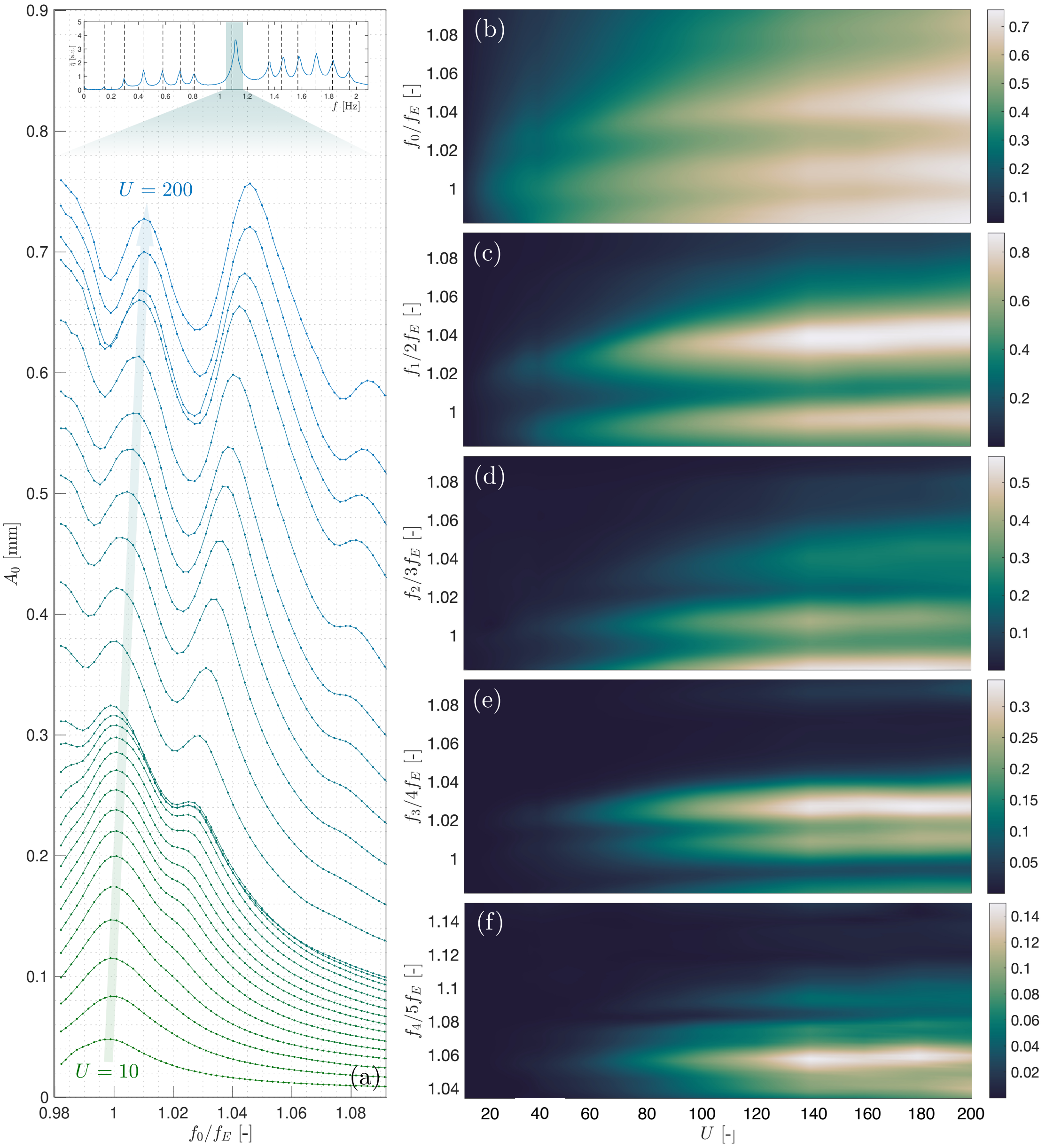

Fig. 5.12 (a) Resonant curves for the set of measurements (5.29) for the fundamental frequency. (b) The measured amplitude of the normalized fundamental frequency f_0/f_E as a function of the Ursell number U. (c) The measured amplitude of the first harmonic $f_1/2f_E$ as a function of the Ursell number U. (d) The measured amplitude of the second harmonic $f_2/3f_E$ as a function of the Ursell number U. (e) The measured amplitude of the third harmonic $f_3/4f_E$ as a function of the Ursell number U. (f) The measured amplitude of the fourth harmonic $f_4/5f_E$ as a function of the Ursell number U. The inset shows the region around the edge mode peak, where the measurements are carried out.

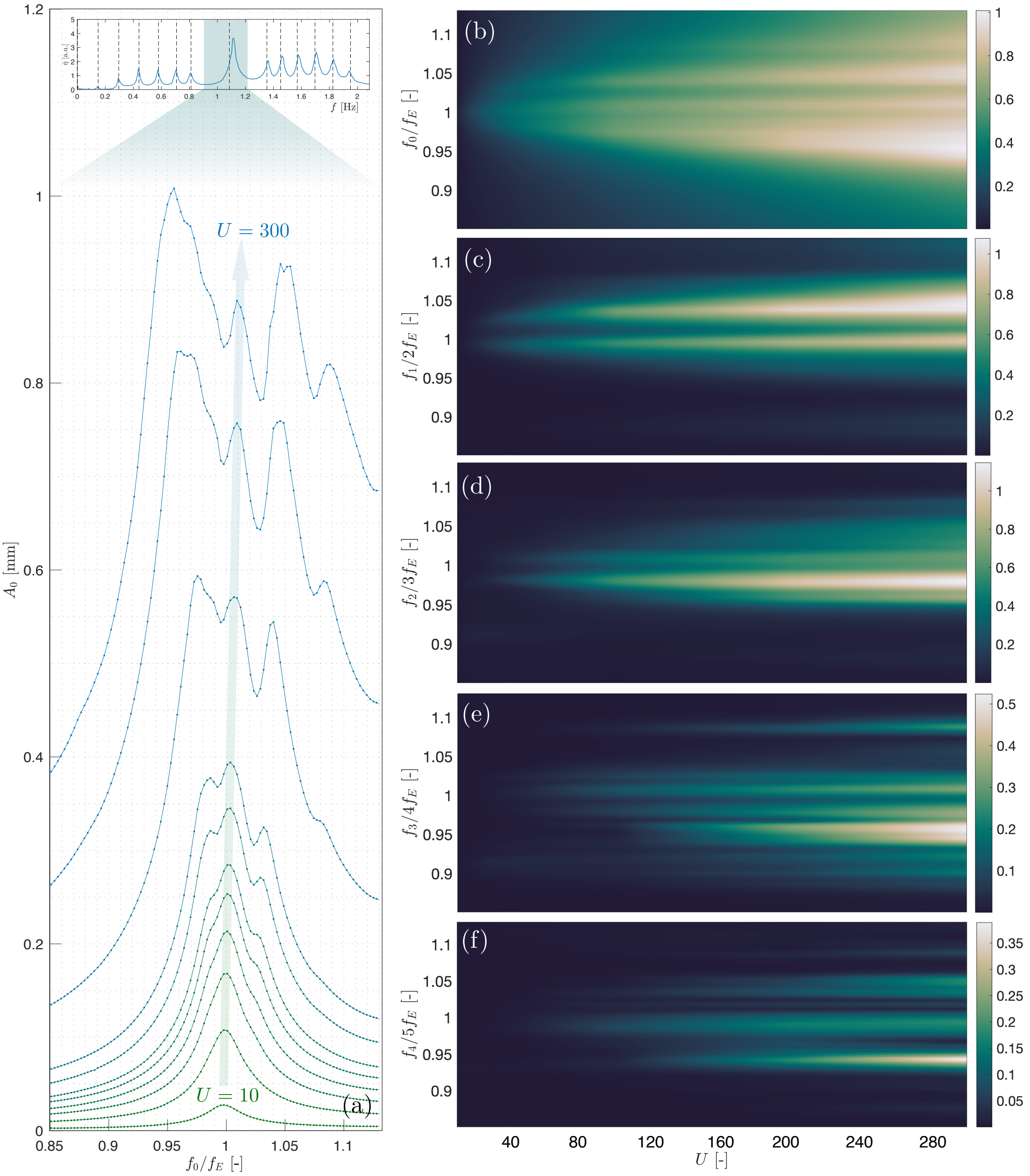

Fig. 5.13 (a) Resonant curves for the set of measurements (5.30) for the fundamental frequency. (b) The measured amplitude of the normalized fundamental frequency f_0/f_E as a function of the Ursell number U. (c) The measured amplitude of the first harmonic $f_1/2f_E$ as a function of the Ursell number U. (d) The measured amplitude of the second harmonic $f_2/3f_E$ as a function of the Ursell number U. (e) The measured amplitude of the third harmonic $f_3/4f_E$ as a function of the Ursell number U. (f) The measured amplitude of the fourth harmonic $f_4/5f_E$ as a function of the Ursell number U. The inset shows the region around the edge mode peak, where the measurements are carried out.

Subsequently, the form of the resonant modes near the edge mode is studied. The amplitude is measured at $x/d \in [2, 3, ..., 9]$. In the regime where the first bifurcation occurs, for $U = 50$, we can observe two secondary peaks (orange and yellow triangles) around the main edge mode peak (blue triangle) (Fig. 5.14a$_1$). It appears that the form of the mode still accurately follows the SSH prediction (5.21) and is immune to the slight change of the frequency, which is reported in Fig. 5.14a$_2$. We also show the prediction of the edge mode form obtained by using the two-dimensional numerical simulation of the Helmholtz equation. Similarly, in the regime where the second bifurcation occurs, two additional peaks emerge ($U = 300$, Fig. 5.14b$_1$), and the modes preserve their form following almost exactly the form of the edge mode (red squares) (Fig. 5.14a$_2$).

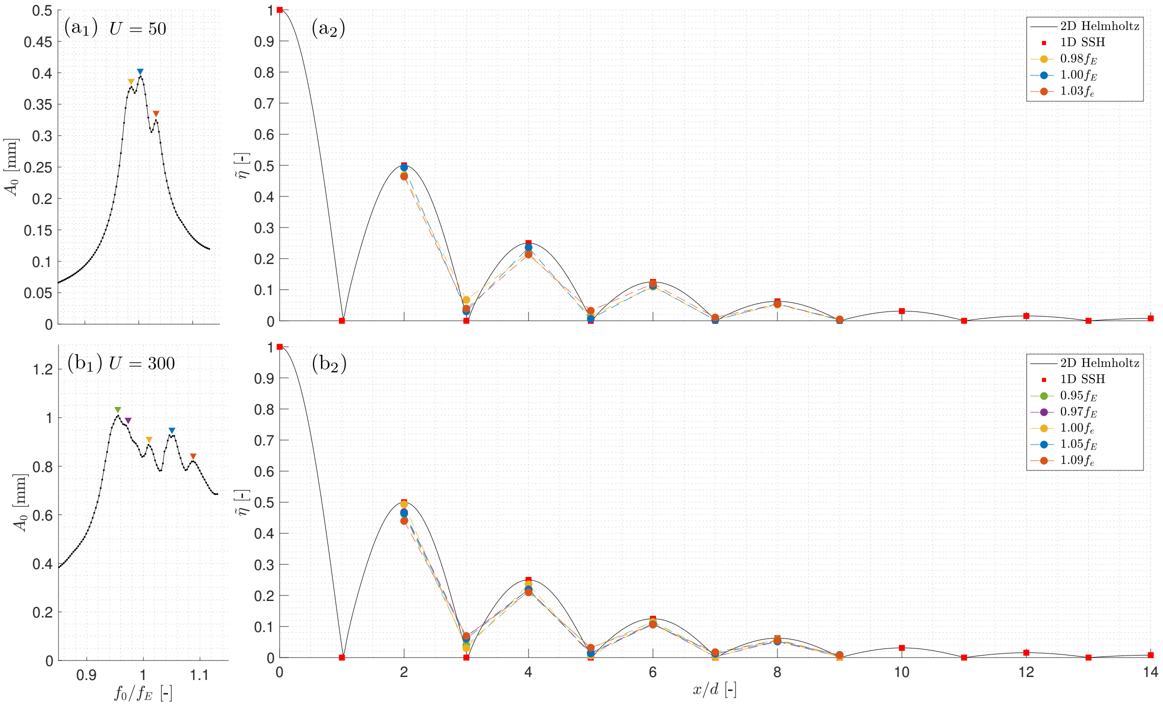

Fig. 5.14 (a$_1$) The spectrum for $U = 50$. The main resonant peak of the edge mode is shown (blue triangle), as well as corresponding secondary peaks on the right (yellow triangle) and left (orange triangle). (a$_2$) The modes for the main peak (blue symbols) and secondary peaks (yellow and orange symbols). The prediction of the 1D SSH model (red squares) and 2D Helmholtz equation (plain black curves). (b$_1$) The spectrum for $U = 300$. The main resonant peak (yellow triangle), corresponding secondary peaks (purple and blue triangle), and two additional peaks (green and orange triangles, respectively). (b$_2$) The form of the edge mode for the main peak (yellow symbols), secondary peaks (purple and blue symbols), and two additional peaks (green and orange symbols).

5.5 Conclusions

The main objective of the presented work is to experimentally investigate the topologically protected edge states and band gaps in a water waveguide with periodic geometry. One of the representations of the topological states provided by the Su-Schrieffer-Heeger model is applied to describe the observed phenomena. A waveguide with step periodic width ($s = 1/3$) and corresponding rectangular tank with constant width ($s = 1/2$) are manufactured and examined using confocal displacement sensors allowing the measurement of water free surface elevation. Two-dimensional numerical simulations are carried out in order to verify the SSH model and experimental data. The obtained results show that this very simple setup exhibits all the properties of the SSH model with an excellent agreement to the water wave systems.

Moreover, the system is also studied in the nonlinear regime, where two bifurcation regimes are found. The first bifurcation corresponds to the emergence of two secondary resonances around the primary edge wave resonance for Ursell number $U > 25$. The second bifurcation, with the appearance of two additional peaks around the main edge mode resonance, is recognized for $U > 100$. It is shown that the edge mode is immune to these subresonances and preserves its form even for a high degree of nonlinearity. This phenomenon, intuitively interpreted as energy transfer between the fundamental frequency and harmonics, needs further theoretical study to be fully understood.

Chapter 6

Conclusions and perspectives

6.1 Summary and conclusions

In this thesis, we have presented various experimental aspects of wave propagation on the water surface. We have obtained the control of the water wave propagation through specially designed structures. We have shown several types of these structures that have been studied both theoretically and experimentally. First, we presented the way of controlling the wave by the array of vertical plates changing the shape of the bathymetry. Next, our attention focused on a similar stratified structure, but it was submerged between two layers of water this time. Both systems mentioned above had a characteristic length, i.e., spacing between the plates, much lower than the wavelength. Ultimately, we evaluated the unusual properties of the channel with periodically varying width and constant depth. In contrast to the previous ones, this setup had a characteristic length (length of the cell) comparable to the size of the wavelength.

Metabathymetry

In the first experimental part of this thesis (Chapter 3), we have shown the array of plates connected to the bottom of the tank to influence the water wave propagation. The wave, ”feeling” different water depths in different directions, was able to change its behavior to our wish.

We have chosen to study this kind of structure in the context of the cavity eigenmodes and eigenfrequencies. The specially designed metamaterial bathymetry allowed to preserve the regular, rectangular cavity properties in a deformed geometry. We have maintained both the eigenmodes' shape and the eigenfrequencies' values even for a high degree of deformation.

We have shown the advantages of the homogenization of the three-dimensional water wave problem over the two-dimensional approach. The presented experiments have shown that the homogenization of the three-dimensional water wave problem combined with coordinate transformation theory led to the successful design of the metabathymetry. The robustness of the anisotropic medium has been shown using space-time resolved measurements of the entire water wavefield. The applications of such a structure include shore protection, or creating a wave-free region by deviating the wave.

Submerged metamaterials

In Chapter 4, we have shown the ability of the submerged array of vertical plates, surrounded by two layers of liquid to provide an anisotropic medium for water wave propagation. We have established the dispersion relation for such a medium by using the homogenized model, a practical tool for designing the metamaterial structure. It could accurately predict the frequency band for which maximal anisotropy occurred.

This relation has been verified using Bloch-Floquet formalism and has shown a good agreement when foreseeing where the maximal anisotropy takes place. However, the obtained dispersion relation overestimates the degree of anisotropy.

We have performed an experimental study of such submerged structures for several different configurations. The measured wavefields have proved that an anisotropic behavior indeed occurs and obeys the developed theoretical model.

SSH model for water waves

The primary purpose of Chapter 5 was to investigate topologically protected edge states and bandgap in a waveguide with periodically varying width. One of the topological state representations provided by the Su-Schrieffer-Heeger model has been employed to describe the behavior of the water wave in such a medium. A rectangular waveguide with constant width and a tank with periodically varying width have been manufactured and inspected with a confocal displacement sensor by measuring the surface deformation.

The obtained experimental data has been compared with the results of the 2D numerical simulations and the prediction given by the SSH model. The results have shown that this uncomplicated setup presents all the properties of the SSH model with excellent agreement.

In addition, the system has been examined in a nonlinear regime where we have found two bifurcation regimes. The first bifurcation corresponds to the appearance of two secondary resonances around the original edge wave resonance. The second bifurcation, where two additional peaks appear, has also been recognized. We have seen that the shape of the edge mode is unaffected by these subresonances and retains its shape despite the nonlinearity of the wave.

6.2 Future works

The presented research opens a wide range of possibilities for the continuation of the development of metamaterials for water surface waves.

When it comes to the second project concerning submerged metamaterials (Chapter 4), higher-order homogenization can be done to improve the homogenized model and explain the differences between the model and the system's actual behavior. Since it has been shown that high anisotropy can be expected for a thin fluid layer, it can be considered to replace the layer with effective boundary conditions that would compensate for the discrepancies between the presented homogenization model and the actual metamaterial structure.

Detailed attention should be paid to describe theoretically the bifurcations found for a system described in the third project (Chapter 5), where the waveguide with periodically varying width is studied. More numerical and theoretical work is needed to fully understand and explain this phenomenon in a nonlinear regime.

Appendix A

Modal method for the unit cell of the metabathymetry

In the bulk, the single step satisfies the problem

$$\triangle \phi = 0, \tag{A.1}$$

where the boundary conditions are given by

$$\frac{\partial \phi}{\partial \mathbf{n}} = 0 \quad \text{on } \Gamma, \tag{A.1a}$$

$$\frac{\partial \phi}{\partial z} = \frac{\omega^2}{g} \phi \quad \text{at } z = 0. \tag{A.1b}$$

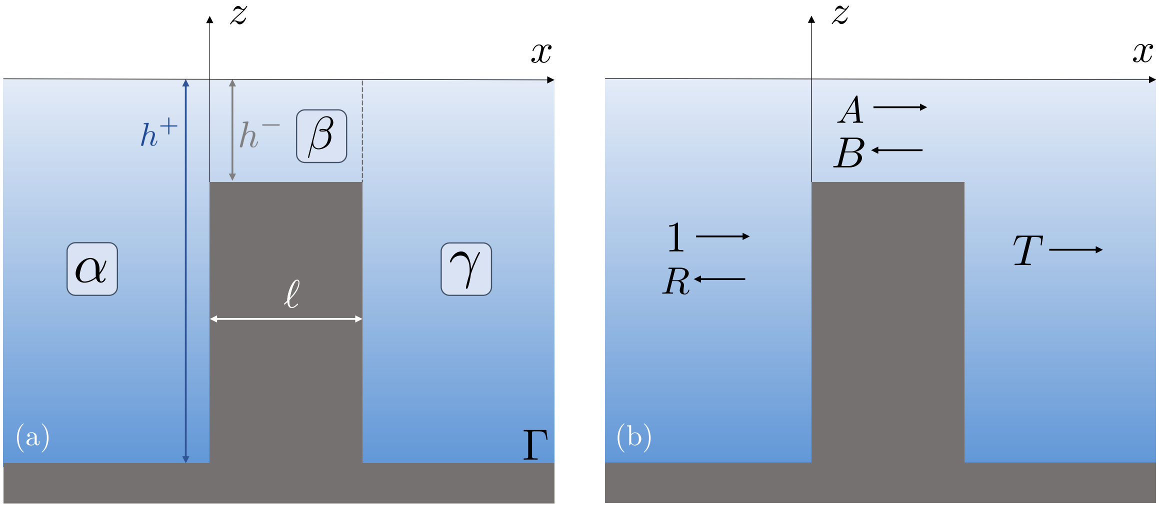

Fig. A.1 (a) Step scheme with regions. (b) Step scheme with reflected and transmitted waves in corresponding regions.

We can write the solution of the problem (A.1) in each region α, β, and γ as

$$\begin{aligned}\phi^{\alpha}(x,z) &= \sum_n f_n^{\alpha}(x)\varphi_n^{\alpha}(z),\\ \phi^{\beta}(x,z) &= \sum_n f_n^{\beta}(x)\varphi_n^{\beta}(z),\\ \phi^{\gamma}(x,z) &= \sum_n f_n^{\gamma}(x)\varphi_n^{\gamma}(z),\end{aligned} \tag{A.2}$$

where f_n is a function along x direction and φ_n is a transverse function that forms a complete set of orthonormal basis

$$\int\limits_{-h}^{0} \varphi_n\varphi_m \mathrm{d}z = \delta_{nm}. \tag{A.3}$$

In order to derive the tranverse functions φ_n for all the regions α, β, and γ, we use the boundary conditions (A.1a) and (A.1b), which yields

$$\left.\frac{\partial\varphi_n}{\partial\mathbf{n}}\right|_{\Gamma} = 0, \quad \left.\frac{\partial\varphi_n}{\partial z}\right|_{z=0} = \frac{\omega^2}{g}\varphi_n, \tag{A.4}$$

and for every region separately it becomes

$$\begin{aligned}\left.\frac{\partial\varphi_n^{\alpha}}{\partial z}\right|_{z=h^+} &= 0, \quad \left.\frac{\partial\varphi_n^{\alpha}}{\partial z}\right|_{z=0} = \frac{\omega^2}{g}\varphi_n^{\alpha},\\ \left.\frac{\partial\varphi_n^{\beta}}{\partial z}\right|_{z=h^-} &= 0, \quad \left.\frac{\partial\varphi_n^{\beta}}{\partial z}\right|_{z=0} = \frac{\omega^2}{g}\varphi_n^{\beta},\\ \left.\frac{\partial\varphi_n^{\gamma}}{\partial z}\right|_{z=h^+} &= 0, \quad \left.\frac{\partial\varphi_n^{\gamma}}{\partial z}\right|_{z=0} = \frac{\omega^2}{g}\varphi_n^{\gamma}.\end{aligned} \tag{A.5}$$

The transverse functions satisfying the conditions (A.5) are

$$\begin{aligned}\varphi_n^{\alpha} &= N_n^{\alpha}\cosh(K_n^{\alpha}(z+h^+)),\\ \varphi_n^{\beta} &= N_n^{\beta}\cosh(K_n^{\beta}(z+h^-)),\\ \varphi_n^{\gamma} &= N_n^{\gamma}\cosh(K_n^{\gamma}(z+h^+)).\end{aligned} \tag{A.6}$$

The above normalized transverse functions adapted to the boundary conditions of the Neumann type at $z = h^-$ or $z = h^+$, and of the Robin type at $z = 0$ satisfy (A.5) with the dispersion relation of the water waves

$$\omega^2 = gK_n \tanh(K_n h). \tag{A.7}$$

In order to calculate the normalization factor N_n we use (A.3) for $n = m$

$$\int_{-h}^{0} \varphi_n^2 \mathrm{d}z = 1, \tag{A.8}$$

and substitute the transverse functions (A.6). It yields

$$\int_{-h}^{0} N_n^2 \cosh^2(K_n(z+h))\mathrm{d}z = 1. \tag{A.9}$$

Solving (A.9) we obtain

$$N_n = \sqrt{\frac{4K_n}{2K_n h + \sinh(2K_n h)}} = \left[\frac{h}{2}(\mathrm{sinhc}(2K_n h) + 1)\right]^{-\frac{1}{2}}. \tag{A.10}$$

Now we need to find f_n. To do it we use (A.1)

$$\triangle\left(\sum_n f_n(x)\varphi_n(x)\right) = 0. \tag{A.11}$$

After derivation

$$\frac{\partial^2 f_n}{\partial x^2}\varphi_n + f_n \frac{\partial^2 \varphi_n}{\partial z^2} = 0. \tag{A.12}$$

Taking into account (A.6) we know that

$$\frac{\partial^2 \varphi_n}{\partial z^2} = K_n^2 \varphi_n, \tag{A.13}$$

so (A.12) becomes

$$\frac{\partial^2 f_n}{\partial x^2} + K_n^2 f_n = 0, \tag{A.14}$$

whose solution is

$$f_n = A_n \mathrm{e}^{\mathrm{i}K_n x} + B_n \mathrm{e}^{-\mathrm{i}K_n x}. \tag{A.15}$$

Having derived the functions φ_n and f_n we are able to construct the form of the solution based on the assumption of reflected and transmitted waves (Fig. A.1b)

$$\begin{aligned}
\phi_\alpha(x,z) &= \mathrm{e}^{\mathrm{i}K_0^\alpha x}\varphi_0^\alpha(z) + \sum_n R_n \mathrm{e}^{-\mathrm{i}K_n^\alpha x}\varphi_n^\alpha(z),\\
\phi_\beta(x,z) &= \sum_n A_n \mathrm{e}^{\mathrm{i}K_n^\beta x}\varphi_n^\beta(z) + \sum_n B_n \mathrm{e}^{-\mathrm{i}K_n^\beta (x-\ell)}\varphi_n^\beta(z),\\
\phi_\gamma(x,z) &= \sum_n T_n \mathrm{e}^{\mathrm{i}K_n^\gamma (x-\ell)}\varphi_n^\gamma(z).
\end{aligned} \tag{A.16}$$

In order to calculate the unknowns R_n, A_n, B_n, and T_n we impose matching boundary conditions at the limits of the regions α, β, and γ where we want continuity of ϕ and $\partial\phi/\partial x$, i.e. at $x = 0$

$$\phi^\alpha(0,z) = \phi^\beta(0,z), \tag{A.17a}$$

$$\left.\frac{\partial\phi^\alpha}{\partial x}\right|_{x=0} = \left.\frac{\partial\phi^\beta}{\partial x}\right|_{x=0}, \tag{A.17b}$$

and at $x = \ell$

$$\phi^\beta(\ell,z) = \phi^\gamma(\ell,z), \tag{A.18a}$$

$$\left.\frac{\partial\phi^\beta}{\partial x}\right|_{x=\ell} = \left.\frac{\partial\phi^\gamma}{\partial x}\right|_{x=\ell}. \tag{A.18b}$$

Projecting (A.17a) on $z \in (-h^+, 0)$ at $x = 0$ we obtain (in region β)

$$\int\limits_{-h^-}^{0} \phi^\alpha \varphi_m^\alpha \mathrm{d}z = \int\limits_{-h^-}^{0} \phi^\beta \varphi_m^\beta \mathrm{d}z. \tag{A.19}$$

Substituting (A.16)

$$\int\limits_{-h^-}^{0} \varphi_0^\alpha \varphi_m^\beta \mathrm{d}z + \sum_n R_n \int\limits_{-h^-}^{0} \varphi_n^\alpha \varphi_m^\beta \mathrm{d}z = \sum_n A_n \int\limits_{-h^-}^{0} \varphi_n^\beta \varphi_m^\beta \mathrm{d}z + \sum_n B_n \mathrm{e}^{\mathrm{i}K_n^\beta \ell} \int\limits_{-h^-}^{0} \varphi_n^\beta \varphi_m^\beta \mathrm{d}z. \tag{A.20}$$

This approach is performed similarly to match (A.17b), (A.18a), (A.18b). Projecting (A.17b) on $z \in (-h^{+}, 0)$ at $x = 0$ we obtain (in region α)

$$\int_{-h^{+}}^{0} \frac{\partial \phi^{\alpha}}{\partial x} \varphi_{m}^{\alpha} \mathrm{d}z = \int_{-h^{-}}^{0} \frac{\partial \phi^{\beta}}{\partial x} \varphi_{m}^{\alpha} \mathrm{d}z. \tag{A.21}$$

Substituting (A.16)

$$\begin{aligned} K_{0}^{\alpha} \int_{-h^{-}}^{0} \varphi_{0}^{\alpha} \varphi_{m}^{\alpha} \mathrm{d}z - \sum_{n} K_{n}^{\alpha} R_{n} \int_{-h^{-}}^{0} \varphi_{n}^{\alpha} \varphi_{m}^{\alpha} \mathrm{d}z = \qquad\qquad (A.22)\\ = \sum_{n} K_{n}^{\beta} A_{n} \int_{-h^{-}}^{0} \varphi_{n}^{\beta} \varphi_{m}^{\alpha} \mathrm{d}z + \sum_{n} K_{n}^{\beta} B_{n} \mathrm{e}^{\mathrm{i} K_{n}^{\beta} \ell} \int_{-h^{-}}^{0} \varphi_{n}^{\beta} \varphi_{m}^{\alpha} \mathrm{d}z. \end{aligned}$$

Projecting (A.18a) on $z \in (-h^{+}, 0)$ at $x = \ell$ we obtain (in region β)

$$\int_{-h^{-}}^{0} \phi^{\beta} \varphi_{m}^{\beta} \mathrm{d}z = \int_{-h^{-}}^{0} \phi^{\gamma} \varphi_{m}^{\beta} \mathrm{d}z. \tag{A.23}$$

Substituting (A.16)

$$\sum_{n} A_{n} \mathrm{e}^{\mathrm{i} K_{n}^{\beta} \ell} \int_{-h^{-}}^{0} \varphi_{n}^{\beta} \varphi_{m}^{\beta} \mathrm{d}z + \sum_{n} B_{n} \int_{-h^{-}}^{0} \varphi_{n}^{\beta} \varphi_{m}^{\beta} \mathrm{d}z = \sum_{n} T_{n} \int_{-h^{-}}^{0} \varphi_{n}^{\gamma} \varphi_{m}^{\beta} \mathrm{d}z. \tag{A.24}$$

Projecting (A.18b) on $z \in (-h^{+}, 0)$ at $x = \ell$ we obtain (in region γ)

$$\int_{-h^{+}}^{0} \frac{\partial \phi^{\beta}}{\partial x} \varphi_{m}^{\gamma} \mathrm{d}z = \int_{-h^{-}}^{0} \frac{\partial \phi^{\gamma}}{\partial x} \varphi_{m}^{\gamma} \mathrm{d}z. \tag{A.25}$$

Substituting (A.16)

$$\sum_{n} K_{n}^{\beta} A_{n} \mathrm{e}^{\mathrm{i} K_{n}^{\beta} \ell} \int_{-h^{-}}^{0} \varphi_{n}^{\beta} \varphi_{m}^{\gamma} \mathrm{d}z - \sum_{n} K_{n}^{\beta} B_{n} \int_{-h^{-}}^{0} \varphi_{n}^{\beta} \varphi_{m}^{\gamma} \mathrm{d}z = \sum_{n} K_{n}^{\gamma} T_{n} \int_{-h^{-}}^{0} \varphi_{n}^{\gamma} \varphi_{m}^{\gamma} \mathrm{d}z. \tag{A.26}$$

Knowing that $K_{n}^{\alpha} = K_{n}^{\gamma}$, therefore $\varphi_{n}^{\alpha} = \varphi_{n}^{\gamma}$, remembering that (A.3) and defining

$$C_{nm} \triangleq \int_{-h^{-}}^{0} \varphi_{n}^{\alpha} \varphi_{m}^{\beta} \mathrm{d}z, \tag{A.27}$$

we can write the matching conditions (A.20), (A.22), (A.24), and (A.26) as

$$\begin{aligned} C_{0m} + \sum_n R_n C_{nm} &= \sum_N A_n \delta_{nm} + \sum_n B_n \mathrm{e}^{\mathrm{i}K_n^\beta \ell}\delta_{nm}, \\ K_0^\alpha \delta_{0m} - \sum_n K_n^\alpha R_n \delta_{nm} &= \sum_n K_n^\beta A_n C_{mn} - \sum_n K_n^\alpha B_n C_{mn}, \\ \sum_n A_n \mathrm{e}^{\mathrm{i}K_n^\beta \ell}\delta_{nm} + \sum_n B_n \delta_{nm} &= \sum_n T_n C_{nm}, \\ \sum K_n^\alpha A_n \mathrm{e}^{\mathrm{i}K_n^\beta \ell} C_{mn} - \sum_n K_n^\beta C_{mn} &= \sum_n K_n^\alpha T_n \delta_{nm}. \end{aligned}$$

or in a matrix form

$$\begin{bmatrix} -\mathbf{C} & \mathbf{I} & \mathrm{e}^{\mathrm{i}K_n^\beta \ell}\mathbf{I} & \mathbf{0} \\ K_n^\alpha \mathbf{I} & K_n^\beta \mathbf{C}^T & -K_n^\beta \mathrm{e}^{\mathrm{i}K_n^\beta \ell}\mathbf{C}^T & \mathbf{0} \\ \mathbf{0} & \mathrm{e}^{\mathrm{i}K_n^\beta \ell}\mathbf{I} & \mathbf{I} & -\mathbf{C} \\ \mathbf{0} & K_n^\beta \mathrm{e}^{\mathrm{i}K_n^\beta \ell}\mathbf{C}^T & -K_n^\beta \mathbf{C}^T & -K_n^\alpha \mathbf{I} \end{bmatrix} \begin{bmatrix} R_n \\ A_n \\ B_n \\ T_n \end{bmatrix} = \begin{bmatrix} C_{0m} \\ K_0^\alpha \delta_{0m} \\ \mathbf{0} \\ \mathbf{0} \end{bmatrix} \qquad (A.28)$$

The sought coefficients R_n, A_n, B_n, and T_n can be now calculated and inserted into (A.16) to obtain the potential ϕ necessary to determine the parameter h_x (3.15).

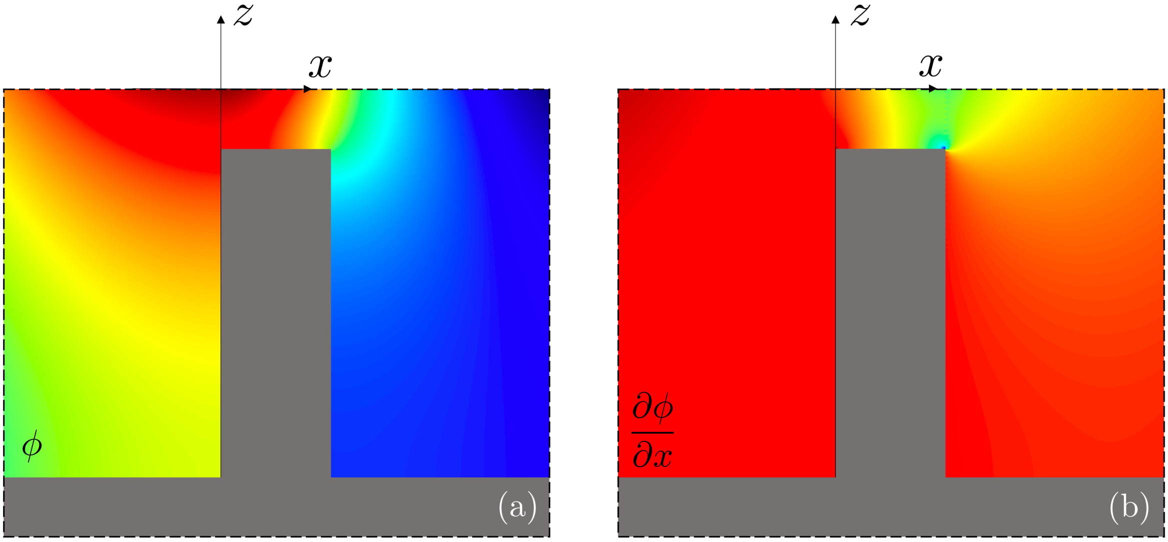

Fig. A.2 (a) Example of the solution to (A.28) for the velocity potential ϕ (A.16). (b) Correspoding horizontal velocity $\partial\phi/\partial x$, whose integral provides h_x (3.15)

Appendix B

Article: Regular sloshing modes in irregular cavities using metabathymetry

Regular sloshing modes in irregular cavities using metabathymetry

Adam Anglart,[1,*] Agnès Maurel,[2] Philippe Petitjeans,[1] and Vincent Pagneux[3]
[1]*Sorbonne Université, Université PSL, ESPCI PMMH,*
Institut Langevin, 1 rue Jussieu, 75005 Paris, France
[2]*Institut Langevin, ESPCI, 1 rue Jussieu, 75005 Paris, France*
[3]*Laboratoire d'Acoustique de l'Université du Maine,*
Avenue Olivier Messiaen, 72085 Le Mans, France

We demonstrate experimentally and numerically that metamaterials can be used to control water wave propagation and resonance properties of a closed cavity, including cloaking of its eigenmodes. The anisotropic medium, designed using coordinate transformation theory and the homogenization of a fully three-dimensional linear water wave problem, consists of bathymetry with a layered structure at a subwavelength scale. Three cavities with bending angles of 15°, 30°, and 45° were tested and compared to a reference case with flat bathymetry. Fourier Transform Profilometry, as well as confocal displacement sensors, are used for space-time resolved measurements of a water surface deformation. Experimental data show the capability of water-wave metamaterials to provide a robust anisotropic medium for wave propagation.

The concept of designing materials that exhibit peculiar behavior, which cannot be commonly found in nature, has always been attracting the attention of the scientific and engineering community. Metamaterials, originally used in electromagnetism, during the last two decades [1, 2] have been of a substantial interest in controlling acoustic [3–7], elastic [8–11], and seismic waves [12–16]. They have also been employed to control water wave propagation, for which some of the applications include cloaking [17, 18], focusing [19], or guiding the energy flow [20]. As a result, metamaterials can be beneficial for coastal engineering when it comes to wave-free zones, shore protection, energy harvesting, or designing wake-less watercraft. Less attention has been devoted to sloshing dynamics, where resonance properties of a cavity strongly depend on its geometry yielding phenomena such as high spots [21, 22]. Mathematical approaches to metamaterial design vary significantly throughout the disciplines and the category of waves it serves. In this paper we benefit from the coordinate transformation theory [23, 24] and the homogenization of fully three-dimensional water wave problem [25, 26]. First, we take into account the coordinate transformation theory (CTT), which is of great use with regard to water waves. However, it has not been used yet in the context of cavity resonance and eigenmodes cloaking (Fig. 1), which we study in this paper experimentally (Fig. 3). Although the dispersion, being an inherent property of water waves, makes the CTT unavailable, we stay close to a shallow water regime and consider our system dispersionless. This fact allows to use of the 2D shallow water equation (2D SWE).

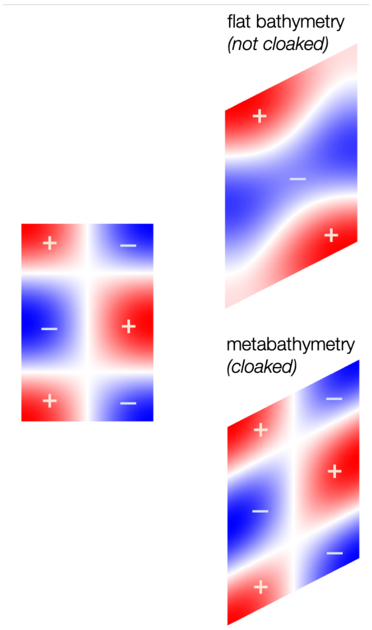

FIG. 1: Example of an eigenmode in a regular cavity (left) and in an irregular, shifted, cavity (right) without cloaking for flat bathymetry and with cloaking thanks to a metabathymetry.

We start with the two-dimensional shallow-water equation (2D SWE) in a virtual space (X, Y)

$$\begin{aligned} \nabla_{XY} \cdot (h_0 \nabla_{XY} \eta) + \frac{\omega^2}{g} \eta = 0, \\ \nabla_{XY} \eta \cdot \mathbf{n} = 0 \text{ on } \partial\Omega, \end{aligned} \tag{1}$$

where h_0 is the reference water depth, η stands for the vertical displacement of a free surface, ω is the angular frequency, g denotes the gravitational acceleration, $\partial\Omega$ is the boundary, and $\mathbf{n}$ identifies the vector normal to it and $\nabla_{XY} = (\partial/\partial X, \partial/\partial Y)^T$. We assume shallow water limit ($kh_0 \ll 1$), where the wavenumber k is given through the dispersion relation $\omega^2 = gh_0k^2$. Now, applying geometrical transformation from virtual (X, Y) to

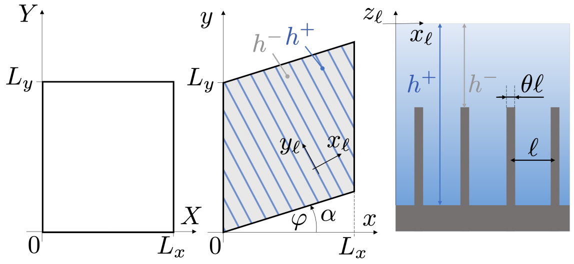

(a) (b) (c)

FIG. 2: The cavity in virtual space (X, Y) (a) and in the real space (x, y) with bending angle φ (b). In (b) we show the top view of the metabathymetry realizing the anisotropy, an array of layers inclined by an angle α and in (c) the side view.

real (x, y) space, e.g., by using the variational formulation of the problem, we obtain

$$\nabla \cdot \left(\frac{\mathbf{J} h_0 \mathbf{J}^T}{\det \mathbf{J}} \nabla \eta \right) + \frac{\omega^2}{g \det \mathbf{J}} \eta = 0,$$
$$\mathbf{n} \cdot \left(\frac{\mathbf{J} h_0 \mathbf{J}^T}{\det \mathbf{J}} \nabla \eta \right) = 0 \text{ on } \partial\Omega, \tag{2}$$

where $\mathbf{J}$ stands for the Jacobian matrix of the tranformation, and now $\nabla = (\partial/\partial x, \partial/\partial y)^T$. The 2D SWE preserves its form, i.e., is of Helmholtz type. Due to the fact that g is not tunable in conventional conditions, we need a volume preserving (nonmagnetic) transformation ($\det \mathbf{J} = 1$). We choose a simple shear deformation of the cavity, which leads to the change of coordinates $x = X$, $y = \tan\varphi X + Y$, and whose Jacobian matrix

$$\mathbf{J} = \begin{bmatrix} 1 & 0 \\ \tan\varphi & 1 \end{bmatrix}. \tag{3}$$

By changing the coordinates (Fig. 2), the anisotropy is introduced (2) and has to be realized in practice. To do so, we insert a particularly oriented anisotropic medium (with an angle α) with different effective water depths in x and y directions, i.e., h_x and h_y. We obtain

$$\nabla \cdot \left(\mathbf{R}_\alpha \mathbf{h} \mathbf{R}_\alpha^T \nabla \eta \right) + \frac{\omega^2}{g} \eta = 0, \quad \text{where } \mathbf{h} = \begin{bmatrix} h_x & 0 \\ 0 & h_y \end{bmatrix}, \tag{4}$$

and $\mathbf{R}_\alpha$ is the conventional rotation matrix with a rotation through an angle α with respect to x axis (Fig. 2(b)). Now, by identifying (2) and (4), and having in mind the geometry of the cavity (3), we obtain explicit formulae for the water depths h_x, h_y and the rotation angle α as the functions of bending angle φ and the reference water depth h_0. Hence, the depts h_x and h_y are the roots of $h^2 - (2 + \tan^2\varphi) h_0 h + h_0^2 = 0$, where $h_x > h_y$ and $\tan 2\alpha = -2/\tan\varphi$ (note a misprint in [20]).

It has been shown that the effective anisotropy, being the result of the presence of the metabathymetry, cannot be inferred from the shallow water equation even in the shallow water regime, as 3D effects affect the flow over a rapidly varying bathymetry due to the strong effect of the evanescent field [25–27]. Thus, the modeling, which predicts that the effective water depth tensor is related to the arithmetic and geometric averages of the actual water depths

$$h_x = \langle h^{-1} \rangle^{-1}, \quad h_y = \langle h \rangle, \tag{5}$$

underestimates the degree of the anisotropy due to the metabathymetry ($\langle h \rangle = \theta h^- + (1-\theta) h^+$, where θ is the filling fraction of the layers, Fig. 2). To properly model the aforementioned effects, the homogenization of the full 3D linear water wave problem must be used. Considering harmonic regime with time dependence $e^{i\omega t}$, assuming that the fluid is inviscid and incompressible, and knowing that the flow is irrotational, the velocity potential $\phi(x_\ell, y_\ell, z_\ell)$ satisfies

$$\triangle \phi = 0,$$
$$\frac{\partial \phi}{\partial z_l} = \frac{\omega^2}{g} \phi \text{ at } z_l = 0,$$
$$\mathbf{n} \cdot \nabla \phi = 0 \text{ on } \Gamma, \tag{6}$$

where Γ is the nonflat bottom, $\mathbf{n}$ is the vector normal to it, and $z_l = 0$ corresponds to the unperturbed free surface.

As shown in [25, 27], the effective water depths h_x and h_y derived from a fully three dimensional problem (6) are of the form

$$h_x = \ell \int_Y \frac{\partial \Phi}{\partial x_r} \mathrm{d}Y, \quad h_y = \langle h \rangle, \tag{7}$$

where Φ stands for the potential satisfied in the unit cell Y, ℓ is the periodicity of the metabathymetry, Y denotes a unit cell of the metabathymetry, and $x_r = x_l/\ell$ [25]. Comparing (5) to (7), it comes into view that only h_x is affected by 3D near field effects. It has been shown that h_x in (7) might be much smaller than $\langle h^{-1} \rangle^{-1}$ predicted by 2D approach. As a consequence, the resulting

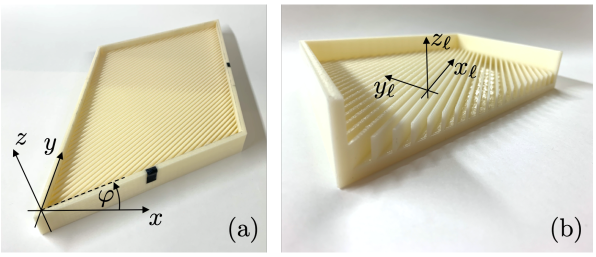

FIG. 3: (a) Metamaterial cavity used in the experiments. The view from above with a coordinate system in real space (x, y, z). (b) Section view with a local coordinate system used for metabathymetry design (x_ℓ, y_ℓ, z_ℓ).

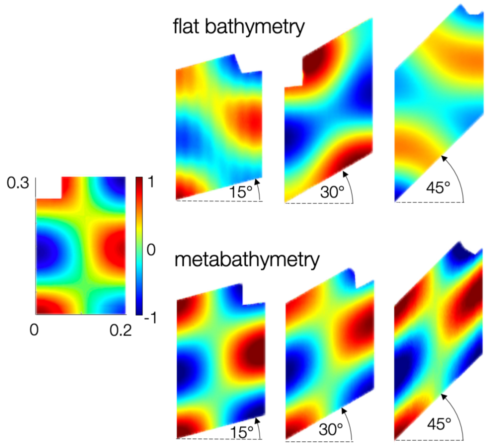

FIG. 4: Experimental FTP measurements of the free surface elevation of the fifth eigenmode $\tilde{\eta}(x, y, \omega)$ for bending angles $\varphi = 15°$, $30°$ and $45°$ for the flat bathymetry and for the metabathymetry. The reference cavity for $\varphi = 0°$ is shown on the left panel.

anisotropy can be much larger than the one predicted by the classical homogenization of layered media. Now, we use the homogenization theory (7) that allows to calculate real water depths $\mathbf{h}^{\pm} = [h^{+}\ h^{-}]^{T}$. However, this approach needs already preset values of the real geometry. That is why we use optimization routine for obtaining $\mathbf{h}^{\pm}$: $\min_{\mathbf{h}^{\pm}\in\mathbb{R}^2} \left|\left|f(\ell, \theta, h^{+}, h^{-}) - [h_x\ h_y]^{T}\right|\right|$, subject to $h^{+} - h^{-} \geq 0$, where $f(\ell, \theta, h^{+}, h^{-})$ is a function whose output are the values of h_x and h_y [25]. The periodicity ℓ and the filling fraction θ are constant.

Three metamaterial cavities with bending angles $\varphi_1 = 15°$, $\varphi_2 = 30°$ and $\varphi_3 = 45°$ were designed and manufactured using a 3D printer. Three reference cavities with flat bathymetry and of the same deviation angles φ_1, φ_2 and φ_3 were also built. The dimensions of cavities were constant and set as $L_x = 200\,\mathrm{mm}$ and $L_y = 300\,\mathrm{mm}$, which allowed to preserve the same volume throughout the set of cavities. The reference water depth was chosen as $h_0 = 10\,\mathrm{mm}$ as a trade-off between staying close to shallow-water regime and undesirable attenuation caused by a bottom friction for small water depths. For each of three systems we calculate the parameters h_x, h_y, h^{+}, h^{-} and α based on the routine presented before and are summarised in Table I. Considering wavemaker constraints ($h^{-} \geq 3\,\mathrm{mm}$) and rigidity limitations of the 3D printed structure ($\theta\ell \geq 1\,\mathrm{mm}$) we chose $\theta = 0.2$ and $\ell = 5\,\mathrm{mm}$.

The wave generator (point source) excites a system with a chirp signal whose frequency spectrum ranges from 0.3 Hz to 1.5 Hz. This range allows to recover the first five eigenmodes of the cavity. The partially immerged point source, creating a circular, linear wave, is placed in one of the corners of the cavity. The corner is chosen based on the shape of the eigenmodes so that it can be excited in the cavity. Occasionally the position of the source has to be changed since placing it in the node of the eigenmode would make it unfeasible to recover. The region where the wavemaker is placed is sufficiently cut out from the measurements so that the near-field effects are negligible.

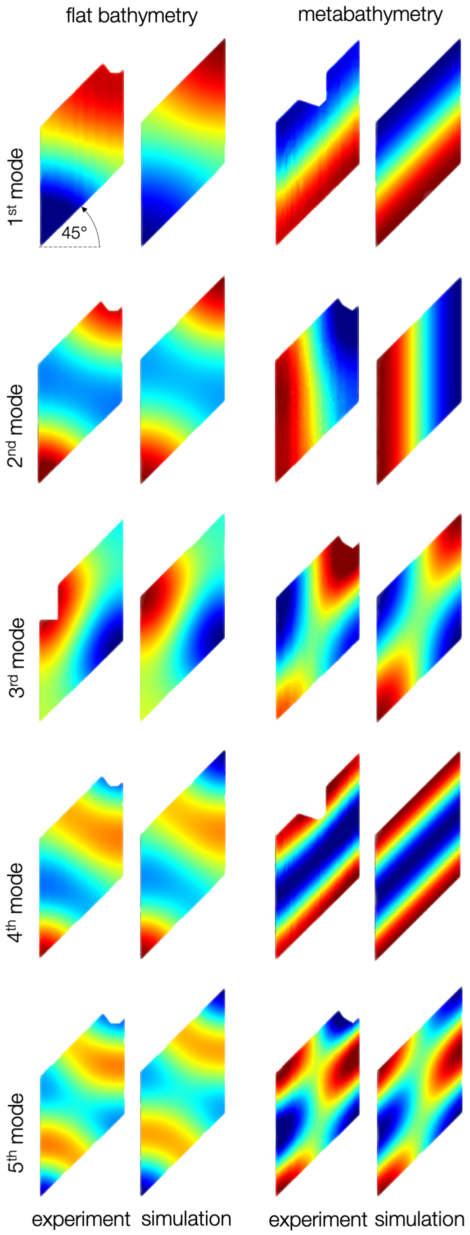

FIG. 5: First 5 eigenmodes for $\varphi = 45°$ – Wavefields $\tilde{\eta}(x, y, \omega)$ from FTP measurements and from direct numerics, for the metabathymetry and for the flat bottom.

In order to quantify the wavefield, we use the Fourier

Transform Profilometry (FTP) technique [28] as well as confocal displacement sensors (2 lasers Keyence CL-P070). FTP is a technique that uses a fringe pattern projection on a measured surface. In our case, the water is painted with titanium dioxide (TiO_2) so that its surface becomes diffusive and ready for a fringe projection, whereas the change of physical properties of the painted water, including viscosity, is insignificant [29]. A high-resolution video projector EPSON EH-TW9200W is used to project the fringe pattern, and a high-speed camera Photron FASTCAM Mini WX100 records the deformation of the surface with an accuracy of more than 0.1 mm. Confocal displacement sensors allow us to measure the amplitude of the wave in the maxima of eigenmodes with much higher accuracy than FTP and with pure, transparent water confirming the results of the FTP technique. Using these methods, we obtain the space-time resolved measurements $\eta(x, y, t)$ that are later transformed into the frequency domain, resulting in the complex wavefield $\tilde{\eta}(x, y, \omega)$, to extract eigenfrequencies and eigenmodes. The selection of eigenfrequencies from the experiments is done by finding the local maxima of $|\tilde{\eta}(x, y, \omega)|$ averaged in space. Then, the eigenmodes are chosen as the real part of $\tilde{\eta}(x, y, \omega)$ at the given eigenfrequency and some of them are presented in Fig. 4 and Fig. 5.

The real part of the wavefield for the fifth eigenmode, i.e., the one whose frequency is the highest in the set of the measurements, is presented in Fig. 4 for rectangular reference cavity and the cavities with the bending angles φ of 0°, 15°, 30° and 45°. In the reference cavities without the metabathymetry the effect of the difference in geometry is clearly visible. The eigenmodes change their shape significantly with respect to the angle φ. The change in the position of nodes and maxima is easily noticeable. Introducing metabathymetry has an anticipated consequence. The eigenmode pattern remains the same throughout the measurements, even for the highest angle $\varphi = 45°$. It is worth mentioning that in this case, i.e., the mode with the highest frequency and the highest bending angle, the pattern remains the same, even though the shallow water approximation here is questionable ($h^+ = 31.92\,\text{mm}$) and the friction of the metamaterial structure becomes more and more significant ($h^- = 3.23\,\text{mm}$). This manifests a significant improvement and the benefit of using the homogenization of a fully three-dimensional linear water wave problem in comparison to previous works where 2D homogenization was used [20].

TABLE I: Cavities dimensions and design parameters.

φ [°]	15	30	45
α [°]	-41.18	-36.95	-31.72
h_x [mm]	7.66	5.66	3.82
h_y [mm]	13.06	17.68	26.18
h^+ [mm]	14.56	20.83	31.92
h^- [mm]	7.07	5.07	3.23

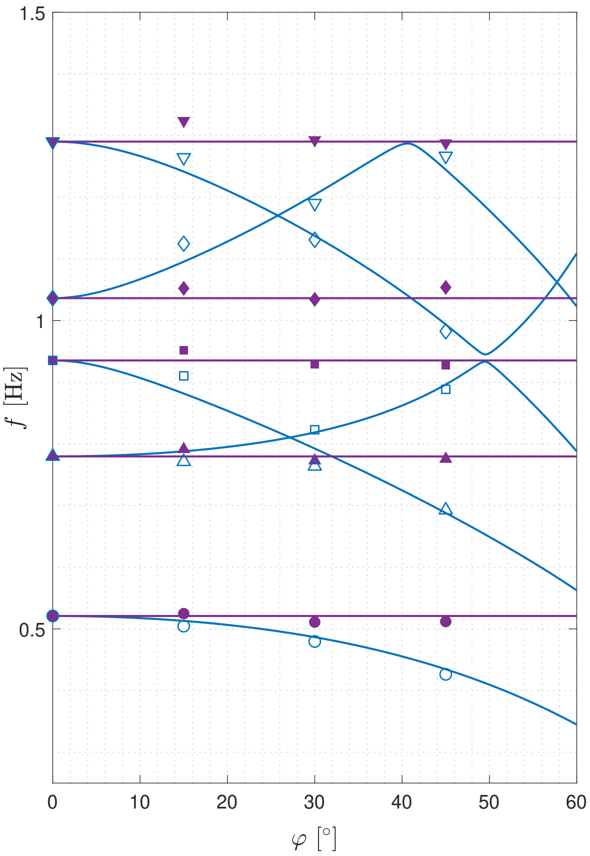

FIG. 6: Experimental (symbols) and numerical (plain lines) values of the eigenfrequencies as a function of the bending angle φ. Results are shown for the anisotropic bathymetry (purple) and for the flat bathymetry (blue).

All the five eigenmodes recovered in this experiment for the highest angle $\varphi = 45°$ are reported in Fig. 5. The higher modes were difficult to achieve for several reasons. First of all, as frequency increases, the eigenvalues become closer to each other, including degenerate cases, and are problematic if not impossible to distinguish experimentally. Moreover, when it comes to higher frequencies, dispersion and dissipation play a significant role in the water wave experiments, questioning the shallowness of the system and measurement techniques capacities, as the amplitude of the wave becomes extremely small. Please note that increasing the amplitude and the frequency of a water wave in our system would result in a nonlinear problem, which we do not study in this paper.

Comparing the experimental results with the numerical prediction obtained by solving (4) using the Finite Element Method, we observe an excellent agreement of the eigenmodes. In order to quantitatively describe the difference between them, we introduce a pattern error defined as $\epsilon_P \equiv \int_A |\eta_S(x,y,\omega) - \hat{\eta}(x,y,\omega)|^2 \,\mathrm{d}A / \int_A |\eta_S(x,y,\omega)|^2 \,\mathrm{d}A$, where η_S is the normalized wavefield predicted numerically, $\hat{\eta}$ denotes the normalized wavefield measured in the experiments, and A is the area of the cavity. The normalization is accomplished by rescaling the wavefield amplitude so that it satisfies the following condition $\int_A |\eta(x,y,\omega)|^2 \,\mathrm{d}A = 1$. The error increases both with the increasing angle φ and the frequency ω. However, in all of the cases, it does not exceed $\epsilon_P = 5.2\%$. The summary of all the experimental values of the eigenfrequencies compared to the numerical predictions is shown in Fig. 6. The horizontal axis represents the angle of the cavity deformation φ and the vertical axis - the frequency f. Consecutive lines correspond to the eigenvalues of the cavity with a bending angle φ. It can be seen that the use of the metabathymetry allows to have a constant value of eigenfrequencies (pink dots), hence meeting our goal and preserving the resonance properties of the deformed cavities as predicted with coordinate transformation theory. The efficiency of the metabathymetry is quantified by the eigenfrequency error defined as $\epsilon_F = |f_S - f|/|f_S|$, where f_S is the predicted eigenfrequency, and f stands for the eigenfrequency measured using confocal displacement sensors. This error is always smaller than the pattern error ϵ_P, and its value varies from 1.4% to 3.1%. The metabathymetry allows to recover the properties of a regular cavity in a shifted geometry. The example of one of the eigenmodes is reported in Fig. 4 for different angles φ. We are also able to maintain the same set of eigenfrequencies for the cavities with changed geometry (Fig. 6). The presented experiments show the robustness of the homogenization of the three-dimensional water wave problem and the coordinate transformation theory in designing metamaterials for water waves. The designed metabathymetry can be used for the control of water cavity resonance and the propagation of the wave inside of it. The efficiency of the anisotropic medium is shown using space-time resolved measurements of the full water wavefield. Very good agreement with numerical prediction is achieved.

---

[*] Electronic address: adam.anglart@espci.fr

[1] N. Engheta and R. W. Ziolkowski, *Metamaterials: Physics and Engineering Explorations* (Wiley-IEEE Press, 2006).

[2] T. J. Cui, D. R. Smith, and R. Liu, *Metamaterials: Theory, Design and Applications* (Springer, 2010).

[3] V. Achilleos, G. Theocharis, O. Richoux, and V. Pagneux, Physical Review B **95**, 144303 (2017).

[4] C. Faure, O. Richoux, S. Félix, and V. Pagneux, Applied Physics Letters **108**, 064103 (2016).

[5] S.-W. Fan, S.-D. Zhao, L. Cao, Y. Zhu, A.-L. Chen, Y.-F. Wang, K. Donda, Y.-S. Wang, and B. Assouar, Physical Review B **101**, 024104 (2020).

[6] G. Ma and P. Sheng, Science Advances **2**, e1501595 (2016).

[7] S. Qi, M. Oudich, Y. Li, and B. Assouar, Applied Physics Letters **108**, 263501 (2016).

[8] H. Nassar, H. Chen, A. Norris, M. Haberman, and G. Huang, Proceedings of the Royal Society A: Mathematical, Physical and Engineering Sciences **473**, 20170188 (2017).

[9] H.-W. Dong, S.-D. Zhao, Y.-S. Wang, and C. Zhang, Journal of the Mechanics and Physics of Solids **105**, 54 (2017).

[10] G. Trainiti, Y. Xia, J. Marconi, G. Cazzulani, A. Erturk, and M. Ruzzene, Physical Review Letters **122**, 124301 (2019).

[11] X. Xu, C. Wang, W. Shou, Z. Du, Y. Chen, B. Li, W. Matusik, N. Hussein, and G. Huang, Physical Review Letters **124**, 114301 (2020).

[12] A. Colombi, D. Colquitt, P. Roux, S. Guenneau, and R. V. Craster, Scientific Reports **6**, 1 (2016).

[13] M. Miniaci, A. Krushynska, F. Bosia, and N. M. Pugno, New Journal of Physics **18**, 083041 (2016).

[14] Y. Achaoui, T. Antonakakis, S. Brûlé, R. Craster, S. Enoch, and S. Guenneau, New Journal of Physics **19**, 063022 (2017).

[15] A. Maurel, J.-J. Marigo, K. Pham, and S. Guenneau, Physical Review B **98**, 134311 (2018).

[16] K. Pham, A. Maurel, S. Félix, and S. Guenneau, Materials **13**, 1632 (2020).

[17] J. Newman, European Journal of Mechanics-B/fluids **47**, 145 (2014).

[18] T. Bobinski, A. Maurel, P. Petitjeans, and V. Pagneux, Journal of Fluid Mechanics **845**, R4 (2018).

[19] T. Bobinski, A. Eddi, P. Petitjeans, A. Maurel, and V. Pagneux, Applied Physics Letters **107**, 014101 (2015).

[20] C. Berraquero, A. Maurel, P. Petitjeans, and V. Pagneux, Physical review E **88**, 051002 (2013).

[21] T. Kulczycki and N. Kuznetsov, Proceedings of the Royal Society A: Mathematical, Physical and Engineering Sciences **467**, 1491 (2011).

[22] T. Kulczycki, M. Kwaśnicki, and B. Siudeja, Journal of Engineering Mathematics **99**, 157 (2016).

[23] J. B. Pendry, D. Schurig, and D. R. Smith, science **312**, 1780 (2006).

[24] U. Leonhardt and T. G. Philbin, in *Progress in Optics* (Elsevier, 2009), vol. 53, pp. 69–152.

[25] A. Maurel, J. J. Marigo, P. Cobelli, P. Petitjeans, and V. Pagneux, Physical Review B **96**, 1 (2017), ISSN 24699969.

[26] A. Bensoussan, J.-L. Lions, and G. Papanicolaou, *Asymptotic analysis for periodic structures*, vol. 374 (American Mathematical Soc., 2011).

[27] R. R. Rosales and G. C. Papanicolaou, Studies in Applied Mathematics **68**, 89 (1983).

[28] P. J. Cobelli, A. Maurel, V. Pagneux, and P. Petitjeans, Experiments in fluids **46**, 1037 (2009).

[29] A. Przadka, B. Cabane, V. Pagneux, A. Maurel, and P. Petitjeans, Experiments in Fluids **52**, 519 (2012), ISSN 07234864.

References

[1] J. da Silva, “Satellite imagery shows alernating dark and light bands of smooth and rough waters formed at the ocean surface by an internal wave propagating deeper in the depths. The internal wave is rippling into Cape Cod Bay between the tip of Cape Cod and Stellwagen Bank, a shallow underwater bank to the north.”, Dec 2014.

[2] E. H. T. Collaboration *et al.*, “First M87 event horizon telescope results. I. The shadow of the supermassive black hole”, *arXiv preprint arXiv:1906.11238*, 2019.

[3] J. Oeffner and G. V. Lauder, “The hydrodynamic function of shark skin and two biomimetic applications”, *Journal of Experimental Biology*, vol. 215, no. 5, pp. 785–795, 2012.

[4] L. Plattner, “Optical properties of the scales of Morpho rhetenor butterflies: theoretical and experimental investigation of the back-scattering of light in the visible spectrum”, *Journal of the Royal Society Interface*, vol. 1, no. 1, pp. 49–59, 2004.

[5] P. Vukusic, J. Sambles, C. Lawrence, and R. Wootton, “Quantified interference and diffraction in single Morpho butterfly scales”, *Proceedings of the Royal Society of London. Series B: Biological Sciences*, vol. 266, no. 1427, pp. 1403–1411, 1999.

[6] J. A. Morris, *Application of shark skin flow control techniques to airflow.* The University of Alabama, 2017.

[7] V. G. Veselago, “Electrodynamics of substances with simultaneously negative values of ϵ and μ”, *Soviet Physics Uspekhi*, vol. 10, no. 4, pp. 504–509, 1968.

[8] J. B. Pendry, “Negative refraction makes a perfect lens”, *Physical Review Letters*, vol. 85, no. 18, p. 3966, 2000.

[9] J. B. Pendry, D. Schurig, and D. R. Smith, “Controlling electromagnetic fields”, *Science*, vol. 312, no. 5781, pp. 1780–1782, 2006.

[10] U. Leonhardt, “Optical conformal mapping”, *Science*, vol. 312, no. 5781, pp. 1777–1780, 2006.

[11] N. Engheta and R. W. Ziolkowski, *Metamaterials: Physics and Engineering Explorations.* Wiley-IEEE Press, 2006.

[12] T. J. Cui, D. R. Smith, and R. Liu, *Metamaterials: Theory, Design and Applications.* Springer, 2010.

[13] V. Achilleos, G. Theocharis, O. Richoux, and V. Pagneux, “Non-hermitian acoustic metamaterials: Role of exceptional points in sound absorption”, *Physical Review B*, vol. 95, no. 14, p. 144303, 2017.

[14] C. Faure, O. Richoux, S. Félix, and V. Pagneux, “Experiments on metasurface carpet cloaking for audible acoustics”, *Applied Physics Letters*, vol. 108, no. 6, p. 064103, 2016.

[15] S.-W. Fan, S.-D. Zhao, L. Cao, Y. Zhu, A.-L. Chen, Y.-F. Wang, K. Donda, Y.-S. Wang, and B. Assouar, “Reconfigurable curved metasurface for acoustic cloaking and illusion”, *Physical Review B*, vol. 101, no. 2, p. 024104, 2020.

[16] G. Ma and P. Sheng, “Acoustic metamaterials: From local resonances to broad horizons”, *Science Advances*, vol. 2, no. 2, p. e1501595, 2016.

[17] S. Qi, M. Oudich, Y. Li, and B. Assouar, “Acoustic energy harvesting based on a planar acoustic metamaterial”, *Applied Physics Letters*, vol. 108, no. 26, p. 263501, 2016.

[18] H. Nassar, H. Chen, A. Norris, M. Haberman, and G. Huang, “Non-reciprocal wave propagation in modulated elastic metamaterials”, *Proceedings of the Royal Society A: Mathematical, Physical and Engineering Sciences*, vol. 473, no. 2202, p. 20170188, 2017.

[19] H.-W. Dong, S.-D. Zhao, Y.-S. Wang, and C. Zhang, “Topology optimization of anisotropic broadband double-negative elastic metamaterials”, *Journal of the Mechanics and Physics of Solids*, vol. 105, pp. 54–80, 2017.

[20] G. Trainiti, Y. Xia, J. Marconi, G. Cazzulani, A. Erturk, and M. Ruzzene, “Time-periodic stiffness modulation in elastic metamaterials for selective wave filtering: theory and experiment”, *Physical Review Letters*, vol. 122, no. 12, p. 124301, 2019.

[21] X. Xu, C. Wang, W. Shou, Z. Du, Y. Chen, B. Li, W. Matusik, N. Hussein, and G. Huang, “Physical realization of elastic cloaking with a polar material”, *Physical Review Letters*, vol. 124, no. 11, p. 114301, 2020.

[22] A. Colombi, D. Colquitt, P. Roux, S. Guenneau, and R. V. Craster, “A seismic metamaterial: The resonant metawedge”, *Scientific Reports*, vol. 6, no. 1, pp. 1–6, 2016.

[23] M. Miniaci, A. Krushynska, F. Bosia, and N. M. Pugno, “Large scale mechanical metamaterials as seismic shields”, *New Journal of Physics*, vol. 18, no. 8, p. 083041, 2016.

[24] Y. Achaoui, T. Antonakakis, S. Brûlé, R. Craster, S. Enoch, and S. Guenneau, “Clamped seismic metamaterials: ultra-low frequency stop bands”, *New Journal of Physics*, vol. 19, no. 6, p. 063022, 2017.

[25] A. Maurel, J.-J. Marigo, K. Pham, and S. Guenneau, “Conversion of Love waves in a forest of trees”, *Physical Review B*, vol. 98, no. 13, p. 134311, 2018.

[26] K. Pham, A. Maurel, S. Félix, and S. Guenneau, “Hybridized Love waves in a guiding layer supporting an array of plates with decorative endings”, *Materials*, vol. 13, no. 7, p. 1632, 2020.

[27] J. Newman, “Cloaking a circular cylinder in water waves”, *European Journal of Mechanics-B/fluids*, vol. 47, pp. 145–150, 2014.

[28] T. Bobinski, A. Maurel, P. Petitjeans, and V. Pagneux, “Backscattering reduction for resonating obstacle in water-wave channel”, *Journal of Fluid Mechanics*, vol. 845, p. R4, 2018.

[29] M. Farhat, S. Enoch, S. Guenneau, and A. B. Movchan, “Broadband cylindrical acoustic cloak for linear surface waves in a fluid”, *Physical Review Letters*, vol. 101, p. 134501, Sep 2008.

[30] R. Porter, “Cloaking in water waves”, *Handbook of Metamaterials Properties*, vol. 2, 2017.

[31] T. Bobinski, A. Eddi, P. Petitjeans, A. Maurel, and V. Pagneux, “Experimental demonstration of epsilon-near-zero water waves focusing”, *Applied Physics Letters*, vol. 107, no. 1, p. 014101, 2015.

[32] C. Berraquero, A. Maurel, P. Petitjeans, and V. Pagneux, “Experimental realization of a water-wave metamaterial shifter”, *Physical Review E*, vol. 88, no. 5, p. 051002, 2013.

[33] G. Dupont, O. Kimmoun, B. Molin, S. Guenneau, and S. Enoch, “Numerical and experimental study of an invisibility carpet in a water channel”, *Physical Review E*, vol. 91, no. 2, p. 023010, 2015.

[34] N. S. Bakhvalov and G. Panasenko, *Homogenisation: averaging processes in periodic media: mathematical problems in the mechanics of composite materials*, vol. 36. Springer Science & Business Media, 2012.

[35] E. Sanchez-Palencia and A. Zaoui, “Homogenization techniques for composite media”, *CISM International Centre for Mechanical Sciences, Courses and Lectures*, vol. 272, 1987.

[36] A. Bensoussan, J.-L. Lions, and G. Papanicolaou, *Asymptotic analysis for periodic structures*, vol. 374. American Mathematical Soc., 2011.

[37] L. Tartar, *The general theory of homogenization: a personalized introduction*, vol. 7. Springer Science & Business Media, 2009.

[38] R. Porter, “Plate arrays as a water wave metamaterial”, in *33rd International Workshop on Water Waves and Floating Bodies, Guidel-Plages, France*, pp. 1–4, 2018.

[39] R. Porter, “Plate arrays as a perfectly-transmitting negative-refraction metamaterial”, *Wave Motion*, vol. 100, p. 102673, 2021.

[40] C. Yi, Y. J. Yoo, Y. Kim, W. Kim, Y. Lee, and J. Rhee, “Role of Wood’s anomaly in the performance of metamaterial absorbers with periodicity comparable to wavelength”, *Journal of Physics D: Applied Physics*, vol. 49, p. 195103, 05 2016.

[41] M. Rybin, D. Filonov, K. Samusev, P. Belov, Y. Kivshar, and M. Limonov, “Phase diagram for the transition from photonic crystals to dielectric metamaterials”, *Nature Communications*, vol. 6, 07 2015.

[42] J. K. Asbóth, L. Oroszlány, and A. Pályi, “A short course on topological insulators”, *Lecture notes in physics*, vol. 919, p. 166, 2016.

[43] M. Z. Hasan and C. L. Kane, “Colloquium: topological insulators”, *Reviews of Modern Physics*, vol. 82, no. 4, p. 3045, 2010.

[44] A. D. Craik, “The origins of water wave theory”, *Annual Review of Fluid Mechanics*, vol. 36, pp. 1–28, 2004.

[45] C. C. Mei, M. A. Stiassnie, and D. K.-P. Yue, *Theory and Applications of Ocean Surface Waves: Part 1: Linear Aspects.* World Scientific, 2005.

[46] M. J. Lighthill and J. Lighthill, *Waves in fluids.* Cambridge university press, 2001.

[47] E. Guyon, J. P. Hulin, L. Petit, and C. D. Mitescu, *Physical hydrodynamics.* Oxford university press, 2015.

[48] A. Maurel, J. J. Marigo, P. Cobelli, P. Petitjeans, and V. Pagneux, “Revisiting the anisotropy of metamaterials for water waves”, *Physical Review B*, vol. 96, no. 13, pp. 1–8, 2017.

[49] R. R. Rosales and G. C. Papanicolaou, “Gravity waves in a channel with a rough bottom”, *Studies in Applied Mathematics*, vol. 68, no. 2, pp. 89–102, 1983.

[50] C. Marangos and R. Porter, “Shallow water theory for structured bathymetry”, *Proceedings of the Royal Society A*, vol. 477, no. 2254, p. 20210421, 2021.

[51] F. Moisy, M. Rabaud, and K. Salsac, “A synthetic Schlieren method for the measurement of the topography of a liquid interface”, *Experiments in Fluids*, vol. 46, no. 6, pp. 1021–1036, 2009.

[52] S. Wildeman, “Real-time quantitative Schlieren imaging by fast Fourier demodulation of a checkered backdrop”, *Experiments in Fluids*, vol. 59, no. 6, pp. 1–13, 2018.

[53] W. B. Wright, R. Budakian, and S. J. Putterman, “Diffusing light photography of fully developed isotropic ripple turbulence”, *Physical Review Letters*, vol. 76, no. 24, p. 4528, 1996.

[54] Y. Qian, Y. Zheng, M. Gong, and Y.-H. Yang, “Simultaneous 3D reconstruction for water surface and underwater scene”, in *Proceedings of the European Conference on Computer Vision (ECCV)*, pp. 754–770, 2018.

[55] M. Takeda, H. Ina, and S. Kobayashi, "Fourier-transform method of fringe-pattern analysis for computer-based topography and interferometry", *Journal of the Optical Society of America*, vol. 72, no. 1, pp. 156–160, 1982.

[56] M. Takeda and K. Mutoh, "Fourier transform profilometry for the automatic measurement of 3-D object shapes", *Applied Optics*, vol. 22, no. 24, pp. 3977–3982, 1983.

[57] Q.-C. Zhang and X.-Y. Su, "An optical measurement of vortex shape at a free surface", *Optics & Laser Technology*, vol. 34, no. 2, pp. 107–113, 2002.

[58] P. J. Cobelli, A. Maurel, V. Pagneux, and P. Petitjeans, "Global measurement of water waves by Fourier transform profilometry", *Experiments in Fluids*, vol. 46, no. 6, p. 1037, 2009.

[59] A. Maurel, P. J. Cobelli, V. Pagneux, and P. Petitjeans, "Experimental and theoretical inspection of the phase-to-height relation in Fourier transform profilometry", *Applied Optics*, vol. 48, no. 2, pp. 380–92, 2009.

[60] B. A. Rajoub, M. J. Lalor, D. R. Burton, and S. A. Karout, "A new model for measuring object shape using non-collimated fringe-pattern projections", *Journal of Optics A: Pure and Applied Optics*, vol. 9, no. 6, 2007.

[61] A. Przadka, B. Cabane, V. Pagneux, A. Maurel, and P. Petitjeans, "Fourier transform profilometry for water waves: How to achieve clean water attenuation with diffusive reflection at the water surface?", *Experiments in Fluids*, vol. 52, no. 2, pp. 519–527, 2012.

[62] Keyence, *Confocal Displacement Sensor CL-3000 Series*, 2019.

[63] T. Kulczycki and N. Kuznetsov, "On the 'high spots' of fundamental sloshing modes in a trough", *Proceedings of the Royal Society A: Mathematical, Physical and Engineering Sciences*, vol. 467, no. 2129, pp. 1491–1502, 2011.

[64] T. Kulczycki, M. Kwaśnicki, and B. Siudeja, "The shape of the fundamental sloshing mode in axisymmetric containers", *Journal of Engineering Mathematics*, vol. 99, no. 1, pp. 157–183, 2016.

[65] U. Leonhardt and T. G. Philbin, "Transformation optics and the geometry of light", in *Progress in Optics*, vol. 53, pp. 69–152, Elsevier, 2009.

[66] A. Maurel, K. Pham, and J.-J. Marigo, "Scattering of gravity waves by a periodically structured ridge of finite extent", *Journal of Fluid Mechanics*, vol. 871, pp. 350–376, 2019.

[67] J. Lagarias, J. Reeds, M. Wright, and P. Wright, "Convergence properties of the Nelder–Mead simplex method in low dimensions", *SIAM Journal on Optimization*, vol. 9, pp. 112–147, 12 1998.

[68] E. Monsalve Gutierrez, *Experimental study of water waves: nonlinear effects and absorption.* PhD thesis, Université Pierre et Marie Curie - Paris VI, 2017.

[69] K. Pham, A. Maurel, and J.-J. Marigo, “Two scale homogenization of a row of locally resonant inclusions-the case of anti-plane shear waves”, *Journal of the Mechanics and Physics of Solids*, vol. 106, pp. 80–94, 2017.

[70] M. E. Cage, K. Klitzing, A. Chang, F. Duncan, M. Haldane, R. B. Laughlin, A. Pruisken, and D. Thouless, *The quantum Hall effect.* Springer Science & Business Media, 2012.

[71] D. J. Thouless, M. Kohmoto, M. P. Nightingale, and M. den Nijs, “Quantized Hall conductance in a two-dimensional periodic potential”, *Physical Review Letters*, vol. 49, pp. 405–408, Aug 1982.

[72] G. Ma, M. Xiao, and C. T. Chan, “Topological phases in acoustic and mechanical systems”, *Nature Reviews Physics*, vol. 1, no. 4, pp. 281–294, 2019.

[73] D. Zhao, M. Xiao, C. W. Ling, C. T. Chan, and K. H. Fung, “Topological interface modes in local resonant acoustic systems”, *Physical Review B*, vol. 98, no. 1, p. 014110, 2018.

[74] H. Xue, Y. Yang, G. Liu, F. Gao, Y. Chong, and B. Zhang, “Realization of an acoustic third-order topological insulator”, *Physical Review Letters*, vol. 122, no. 24, p. 244301, 2019.

[75] X. Zhang, M. Xiao, Y. Cheng, M.-H. Lu, and J. Christensen, “Topological sound”, *Communications Physics*, vol. 1, no. 1, pp. 1–13, 2018.

[76] L. Lu, J. D. Joannopoulos, and M. Soljačić, “Topological photonics”, *Nature Photonics*, vol. 8, no. 11, pp. 821–829, 2014.

[77] T. Ozawa, H. M. Price, A. Amo, N. Goldman, M. Hafezi, L. Lu, M. C. Rechtsman, D. Schuster, J. Simon, O. Zilberberg, *et al.*, “Topological photonics”, *Reviews of Modern Physics*, vol. 91, no. 1, p. 015006, 2019.

[78] A. B. Khanikaev and G. Shvets, “Two-dimensional topological photonics”, *Nature Photonics*, vol. 11, no. 12, pp. 763–773, 2017.

[79] A. B. Khanikaev, S. H. Mousavi, W.-K. Tse, M. Kargarian, A. H. MacDonald, and G. Shvets, “Photonic topological insulators”, *Nature Materials*, vol. 12, no. 3, pp. 233–239, 2013.

[80] R. Süsstrunk and S. D. Huber, “Observation of phononic helical edge states in a mechanical topological insulator”, *Science*, vol. 349, no. 6243, pp. 47–50, 2015.

[81] C. Brendel, V. Peano, O. Painter, and F. Marquardt, “Snowflake phononic topological insulator at the nanoscale”, *Physical Review B*, vol. 97, no. 2, p. 020102, 2018.

[82] M. Serra-Garcia, V. Peri, R. Süsstrunk, O. R. Bilal, T. Larsen, L. G. Villanueva, and S. D. Huber, “Observation of a phononic quadrupole topological insulator”, *Nature*, vol. 555, no. 7696, pp. 342–345, 2018.

[83] S. D. Huber, “Topological mechanics”, *Nature Physics*, vol. 12, no. 7, pp. 621–623, 2016.

[84] L. M. Nash, D. Kleckner, A. Read, V. Vitelli, A. M. Turner, and W. T. Irvine, “Topological mechanics of gyroscopic metamaterials”, *Proceedings of the National Academy of Sciences*, vol. 112, no. 47, pp. 14495–14500, 2015.

[85] B. G.-g. Chen, B. Liu, A. A. Evans, J. Paulose, I. Cohen, V. Vitelli, and C. Santangelo, “Topological mechanics of origami and kirigami”, *Physical Review Letters*, vol. 116, no. 13, p. 135501, 2016.

[86] S. F. Edwards, “Statistical mechanics with topological constraints: I”, *Proceedings of the Physical Society (1958-1967)*, vol. 91, no. 3, p. 513, 1967.

[87] W. Su, J. Schrieffer, and A. J. Heeger, “Solitons in polyacetylene”, *Physical Review Letters*, vol. 42, no. 25, p. 1698, 1979.

[88] M. Yan, X. Huang, L. Luo, J. Lu, W. Deng, and Z. Liu, “Acoustic square-root topological states”, *Physical Review B*, vol. 102, no. 18, p. 180102, 2020.

[89] X. Li, Y. Meng, X. Wu, S. Yan, Y. Huang, S. Wang, and W. Wen, “Su-Schrieffer-Heeger model inspired acoustic interface states and edge states”, *Applied Physics Letters*, vol. 113, no. 20, p. 203501, 2018.

[90] M. Esmann, F. Lamberti, A. Lemaître, and N. Lanzillotti-Kimura, “Topological acoustics in coupled nanocavity arrays”, *Physical Review B*, vol. 98, no. 16, p. 161109, 2018.

[91] Z. Yang, F. Gao, and B. Zhang, “Topological water wave states in a one-dimensional structure”, *Scientific Reports*, vol. 6, no. 1, pp. 1–6, 2016.

[92] P. Obrępalski, “Experimental study of surface water waves in periodic channels”, Master’s thesis, Warsaw University of Technology, 2019.

[93] R. Khosropour, S. Cole, and T. Strayer, “Resonant free surface waves in a rectangular basin”, *Wave Motion*, vol. 22, no. 2, pp. 187–199, 1995.

[94] W. Chester, “Resonant oscillations of water waves I. Theory”, *Proceedings of the Royal Society of London. Series A. Mathematical and Physical Sciences*, vol. 306, no. 1484, pp. 5–22, 1968.

[95] W. Chester and J. Bones, “Resonant oscillations of water waves. II. Experiment”, *Proceedings of the Royal Society of London. Series A. Mathematical and Physical Sciences*, vol. 306, no. 1484, pp. 23–39, 1968.

[96] J. Miles, “Resonantly forced, nonlinear gravity waves in a shallow rectangular tank”, *Wave Motion*, vol. 7, no. 3, pp. 291–297, 1985.

Experimental study and modeling of metamaterials for water surface waves

This thesis concerns the study of metamaterials for water surface waves. The study is based on a laboratory experiment which makes it possible to measure the wave field precisely. In the first part, we demonstrate experimentally and numerically that metamaterials can be used to control the wave propagation and resonance properties of a closed cavity, including the cloaking of its eigenmodes. The anisotropic medium is designed using coordinate transformation theory and the homogenization of a three-dimensional linear water wave problem. This medium consists of a set of vertical plates whose spacing is much lower than the wavelength. This structure imposes an anisotropic bathymetry which influences the propagation of the waves differently according to their direction of propagation. Three different cavities manufactured by a 3D printer are tested and compared to the reference case with bathymetry without structuring. Fourier Transform Profilometry, as well as confocal displacement sensors, are used for measurements of water surface deformation resolved in time and space. Experimental data shows a remarkable ability of the metamaterial to influence the anisotropic propagation of waves on the water surface. The second part concerns the metamaterials submerged between two water layers for which a homogenized model is proposed, and the numerical solution by the modal method is provided. The anisotropic properties of such a structure are investigated experimentally using the same technique. An analysis based on the Bloch-Floquet formalism is performed to verify the dispersion relation of this medium predicted by the homogenization method. The main objective of the third part of this thesis is to experimentally study topologically protected edge states in a waveguide with periodic geometry in both linear and nonlinear regimes. One of the representations of topological states, provided by the Su-Schrieffer-Heeger (SSH) model, is applied to describe the observed phenomena. A waveguide with periodic width is compared to the regular case of a rectangular reservoir with constant width. Confocal displacement sensors are used to measure the wave field very precisely. The experimental data is compared with the results of the 2D numerical simulations and the prediction of the SSH model. The results obtained show that this very simple configuration presents all the properties of the SSH model with excellent agreement.

Adam Anglart

PSL UNIVERSITÉ PARIS

SCIENCES SORBONNE UNIVERSITÉ

Institut Langevin ONDES ET IMAGES

IPGP INSTITUT DE PHYSIQUE DU GLOBE DE PARIS

RÉSUMÉ

La thèse concerne l'étude des métamatériaux dans le contexte des ondes à la surface de l'eau. Cette étude s'appuie sur une expérience en laboratoire qui permet de mesurer précisément le champ des ondes. Dans la première partie, nous démontrons expérimentalement et numériquement que les métamatériaux peuvent être utilisés pour contrôler la propagation des ondes et les propriétés de résonance d'une cavité fermée, y compris le « cloaking » de ses modes propres. Le milieu anisotrope est conçu à partir de la théorie de la transformation des coordonnées et de l'homogénéisation d'un problème d'onde tridimensionnel. Ce milieu est constitué par un ensemble de plaques verticales dont l'espacement est très inférieur à la longueur d'onde. Cette structure impose une bathymétrie anisotrope qui influe sur la propagation des ondes différemment selon leur direction de propagation par rapport à ce milieu structuré. Trois cavités différentes, fabriquées par une imprimante 3D, sont testées et comparées au cas de référence avec bathymétrie sans structuration. La profilométrie par transformée de Fourier, ainsi que des capteurs de déplacement confocaux, sont utilisés pour les mesures de la déformation de la surface de l'eau résolues en temps et en espace. Les données expérimentales montrent une capacité remarquable du métamatériau à influer sur la propagation anisotrope des ondes à la surface de l'eau. La deuxième partie concerne les métamatériaux immergés entre deux eaux pour lesquels un modèle homogénéisé est proposé et la solution numérique par méthode modale est fournie. Les propriétés anisotropes d'une telle structure sont étudiées expérimentalement en utilisant la même technique. Une analyse basée sur le formalisme de Bloch-Floquet est effectuée pour vérifier la relation de dispersion de ce milieu prédite par la méthode d'homogénéisation. L'objectif principal de la troisième partie de cette thèse est d'étudier expérimentalement les états de bord topologiquement protégés dans un guide d'ondes à géométrie périodique en régime linéaire et non-linéaire. Une des représentations des états topologiques, fournie par le modèle Su-Schrieffer-Heeger (SSH), est appliquée pour décrire les phénomènes observés. Un guide d'ondes avec une largeur périodique est comparé au cas régulier d'un réservoir rectangulaire avec une largeur constante. Des capteurs de déplacement confocaux sont utilisés pour mesurer le champ d'onde très précisément. Les données expérimentales sont comparées aux résultats des simulations numériques 2D et à la prédiction du modèle SSH. Les résultats obtenus montrent que cette configuration très simple présente toutes les propriétés du modèle SSH avec un excellent accord.

MOTS CLÉS

métamatériaux, mécanique des fluides, ondes, homogénéisation, modèle SSH, étude expérimentale

ABSTRACT

This thesis concerns the study of metamaterials for water surface waves. The study is based on a laboratory experiment which makes it possible to measure the wave field precisely. In the first part, we demonstrate experimentally and numerically that metamaterials can be used to control the wave propagation and resonance properties of a closed cavity, including the cloaking of its eigenmodes. The anisotropic medium is designed using coordinate transformation theory and the homogenization of a three-dimensional linear water wave problem. This medium consists of a set of vertical plates whose spacing is much lower than the wavelength. This structure imposes an anisotropic bathymetry which influences the propagation of the waves differently according to their direction of propagation. Three different cavities manufactured by a 3D printer are tested and compared to the reference case with bathymetry without structuring. Fourier transform profilometry, as well as confocal displacement sensors, are used for measurements of water surface deformation resolved in time and space. Experimental data shows a remarkable ability of the metamaterial to influence the anisotropic propagation of waves on the water surface. The second part concerns the metamaterials submerged between two water layers for which a homogenized model is proposed, and the numerical solution by the modal method is provided. The anisotropic properties of such a structure are investigated experimentally using the same technique. An analysis based on the Bloch-Floquet formalism is performed to verify the dispersion relation of this medium predicted by the homogenization method. The main objective of the third part of this thesis is to experimentally study topologically protected edge states in a waveguide with periodic geometry in both linear and nonlinear regimes. One of the representations of topological states, provided by the Su-Schrieffer-Heeger (SSH) model, is applied to describe the observed phenomena. A waveguide with periodic width is compared to the regular case of a rectangular reservoir with constant width. Confocal displacement sensors are used to measure the wave field very precisely. The experimental data is compared with the results of the 2D numerical simulations and the prediction of the SSH model. The results obtained show that this very simple configuration presents all the properties of the SSH model with excellent agreement.

KEYWORDS

metamaterials, fluid mechanics, waves, homogenization, SSH model, experimental study